Silent and Efficient Supersonic Bi-Directional Flying Wing

Gecheng Zha*
Dept. of Mechanical and Aerospace Engineering
University of Miami
Coral Gables, FL 33124

Louis Cattafesta †and Farrukh S. Alvi‡
Florida Center for Advanced Aero-Propulsion (FCAAP)
Dept. of Mechanical Engineering
Florida State University
2525 Pottsdamer Street, Building A, Suite A229
Tallahassee, FL 32310-6046

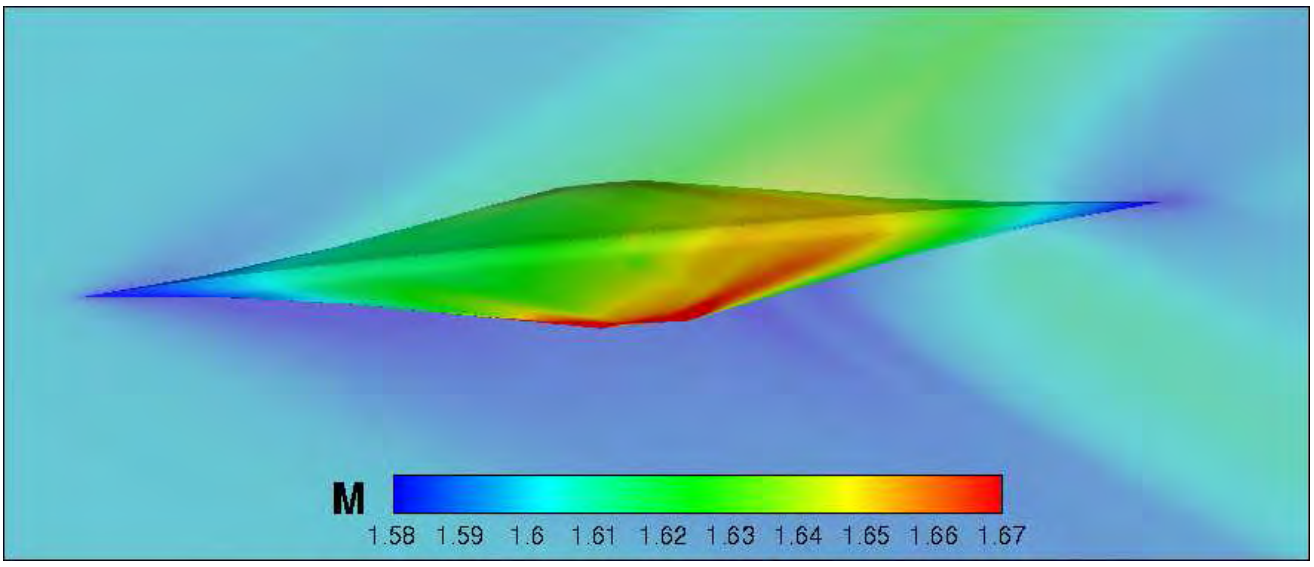

July 9, 2013

* PI, Professor, Director of Aerodynamics and CFD Lab
† CO-I, Professor, Associate Director of FCAAP
‡ CO-I, Professor, Director of FCAAP

Contents

1 Acknowledgment

This project is a team work. We greatly appreciate the following team members for their outstanding and hard working. Graduate Students: Alexis Lefebvre, Jia-Ye Gan, Daniel A. Espinal Undergraduate Seniors: Tom Knight, Christopher C. Longfield, Richard Chan, Olivia M. Chin Faculty: Rajan Kumar, Assistant Professor, Florida State University

We are very grateful to NIAC's funding support from grant NNX12AR05G8 to study this new concept. We are particularly thankful to the program executive Dr. John (Jay) Falker and program manager Jason Derleth for their excellent leadership and strong support, which is always so encouraging with full understanding. All the CFD simulation and design work is done at the Center for Computational Sciences at University of Miami. Without their computing support, this research will not be possible.

2 Summary

The supersonic bi-directional (SBiDir) flying wing (FW) concept has a great potential to achieve low sonic boom with high supersonic aerodynamic performance due to removal of performance conflict between high speed and low speed by rotating 90° in flight. This NIAC Phase 1 research has achieved three objectives: 2) prove the concept based on simulation that it can achieve very low boom with smooth *Sine* wave ground over-pressure signature and excellent aerodynamic efficiency; 3) conduct trade study to correlate the geometric parameters with sonic boom and aerodynamic performance for further automated design optimization in Phase II.

The design methodology developed in Phase I includes three parts: 1) an advanced geometry model, which can vary airfoil meanline angle distribution to control the expansion and shock waves on the airplane surface to mitigate sonic boom and improve aerodynamic efficiency. 2) a validated CFD procedure to resolve near field flow with accurate shock strength. The sonic boom propagation from near field to far field ground is simulated by NASA *NF Boom* code. The surface friction drag prediction is based on flat plate correlation adopted by Seebass [1] and supported by the experimental study of Winter and Smith [2], which is on the conservative side and is more reliable than CFD RANS simulation. 3) a mission analysis tool based on Corke's model[3] that provides design requirements and constraints of supersonic airplanes for range, payload, volume, size, weight, etc. The design mission target is a supersonic transport with cruise Mach number 1.6, 100 passengers, and 4000nm range.

The trade study has several very important findings: 1) The far field ground sonic boom signature is directly related to the smoothness of the flow on the airplane surface. The meanline angle distribution is a very effective control methodology to mitigate surface shock and expansion wave strength, and mitigating compression wave coalescing by achieving smooth loading distribution chord-wise. Compared with a linear meanline angle distribution, a design using nonlinear and non-monotonic meanline angle distribution is able to reduce the sonic boom ground loudness by over 20dBPL. The design achieves sonic boom ground loudness less than 70dBPL and aerodynamic dynamic efficiency L/D of 8.4. 2) Decreasing sweep angle within the Mach cone will increase L/D as well as sonic boom. A design with variable sweep from 84° at the very leading edge to 68° at the tip achieves an extraordinarily high L/D of 10.4 at Mach number 1.6 due to the low wave drag. If no sonic boom constraint is attached, SBiDir-FW concept still has a lot of room to increase the L/D. 3) The round leading edge and trailing edge under high sweep angle are beneficial to improve aerodynamic performance, sonic boom, and to increase volume of the airplane. 4) Subsonic performance is benefited greatly from the high slenderness of supersonic configuration after rotating 90°. A design with excellent supersonic aspect ratio of 0.44, L/D of 8.9, gives an extraordinary subsonic aspect ration of 10 and L/D of 19.7. Two configurations are designed in details to install internal seats, landing gears, and engine installation to demonstrate the feasibility of SBiDir-FW configuration to accommodate all the required volume for realistic airplane.

In summary, it is proved numerically that SBiDir-FW can achieve very low sonic boom and excellent aerodynamic performance for both supersonic and subsonic. It is discovered that the airfoil meanline angle distributions are critical to mitigate far field sonic boom by achieving smooth surface loading distribution with weak shock, expansion waves and compression wave coalescing, whereas the sweep angle determining the aspect ratio has strong effect on aerodynamic efficiency of L/D. It is expected that more improved designs will be achieved in Phase II with automated systematic design optimization.

Here we emphasize that the qualitative findings in Phase I are very encouraging, more important than the quantitative results. Qualitative findings give the understanding of physics and provide the path to achieve the ultimate high performance design. The promising quantitative results achieved in Phase I need to be confirmed by wind tunnel testing in Phase II and ultimately proved by flight test. The other important step forward will be made to study the rotation transition from both CFD unsteady simulation and wind tunnel testing.

3 Introduction

Supersonic commercial flight has always been a great interest of aircraft design engineers, scientists, and business professionals due to the potential to reduce inter-continental travel time. The Concorde (Fig. 1), the first supersonic civil transport to carry passengers, ceased service in 2003 due to high operating costs. However, the efforts to make supersonic commercial flight economically and environmentally viable has never stopped. NASA's strategic plan indicates that the high performance supersonic airplane development is one of the tasks to advance aeronautics research for societal benefit. The NASA Aeronautics Research Mission Directorate (ARMD) has identified a set of key technology challenges for the success of future supersonic flight. The first two challenges are efficiency and environment. The primary efficiency challenges include high supersonic cruise efficiency and light weight. The primary environmental challenges include reduction of sonic boom, airport noise, and high altitude emission pollution.

Supersonic transports (SSTs) have two major problems: sonic boom and aerodynamic efficiency. Sonic boom is the noise that propagates to ground as an N-wave created by the shock waves of a supersonic airplane. Fig. 2 to 4 show the measured shock wave system of SR 71 and the N-wave over-pressure propagating to different altitude[4]. The N-wave represents the sharp pressure rise from the front shock wave, followed by a series of expansion waves, and ends with a shock wave to balance the pressure to ambient value. The amplitude of N-wave determines the strength of the sonic boom and the annoyance to people. The measured ground N-wave over-pressure amplitude of SR71 propagating from 80,000 ft at Mach 3 is 0.9 psf. Concord as shown in Fig. 1 has the ground N-wave amplitude of 1.94psf propagating from 52,000 ft altitude at Mach 2. Due to the sonic boom, FAA has banned supersonic flight over land. It is not economic viable for airlines if they can only fly supersonically over sea. The prohibition of the Concorde's flight over populous land areas limited its commercial success. Resolving sonic boom issue is hence essential for civil supersonic flight, whereas the aerodynamic efficiency, even though very important, becomes secondary.

One factor affecting aerodynamic efficiency is the extra drag contribution during supersonic flight: the wave drag caused by the entropy increase of strong shock waves. Wave drag does not exist for subsonic airplanes and is not a serious problem for transonic flight due to the low supersonic Mach number. The second factor that affects efficiency is the large flight speed disparity between take-off/landing and cruise. At take-off and landing, the low flight speed requires a high aspect ratio (AR) and low wing sweep angle. High-speed cruise however requires the opposite characteristics. A compromise between low speed take-off/landing and high-speed cruise efficiency is required.

The flying wing and blended wing body concepts eliminate the non-lifting fuselage component of the conventional tube and wing configuration, so efficiency during subsonic flight is improved. However, the flight of a supersonic flying wing or blended wing body configuration for civil

Figure 1: Concord, supersonic transport, Mach 2.0

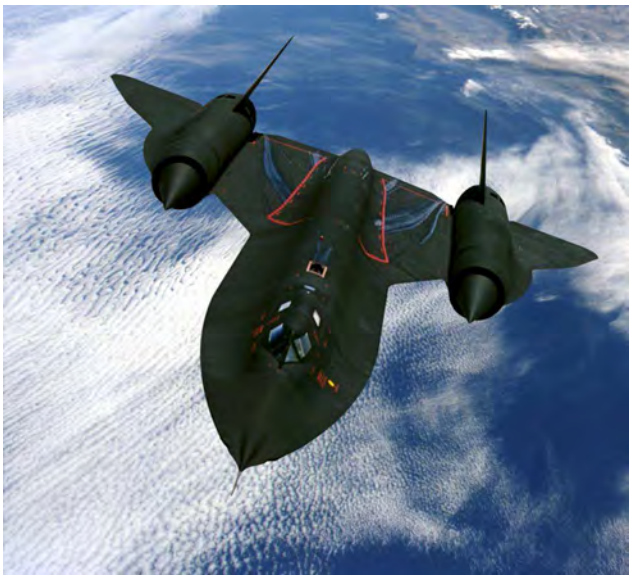

Figure 2: SR71, M=3.0

Figure 3: Shock waves of SR71

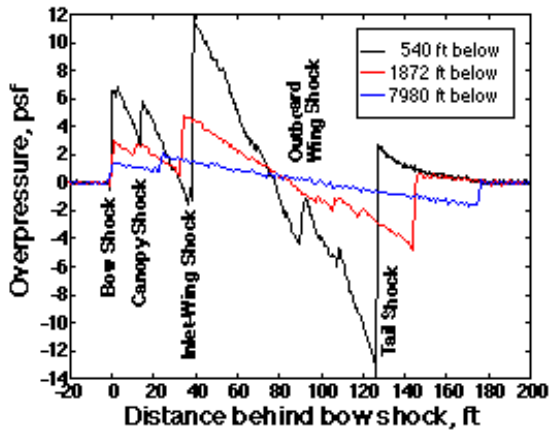

Figure 4: SR71 over-pressure propagation

transport has not appeared, and the full conceptual study of such configurations is rarely seen.

The oblique flying wing (OFW) concept as shown in Fig. 5 proposed by Jones was intended for the development of supersonic flying wings[5, 6]. An excellent review of oblique wing history is given by Hirschberg et al.[7, 8] and a helpful introduction to oblique flying wings and their conceptual design is provided by Desktop Aeronautics. The advantage of oblique flying wings is that the sweep angle can be varied during a flight mission for different Mach numbers to obtain a high aspect ratio at low speeds and a low aspect ratio at high speeds[6, 8, 7]. Such performance is appealing for supersonic airplane design.

However, there are some difficulties with oblique flying wing or oblique all wing (OAW) concepts. For example, the configuration of an OFW is asymmetric about flight direction. The asymmetry of the configuration may create serious problems for stability and control, in particular at a high sweep angle[9, 10, 11, 12, 13]. Second, to accommodate sufficient headroom for passengers, the airfoil thickness must be high and the OFW airplane size will be usually very

Figure 5: Oblique wing tested by NASA

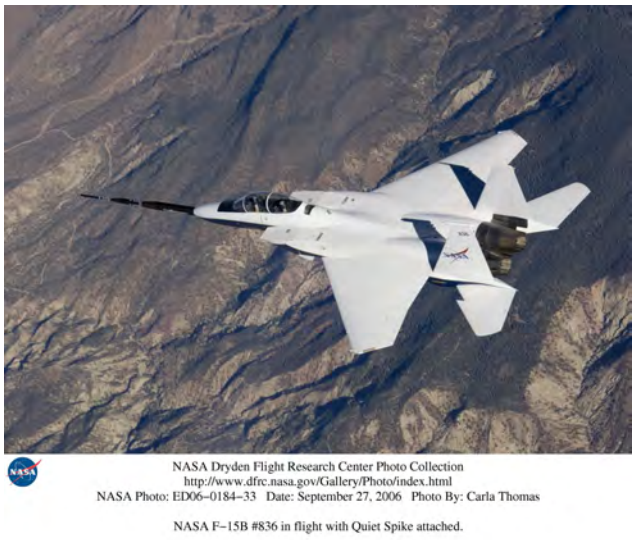

Figure 6: Quiet Spike^{TM} concept of Gulfstream Aerospace

large. This is because an OFW stacks the airfoil to align with the low speed flight direction in order to form a high aspect ratio elliptic planform. Hence, the airfoil chord is short. This is different from the regular flying wing concept that has the airfoil aligned with the cruise flight direction so that a long chord length can be used. The high thickness airfoil of an OFW would not be favorable for supersonic flight since it creates large wave drag. The large airplane size would also create airport operating difficulties[14]. Nonetheless, even though the oblique wing configuration has potential to achieve high aerodynamic efficiency, it does not have an inherent advantage in reducing sonic boom.

3.1 Overview on Sonic Boom Mitigation

The shock waves contributing to sonic boom are formed by two mechanisms, volume blockage and lift. A solid blockage in a supersonic flow will generate a front shock, followed by an expansion wave due to the diminishing blockage with reduced pressure, which needs to return to ambient pressure through a shock at the end. The pressure variation forms a N-wave that propagates to the ground and produces the sonic boom. However, the strength of the shock waves is determined by the area-weighted distribution of the blockage. The more slender the volume blockage is distributed, the weaker the shock. A very slender body will therefore generate shock waves as weak as isentropic compression wave.

In addition to volume blockage, an airplane must generate lift, which requires high pressure on the lower surface (pressure surface) and low pressure on the upper surface (suction surface). The high pressure will generate compression wave and the low pressure will generate expansion wave. They both propagate downstream within their Mach cone. The compression wave will have slightly higher temperature than the expansion and hence faster wave speed, which is the speed of sound. Away from the airplane in the near field, the pressure wave thus will be measured as the high pressure compression wave in the front and the expansion wave reducing the pressure will follow. Usually, due to the higher curvature on suction surface, the pressure reduction extent by the expansion wave is more than the pressure rise extent of the front compression wave. The

pressure downstream of the front compression wave hence will be lower than the ambient pressure. To return the pressure back to ambient pressure, compression waves at the end of the aircraft are needed. Since a compression wave in the downstream always has a higher wave speed and Mach cone angle than the one in the upstream, they have the tendency to merge in the mid-field or far-field to form a shock wave. If both the front and tail compression waves become shock waves, they appear on the ground as an N-wave. The longer and smoother the lift is distributed, the less intense the compression waves will coalesce. It is possible that the compression waves will not have enough time to coalesce when they reach ground if the pressure compression is smooth and gradual. In that case, we will obtain smooth *Sine* wave shape pressure wave on ground instead of N-wave.

To weaken the shock effect and minimize sonic boom, the dominantly used method at present is to follow the mid-field over pressure signatures suggested by Seebass and George[15, 16, 17] and later further advanced by Darden[18], a flat rooftop shape or a ramp shape. The former is to achieve low ground over-pressure signature and the latter is to achieve weak shock. The flat rooftop shape mid-field over-pressure signature may be achieved by implementing nose bluntness following the area rule theory[19, 5, 17, 16, 20], which is based on linear model for axisymmetric body of revolution and is applied to airplane lifting surface by using equivalent area. A blunt nose design creates a shock distribution in which the greatest shock strengths are near the aircraft and the shocks are weakened gradually due to interaction with expansion waves as the shock waves travel from the aircraft to the ground. Unfortunately, this method also induces substantial wave drag since the entropy increase due to the strong shock waves is irreversible. Darden investigated nose-blunt relaxation as a compromise between the blunt nosed low-boom aircraft and sharp nosed low drag design[21]. McLean found that the pressure signature that reaches the ground from a long slender aircraft with minimal weight change may not fully develop into the far-field N-wave form[22].

The ramp shape mid-field over-pressure signature to mitigate sonic boom is to generate weak leading edge(LE) and trailing edge(TE) shocks, or multiple weak shocks, or ideally isentropic compression waves, to minimize or remove N-wave ground over-pressure signature. For example, designs with sharp nose is for this purpose, which is aerodynamically efficient, but may produce a strong shock at mid-field and far-field distances from the aircraft. In principle, a sharp nose with weak shock or isentropic compression is more likely to achieve both high aerodynamic efficiency and low sonic boom than the nose bluntness method.

The Quiet Supersonic Platform (QSP) Shaped Sonic Boom Demonstrator (SSBD) program [23] sponsored by DARPA was to prove the theory of Seebass, and George[17] by shaping the nose to weaken the front sonic boom of F-5E flight test aircraft [20]. The significance of that project is to demonstrate that ground sonic boom can be modified by shaping the geometry and the resulted near field pressure signature. However, the SSBD is not a low boom design.

The Quiet Spike^{TM} of Gulfstream Aerospace as shown in Fig. 6 is an example of using sharp nose to reduce sonic boom. It was a joint program of Gulfstream Aerospace and NASA Dryden Flight Research Center, in which the concept of an extendable nose spike for sonic boom minimization was investigated[24]. In supersonic flight tests with a spike mounted on F-15B aircraft, the typical N-shaped pressure wave was reduced to a series of weaker shocks. However, the long spike brings structural difficulties to make it stable and results in other system complication and weight penalty. The Quiet Spike^{TM} concept may be feasible for a small business jet with 8-12 passengers. For a large supersonic transport, the feasibility of using such a long spike is uncertain.

In 2008, NASA has outlined the requirements of N+2 (year 2020-2025) and N+3 (year 2030-2035) goal of supersonic civil transport[25]. For N+2, the range $\geq$ 4000nm, Mach number =1.6-2.0, passenger 25-100. For N+3, the range $\geq$ 4000nm, Mach number =1.3-2.0, passenger 100-200. The challenging requirement for both N+2 and N+3 is the sonic boom noise level (based on linear theory) should be between 65 to 70 dBPL. NASA contracted Boeing [26, 27] and Lockheed Martin [28] to conduct design of N+2 supersonic airplane. Both the designs have good aerodynamic performance, but the sonic boom level is at about 80dBPL and are considered as a significant progress on low boom supersonic airplane design. However, the boom noise is still quite far away from the targeted 65 to 70 dBPL. Fig. 7 is Boeing's projected supersonic civil airplane up to N+3 in 2040. Fig. 7 also indicates that Boeing's supersonic airplane configuration for the next 3 decades will have no drastic variation, the difference is in the details and refinement.

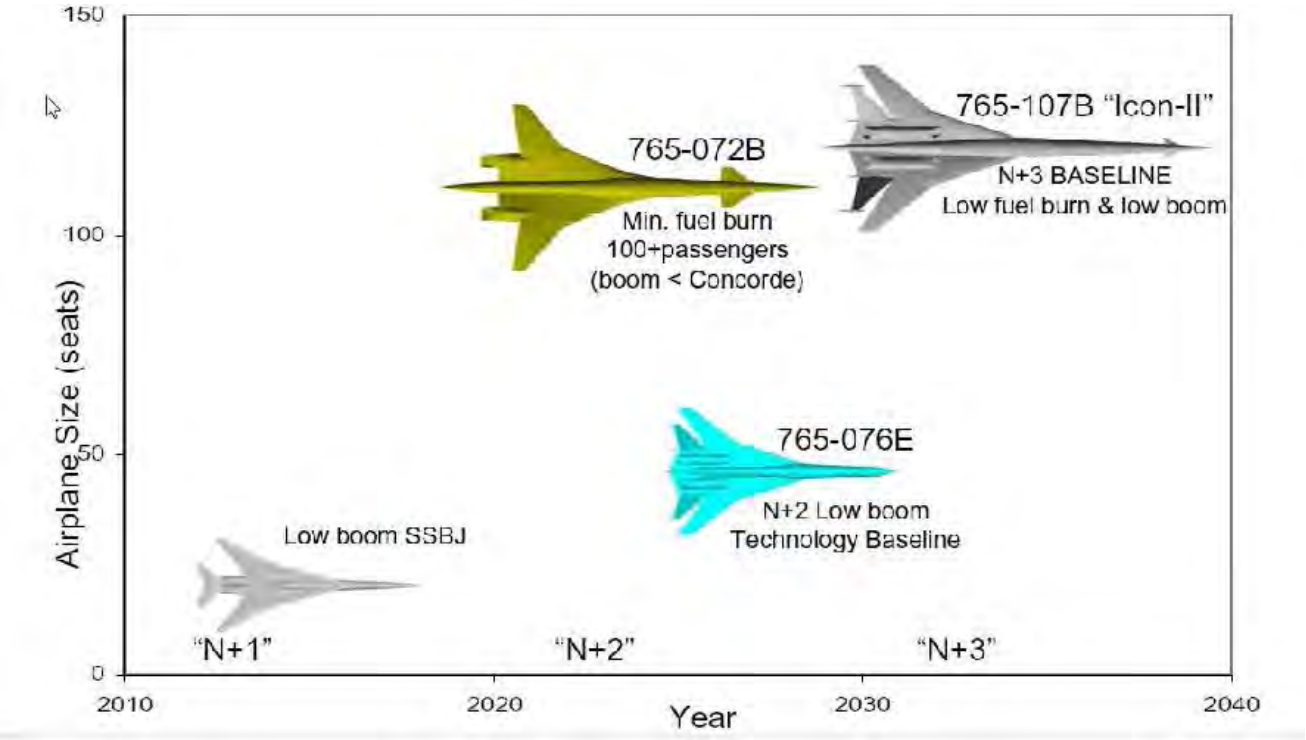

Figure 7: Boeing's projected supersonic airplane of N+1, N+2, and N+3(Courtesy to Welge et al from [26])

Automated design optimization plays a very important role in the supersonic airplane design refinement. For example, both the N+2 designs of Boeing[27] and Lockheed Martin[28] are completed with Design of Experiment, which forms a responsive surface based on previous design samples and extracts the optimum. An important progress on design optimization of supersonic airplane is to use adjoint method for gradient calculation originally suggested by Jameson [29, 30]. The research efforts using adjoint method to mitigate sonic boom were first made by Alonson et al [31, 32]. Rallabhandi et al [33] extends the adjoint equation method of NASA FUN3D CFD code to directly calculate the gradient from ground boom signature instead of the near field signature. Rallabhandi further developed a reversed approach to shape an aircraft to equivalent area using discrete adjoint approach. Design optimization can seek an optimum solution efficiently under the design space defined by a design concept. It is difficult to rely on design optimization to find a breaking through new concept. Too much dependence on design optimization could also have

the risk of losing the understanding of the physics.

In NIAC Phase I research based on the aerodynamics principle described above, we proposed to study a novel Supersonic Bi-Directional Flying Wing concept (SBiDir-FW)[34, 35, 36, 37] aimed at achieving low sonic boom, minimizing wave drag, maximizing the supersonic and subsonic aerodynamic efficiency and performance. The concept is intended to break through the technical barriers of conventional supersonic tube-wing configurations. The key idea is to render the airplane to achieve ultra-high slenderness and length that are drastically greater than those of conventional supersonic configurations. The following is the description of the concept.

4 Supersonic Bi-Directional Flying Wing

4.1 The Concept

The Supersonic Bi-Directional Flying Wing [35, 36, 37] is aimed at breaking through the technical barriers of high sonic boom, poor subsonic performance, and high wave drag of conventional supersonic tube-wing configurations. The key idea is to render the airplane to have ultra-high slenderness at supersonic and high aspect ratio at subsonic. The following is the description of the concept:

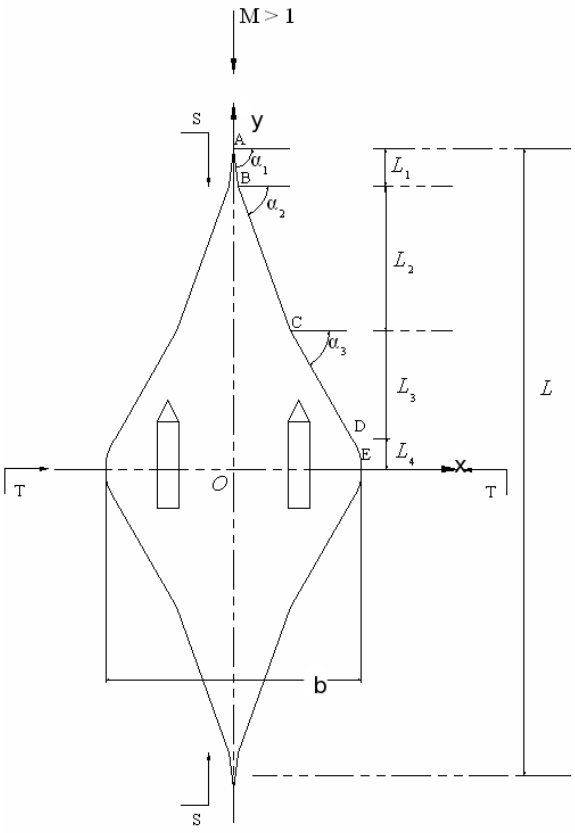

Figure 8: Sketch of a SBiDir-FW Planform flying in supersonic mode (not to scale)

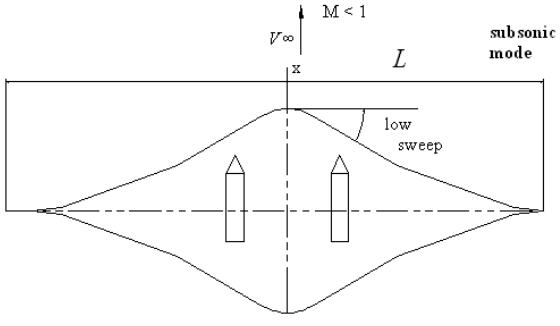

Figure 9: Sketch of a SBiDir-FW Planform flying in subsonic mode (not to scale)

To achieve high aerodynamic efficiency for both supersonic and subsonic, the airplane is a flying

wing or blended wing-body configuration with a symmetric planform about both the longitudinal and span axes with two flight directions altered by 90°. At subsonic flight, the planform will rotate 90° from the supersonic mode shown in Fig. 8 to the subsonic mode as shown in Fig. 9. Fig. 10 shows the 3D supersonic flight direction and the thin airfoil highlighted to form the flying wing to achieve low wave drag. Fig. 11 shows the subsonic mode after 90° rotation from the supersonic mode also with the subsonic airfoil highlighted. A reversed rotation will be done when the mode is changed from subsonic to supersonic. Since the span is significantly shorter than the length, the subsonic airfoil will be significantly thicker than the supersonic airfoil as shown in Fig. 11 to provide high lift coefficient needed for subsonic flight.

The engines will not be rotated and will be always aligned with the flight direction. The rotating turbomachinery inside the jet engines also provide the gyroscope effect to enhance the engine stability. The yaw moment to rotate the airframe will be generated by ailerons or flaps on the two sides of the flying wing. No powered driving system like that for swing wing is needed to rotate the airframe and hence the weight penalty and system complication can be avoided. The desirable transition mode Mach number is high subsonic such as about 0.8 to avoid the unsteady force introduced by shock waves at supersonic.

The subsonic aspect ratio will be substantially increased by $(\frac{L}{b})^2$ based on the following relation:

$$AR_{M<1} = ((\frac{L}{b})^2) * AR_{M>1} \tag{1}$$

where L is the airplane length and b its span.

Moreover, the sweep angle at subsonic will be largely reduced as the following:

$$\delta_{M<1} = 90^o - \delta_{M>1} \tag{2}$$

Fig. 11 shows the subsonic flight mode with high aspect ratio and Fig. **??** shows the supersonic flight with a very low aspect ratio after rotation 90^o. To make the flying wing symmetric about both axes, the airfoil stacked is also symmetric as highlighted in Fig. 10 and 11. The symmetric planform will let the trailing edge become leading during the rotation and generate lift to stabilize the mode transition similar to a flying Frisbee. Even though a thin airfoil is used to stack the flying wing in the supersonic direction, sufficient volume can be easily achieved due to the long length of the flying wing body, which is also the chord of the flying wing airfoil.

The SBiDir-FW has the following inherent aerodynamic advantages over the conventional wing-tube configurations.

4.1.1 Significantly higher slenderness and longer length at Supersonic

Here we define the slenderness coefficient of an object C_s as the following, the greater the value, the higher the slenderness:

$$C_s = V/A_{max}b \tag{3}$$

where V is the total volume, A_{max} is the maximum cross section area normal to the flight direction, and b is the wing span.

Figure 10: A SBiDir-FW civil transport in supersonic mode flying toward right, supersonic thin airfoil highlighted in the middle.

Figure 11: A SBiDir-FW civil transport in subsonic mode flying toward right, subsonic thick airfoil highlighted in the middle.

For a SBiDir-FW configuration, usually the maximum cross section area is at the wing span location at 50% of the airplane length. A_{max} and V may be evaluated as the following:

$$A_{max} = b * t_{avg_b}, \quad V = S * t_{avg_{all}} \tag{4}$$

where t_{avg_b} is the averaged thickness at the wing span location, $t_{avg_{all}}$ is the averaged thickness of the whole airplane.

$$C_s = S/b^2(\frac{t_{avg_{all}}}{t_{avg_b}}) = \frac{t_R}{AR}, \quad t_R = \frac{t_{avg_{all}}}{t_{avg_b}} \tag{5}$$

where t_R is the averaged thickness ratio of the overall airplane to the one at span location. Once the thickness of the configuration is chosen, the slenderness is determined by the planform aspect ratio. The smaller the aspect ratio, the higher the slenderness coefficient.

For the same sweep angle, planform area, and thickness distribution, a diamond wing as sketched in Fig. 10 will have an aspect ratio half of a delta wing, which represents a wing planform of a conventional wing-tube configuration. A diamond wing will have the length $\sqrt{2}$ (1.414) time longer than that of a delta wing and the wing span is $\sqrt{2}/2$ time shorter. Note that this comparison only includes the wing planform. For a SBiDir-FW configuration, the wing planform is the whole airplane. For a conventional wing-tube airplane, the fuselage takes a substantial volume and is also the maximum length. The slenderness coefficient of a SBiDir-FW configuration hence will be more than 2 times greater than that of a conventional wing-body configuration. The lift distribution length of a SBiDir-FW configuration is the whole airplane length from head to tail, the maximum possible length of an airplane. The higher slenderness (smaller aspect ratio) and longer length are all beneficial to reduce shock strength, mitigate coalescing of compression wave in the mid-field, and ultimately minimize the sonic boom and wave drag. Furthermore, the flying wing configuration uses the whole body area as the lifting surface. In other words, it uses the maximum possible length and least possible area, which will satisfy the required volume of the mission with minimum weight. Attributed to the supersonic flow characteristics that disturbance only travels downstream, a small aspect ratio brings little induced drag penalty that occurs at subsonic.

4.1.2 Favorable Aspect Ratio at All Speeds

As indicated by Eq. 1 and 7.3, the smaller the supersonic aspect ratio, the higher the subsonic aspect ratio; the larger the supersonic sweep angle, the smaller the subsonic sweep angle. The conflict of subsonic and supersonic aerodynamic performance of conventional tube-wing configuration is hence removed by rotating the airplane 90°. In other words, designers can favor the supersonic aerodynamic performance as much as needed and do not have to compromise for subsonic performance. High supersonic aerodynamic performance could be naturally translated to high subsonic performance. Conventional supersonic wing-tube configuration usually do not use aspect ratio smaller than 2. Otherwise, they will have difficulty during takeoff and landing at low speed. For SBiDir-FW, a typical supersonic aspect ratio is about 0.5, which translate to subsonic aspect ratio over 10. As an example of conventional design, the Concorde has excellent supersonic aerodynamic efficiency of L/D=7, but its subsonic L/D is only 4. For SBiDir-FW with high aspect ratio and higher maximum lift coefficient at subsonic, the take-off and landing performance at low speed is outstanding.

4.1.3 Efficient Use of Area to Reduce Weight

For the SBiDir-FW without a non-lifting fuselage, all area and volume contributes to lifting surface. For the same payload, the overall size of the airplane hence is smaller and lighter. In fact, the supersonic longitudinal symmetric airfoil section, which is equivalent to the "fuselage" of the conventional wing-tube configuration that generates little lift but drag, plays the most important role to produce lift, reduce shock strength, and the associated sonic boom and wave drag. Hence the design philosophy is very different from the conventional design.

4.1.4 Applicable to Hypersonic Vehicles

The same principle and advantages of SBiDir-FW also apply to hypersonic flight such as one-stage to orbit reusable vehicles to have low wave drag at hypersonic and high lift and controllability at take off/landing at regular airports.

4.2 The Principle

The basic principle of SBiDir-FW concept to achieve low sonic boom and high supersonic aerodynamic efficiency is to make full use of the inherent advantages as below:

1) Minimize the shock strength by maximizing the slenderness with minimal aspect ratio that is sufficient to provide required lift, supersonic L/D, planform area, and required volume.

2) Smoothly distribute the lift loading along the whole body length of an aircraft(the possible longest length) with maximum slenderness to minimize compression wave coalescing in the mid and far filed.

3) The high slenderness features does not hurt any subsonic performance after rotating 90°. Instead, it enhances the subsonic performance by providing high aspect ratio and high airfoil thickness. Hence the concept has high aerodynamic performance to cover the whole fight envelop.

4.3 Impacts

The success of the SBiDir-FW will bring the following profound impacts to benefit society:

1) Make quiet supersonic travel available due to very low sonic boom or no sonic boom.
2) Make airport noise as low as high performance subsonic airplane due to excellent subsonic aspect ratio, L/D, and high subsonic lift coefficient.
3) Make clean supersonic travel available due to high aerodynamic efficiency with less fuel consumption and high altitude emission.
4) Make supersonic flight affordable to ordinary people due to low operating cost.
5) Make airline companies profitable due to the high aerodynamic efficiency and permitted flight everywhere over land.
6) Tremendously reduce the passenger discomfort due to the long flight time for continental travel. For example, the current 14 hours flight from New York to Tokyo can be reduced to 7 hours if fly at Mach 1.6.
7) The same technology and knowledge can be applied to hypersonic vehicle for continental flight or reusable one-stage to orbit for space travel and satellite delivery. The hypersonic vehicle can take off and landing at regular airport with high subsonic performance and cruise at hypersonic speed with minimum wave drag.

5 Research Approaches

The research approach is based on the physics principle of basic aerodynamics to minimize the shock waves strength and obtain smooth near field and ground sonic boom signature.

5.1 Geometry Model

A geometry model is crucial to provide the required controllability to achieve the aerodynamic performance, specifically to minimize shock strength in this research. An ideal geometry model will allow designers to explore the design space with minimal design parameters to achieve the optimum design either manually or using automated design optimization. In this Phase I research, an advanced geometry model for this purpose is developed following the strategy for transonic and supersonic aircraft engine compressor/fan blades[38].

The wing is created by stacking a series of airfoil along leading edge. In our designs, we use 5 to 8 airfoil sections to form a flying wing. A leading edge sweep and dihedral angle distribution can be specified at any leading edge point. Once the sweep and dihedral angle distribution are determined, the flying wing planform is determined, so are the planform area and aspect ratio. Since a SBiDir-FW has a symmetric planform, the airfoil needs to be symmetric about the 50% chord location. Hence the maximum thickness location is at 50% of the chord. After the planform is determined, the next most important step is to generate the meanline angle distribution of each airfoil.

Once the meanline angle is determined, the actual meanline curves are generated by using a spline technique. Then the airfoil is formed by adding the thickness circles along the airfoil meanlines. Again, due to the symmetric requirement, the meanline angle distribution is symmet-

ric about 50% chord location. Our geometry model allows designers freely adjust the meanline angel distribution of each airfoil. The meanline angle is to control the incidence angle of the flow approaching the airfoil, the total flow turning that controls the aifoil loading, and local flow turning that control the local expansion and shock waves.

The definition of flow incidence is similar to angle of attack of an airfoil, but not the same. The flow is defined as the angle between the flow velocity vector and the meanline angle at leading edge. If the flow velocity has the same direction as the airfoil meanline angle, the incidence is zero. If the flow angle is greater than the LE meanline angle, the incidence is positive, otherwise, the incidence is negative. For a supersonic thin airfoil, a zero incidence will generate a weak LE shock since the flow is aligned with the LE. A positive incidence is expected to generated a stronger LE shock going downward and a local expansion on the suction surface LE region. A negative incidence would be opposite to generate a stronger shock going upward and a local expansion on the pressure surface LE region.

The airfoil thickness distribution from the leading edge to the maximum thickness is determined following a quarter-sine wave distribution. For leading and trailing edge, the designers also need to specify the thickness. An ellipse at leading edge(LE) and trailing edge (TE) will then be formed based on the thickness and the ratio of the major and minor axes ratio. A graphical user interface (GUI) is developed using Java language to allow designers directly adjust the meanline angle distributions point by point using mouse click. The meanline angle distribution adjustment is based on the airfoil surface isentropic Mach number distributions predicted by CFD, which indicates the flow incidence, shock location, and shock strength. The principle is to give the airfoil a moderate incidence to weaken the front shock and a favorable turning on the airfoil to minimize the shock strength. How to create desirable meanline angle distributions for each airfoil section to minimize the sonic boom and maximize ratio of lift to drag is the critical part of the design, which will be elaborated more in the later section when we explain the designs achieved. The designers can instantly see the airfoil shape change on the screen when they vary the meanline angle distribution of each airfoil using the GUI.

5.2 Numerical Approach

The in house high order accuracy CFD code FASIP, which is intensively validated with various 2D and 3D steady and unsteady flows including sonic boom[39, 40, 41, 42, 43], is used for the CFD analysis. To accurately capture shock waves and sonic boom, high order shock capturing schemes, including 3rd order MUSCL scheme[44], 3rd, 5th and 7th order WENO schemes and a finite compact scheme combining a shock detector and 6th order Pade scheme, are utilized in the code[41, 42, 43, 45]. A set of 4th order and 6th order central differencing schemes are devised to match the same stencil width of the WENO schemes for the viscous terms[46, 47]. The Roe's scheme [48] and a low diffusion E-CUSP scheme developed by Zha et al[49] are used as the approximate Riemann solver with the MUSCL and WENO shock capturing schemes. For turbulent simulations, FASIP has implemented Detached Eddy Simulation (DES)[50, 51, 52, 53, 54, 55, 56], Large Eddy Simulation(LES)[47, 57], and Reynolds averaged Navier-Stokes (RANS)[58, 46, 59, 60, 61, 62, 63, 64]. An implicit 2nd order time accurate scheme with pseudo time and unfactored Gauss-Seidel line relaxation is employed for time marching. For aeroelasticity problems, a fully coupled fluid-structural interaction model is implemented[65, 56, 64, 52, 58, 60, 61, 51]. The MPI parallel computing is utilized and a high scalability is achieved[66].

The Euler inviscid solver, which is validated with accurate prediction of sonic boom, is used for design iterations at supersonic mode. The Euler solver also predicts lift and pressure drag accurately. The only drag missing from an Euler solver is the supersonic surface friction drag. Winter and Smith [2] conducted rigorous experimental study of supersonic friction drag for delta wings, which has the airfoil maximum thickness of 8.3%, Mach number from 1.5 to 2.6 and angle of attack (AoA0 up to 10°. The delta wing is tappered and twisted. His conclusion is that despite the wide variations in skin friction on the wing surface, the total skin-friction drag is probably only some 5 to 10 per cent less than that on a flat plate due to the adverse pressure gradient. The drag shows little variation with incidence.

Since the SBiDir-FW configurations simulated in this Phase I research do not include the propulsion systems, and the ranges of Mach number, sweep angle, AoA and airfoil thickness are all within the same range of Winter- Smith experiment[2], we hence adopt the flat plate surface friction coefficient modified for different altitude as the surface friction coefficient of SBiDir, which is on the conservative side of the drag estimate. The utilization of flat plate surface friction coefficient for SBiDir-FW design iteration not only saves tremendous CPU time of CFD simulation, it is also more reliable than the friction prediction from Reynolds averaged Navier-Stokes (RANS) solvers[67], which often have difficulty in accurately predicting drag. The same way using flat plate friction coefficient for supersonic wing is also adopted by Seebass[1].

The viscous Navier-Stokes solver is used to predict the lift, drag (with both pressure and friction drag) and moments for the subsonic mode of SBiDir-FW, which has thick airfoil and flow separation. A flat plate friction coefficient would not be as accurate as for supersonic mode with thickness less than 3% and no flow separation.

The far field sonic boom propagation to ground is simulated using the the NASA *NF Boom* code, which has been intensively validated for sonic boom propagation by NASA[68].

5.3 Mission Analysis

To implement realistic constraints for this conceptual design using SBiDir-FW, the mission requirement include cruise Mach number of 1.6, pay load of 100 passenger with standard luggage, and range of 4000nm. The text book *Design of Aircraft* by Corke [3] provides an excellent aircraft conceptual design methodology, which is adopted for the SBiDir design. A FORTRAN code was written based on this methodology in order to facilitate the design iterations.

To maximize the benefit of SBiDir-FW concept, a length of 100m is selected so that we can use thin airfoil with the thickness less than 3%, which will give sufficient headroom space and volume to hold passengers and fuel. It turns out that the volume is in general easy to achieve due to the inherent advantage of flying wing. Once the sweep and dihedral angles distributions are specified, the planform area is determined. When the complete SBIDir-FW geometry is determined and CFD analysis is completed, the coefficients of lift, drag, moment and the ratio of lift to drag are available. With all these geometry and aerodynamic performance parameters including engine fuel consumption, structure factor, and flight altitude as the input to the mission analysis code, an estimate of the aircraft weight at different flight stages is iterated by using standard estimates of the weight of passengers and crew, luggage, cockpit, engines, and other components. The range is one of the output results from the mission analysis.

In this design, the SBiDir configuration is expected to provide a very low wing loading, and thus short take-off and landing distances are expected. To choose the propulsion system, a

computation of the overall aircraft drag is performed to ensure that the plane has sufficient thrust, and then engines that meet the thrust requirements are sized based on a reference engine.

5.3.1 Preliminary Take-off Weight Estimate

The take-off weight consists of fuel weight, payload weight, and empty weight. The fuel weight is mostly dependent on the fuel consumption of the engine selected for the range of the mission. The payload weight refers to the cargo such as passengers and luggage and the empty weight refers to the structural weight of the airplane.

For the cruise out to destination flight phase, the range is determined by the following equation

$$R = \frac{V}{TSFC}\left(\frac{L}{D}\right)\ln\left[\frac{W_i}{W_f}\right] \tag{6}$$

where V is the cruise velocity, L is the lift, D is the drag, $TSFC$ is the thrust-specific fuel consumption, and W_i/W_f is the ratio of initial weight to final weight of the flight phase.

For the take-off flight phase which includes engine start, taxiing, take-off and climb out an estimate of 2.5% to 3% of total take-off weight was consumed in fuel such that

$$0.97 \leq \frac{W_f}{W_i} \leq 0.975 \tag{7}$$

Same empirical estimate was used for landing where W_f is the total aircraft weight after completing the mission and W_i is the aircraft weight after cruise and loiter.

For climbing and accelerating to cruise conditions the weight fraction was estimated by the empirical relation given by Corke in Equation 8

$$\frac{W_f}{W_i} = 0.96 - 0.03 * (M - 1) \tag{8}$$

where M is the cruise Mach number.

For estimates on loiter fuel consumption the endurance relation for turbo-jet engines shown in Equation 9 is used

$$E = \frac{1}{TSFC_{sub}}\left(\frac{L}{D}\right)_{sub}\ln\left[\frac{W_i}{W_f}\right] \tag{9}$$

where E is the endurance (loiter) time and $TSFC_{sub}$ and L/D_{sub} are the values estimated for SBiDir in subsonic configuration.

5.4 Engine Selection

With the drag coefficient decided form the numerical simulation, the required thrusts at cruise altitude and sea level are determined. The other consideration of engine selection includes low-bypass ratio and low dry weight. Since no existing engines match the requirements of SBiDir-FW, a reference engine needs to be selected for scaling the engine size and weight for SBiDir-FW propulsion system. The engine considered by Boeing N+2 supersonic propulsion system with projected futuristic weight and fuel consumption of 0.7 ???[26] is used as the reference engine. The relations used for the sizing factor and other engine parameters are as follows:

$$SF = \left[\frac{T}{T_{ref}}\right] \tag{10}$$

$$\left[\frac{d}{d_{ref}}\right] = SF^{1/2} \tag{11}$$

$$\left[\frac{\dot{m}}{\dot{m}_{ref}}\right] = SF \tag{12}$$

$$\left[\frac{W_{eng}}{W_{eng_{ref}}}\right] = SF^{a}(0.8 \leq a \leq 1.3) \tag{13}$$

$$\left[\frac{L_{eng}}{L_{eng_{ref}}}\right] = SF^{(2a-1)/2}(0.8 \leq a \leq 1.3) \tag{14}$$

The engines will be mounted on the upper surface of the aircraft in order to minimize the engine jet noise at take-off by shielding the noise emitted from propagating to the ground. The shock waves generated by the engines during supersonic cruise will also be blocked by the airframe preventing the shock propagation to ground. There will be a small distance between the engines and the airplane surface to avoid interrupting the flying wing flow.

5.4.1 Wing Loading

Wing loading affects several aspects of flight, namely the stall velocity and the turn rate of the aircraft. Wing loading varies during the mission as the aircraft weight changes. The SBiDir has a low maximum wing loading due to its improved aerodynamic performance and large planform area, characteristics inherent in flying wings. Stall velocity is computed using Equation 15

$$V_s = \left[\frac{W}{S}\frac{2}{\rho C_L}\right]^{0.5} \tag{15}$$

From flight dynamics it is known that the lower the wing loading the lower the stall velocity. Because of this, having a lower stall velocity will require significantly shorter runway length for takeoff and landing. This aircraft exhibits a stall velocity at takeoff of ??? $112.8 ft/s$.

The load factor, which will influence the maximum sustained and instantaneous turn rate of the aircraft, is also affected by the wing loading and they are related by Equation 16

$$n = \frac{C_L q S}{W} \tag{16}$$

where n is the load factor and q is the dynamic pressure. The lower the wing loading, the higher the load factor the aircraft can sustain, which in turn will reciprocate on the maximum turn rate that the aircraft can undergo.

5.4.2 Runway Length

The runway length is calculated for take-off and landing. The take-off runway length is the sum of the lengths for each step of the take-off process. The landing runway length is calculated in the same manner. The Federal Aviation Regulations (FAR) included in the Code of Federal

Regulations (CFR) sets the minimum take-off specifications depending on the type of aircraft and aircraft engines. For simplicity, the following values employed by Corke [3] are used

$$V_{TO} \geq 1.1V_s \tag{17}$$
$$V_L \geq 1.3V_s \tag{18}$$

where V_{TO} is the take-off velocity, V_L is the landing velocity, and V_s is the stall velocity.

The take-off phases include ground roll, rotation, transition, and climb. In ground roll, the aircraft accelerates from rest to take-off velocity. In rotation, the aircraft AoA increases to 80% of the maximum lifting coefficient. The aircraft velocity during rotation is the take-off velocity, and the rotation time is assumed to be a typical value of three seconds. In transition, the aircraft flies along a circular arc. The height at the end of transition is achieved when the climb angle is reached. Climbing begins after transition and ends when the aircraft reaches a certain obstacle height, which is 35 feet for commercial aircraft.

The landing phases are approach, transition, free-roll, and braking. During approach, the aircraft descends at constant velocity from a height of 50 feet to the transition height. In transition, the aircraft flies along a circular arc while the aircraft velocity decreases. During free-roll, the aircraft flies at a constant velocity. The free-roll time is assumed to be three seconds by convention. Braking is the deceleration of the plane on the runway, and is governed by the take-off ground roll equations.

5.4.3 Stability and Control

This section conceptually explains the control system for the six degrees of freedom of the SBiDir and rotation for mode change from subsonic to supersonic and vice versa. The detailed design of the control systems will be left for future study, and is not conducted in this Phase I research, which is focused on sonic boom and aerodynamic performance.

Figure 12 shows the placement of four flaps on SBiDir, two for subsonic control and two for supersonic control. The description on how the flaps should be used applies for both subsonic and supersonic mode. Therefore, the description on how each type of motion is achieved will only refer to two flaps, which are the two activated flaps for the mode under which the aircraft is flying.

Figure 13 shows a special split flap, which is the type of control surface that will be used along the trailing edges of the wing for both subsonic and supersonic mode. It should be noted that this split flap is not the one commonly defined in literature. The split flap proposed in this case has a top and a bottom section, each with the capability to move independently of the other section. Each section moves independently in order to compensate for the lack of a vertical stabilizer (i.e. rudder) in this design. This type of flap is similar to the split rudder of the Space Shuttle which acts as a speed brake. This type of response is the one desired to control yaw without affecting pitching or rotation. Therefore, SBiDir-FW is required to use a state-of-the-art fly-by-wire control system due to the complexity of the use of the control surfaces.

As of now, only two split flaps will be required for each mode where each flap will be placed on both sides of the wing like a usual aircraft wing. Therefore, a total of four flaps must be placed on the SBiDir-FW for full motion control. Only the two corresponding flaps for each mode will function at their corresponding mode and the other two flaps will be locked and unavailable.

The first type of motion to be addressed is pitching. To control pitch, the flaps on both sides of the wing must be used in the following manner: to move the nose up, only the top portion of both flaps on the wing must be used; to move the nose down only the bottom portion of both flaps must be used. To control yaw, the following procedure must be used: to turn counterclockwise, both top and bottom of only the flap to the left of the flying direction must be used; to turn clockwise, both top and bottom of only the flap to the right of the flying direction must be used. Ultimately, rolling is achieved by the following system: looking from the front towards the back, to rotate counterclockwise (left roll), only the bottom of the flap to the left of the flying direction and only the top of the opposite flap must be used; to rotate clockwise (right roll), only the bottom of the flap to the right of the flying direction and only the top of the opposite flap must be used. While this is a simplistic description on how to maneuver SBiDir, fly-by-wire controls must make up for the other aerodynamic moments affecting the motion desired. The above short description on how to maneuver the SBiDir is standard, yet sufficient to understand how to perform basic maneuvers.

In order to improve the aerodynamic efficiency of the aircraft in subsonic flight, winglets will be created by bending a small section of the wingtips for the subsonic mode. The winglets will be activated to a near-vertical position only during subsonic flight. This feature will reduce the lift-induced drag of the aircraft and improve overall subsonic aerodynamic efficiency. Controls will cause the winglets to deactivate and revert to a horizontal position flush with the wing when needed in preparation for supersonic flight. This deactivation will be complete before the rotation to supersonic mode is initiated so that aerodynamic issues during the mode change are minimized.

Two canards, one on each side of the front of the aircraft close to the nose, will be activated during supersonic flight. They will serve as horizontal stabilizers for longitudinal control and stability. The main advantage of the canard configuration is that it acts to counter the pitching moment generated by the main wing while being used as a lifting surface, therefore improving overall aerodynamic efficiency.

Vertical tails are typically used for stabilization. However, their usage should be avoided for the SBiDir aircraft because there would be a drag penalty. Alternatives that can be used to improve stability and control include vortex flow control and thrust vectoring. The X-29 aircraft, a joint venture between NASA and Northrop Grumman, employed two nozzle jets on the forward upper part of the aircraft nose for vortex flow control. In the 60 tests that were conducted, the results showed that higher-than-expected yaw forces were created. The process is as follows: Air is exhausted through the right nozzle to accelerate the right vortex flow. The left vortex is then pushed away from the body. As a result, there is a lower pressure on the right side of the body, which causes a right yawing motion of the aircraft. Thrust vectoring has been employed in fighter jets to achieve better maneuverability. This concept employs mechanical parts to rotate nozzles. The nozzles rotate, which affects the direction of the exhaust. With this capability, the aircraft does not have to rely solely on the control surfaces such as flaps to facilitate movement. A current field of research is flow thrust vectoring that uses injection nozzles. With this system, flow is injected to control the exhaust vector. The flow thrust vectoring system does not require mechanical parts, so it is simpler and lighter than a typical thrust vectoring system.

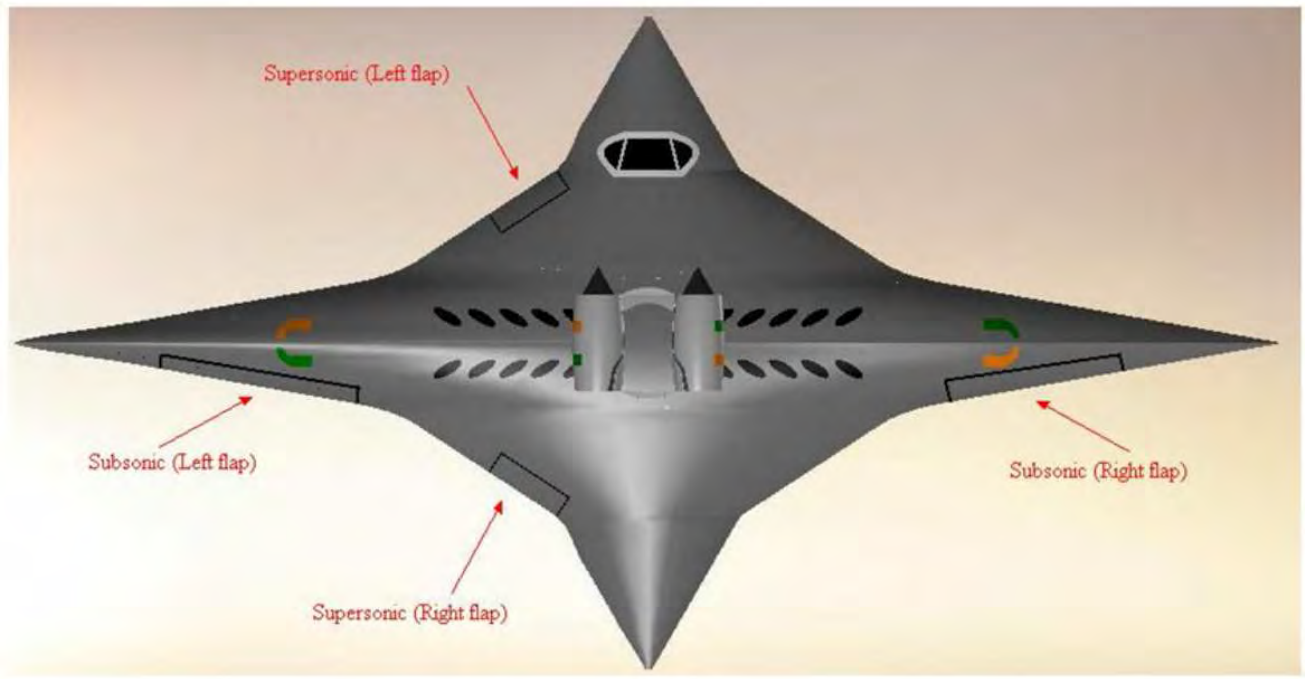

Figure 12: Location of control surfaces supersonic and subsonic modes. Also, winglets (not shown) will be used for subsonic flight and canards (not shown) for supersonic flight to aid control and stability.

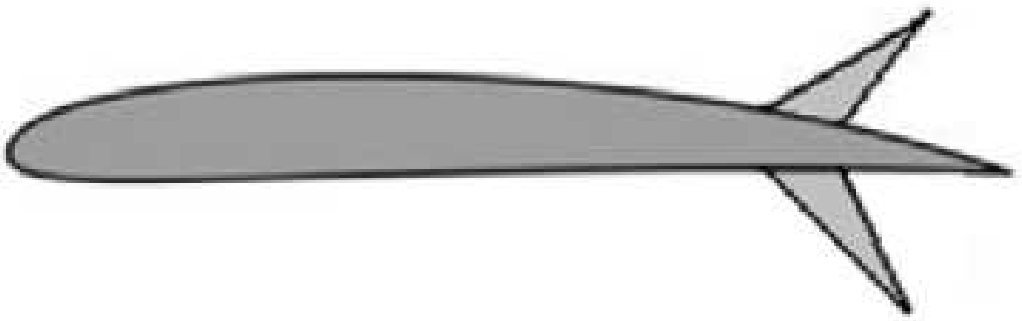

Figure 13: Sketch of split flap required for controlling the six degrees of freedom of SBiDir-FW. Top and bottom flaps move independently of each other.

5.4.4 Mode Change

The operation for yawing control as described in section 5.4.3 is applicable to the mode change from subsonic to supersonic and vice versa and maintain the propulsion thrust in the flight direction. The transition should occur at a high subsonic Mach number with sufficient dynamic pressure, but no shock waves to avoid the instability caused by shock waves. Two ideas of rotation transition are proposed conceptually, but not studied in this Phase I study since it is beyond the scope of Phase I and will be studied in Phase II.

The first idea is that the engines will be mounted on a circular platform with a raised cross at right angles. Each leg of the cross will be positioned between two panels to prevent unwanted rotation. A mechanism will be employed to remove both panels leaving the circular base to rotate freely. As soon as the leg clears the path of the panel, the right panel (counter clockwise rotation) or the left panel (clockwise rotation) will be replaced. Once the next leg reaches the replaced panel it will be prevented from moving further and the other panel will be put back locking the leg in place and ensuring a rotation of only 90°.

The second idea is to employ an electromagnetic system that prevents the circular disk from moving when employed but leaves it free to rotate when disabled. The system can be hooked up to a computer that is programmed to know when the wing is in the correct position. The system will release the disk and allow it to rotate freely while it gradually increases the strength of the magnetic system, eventually bring it to a stop when the wing has rotated 90°. Either system or a combination of both systems can be employed to ensure proper rotation from subsonic to supersonic mode, and vice versa.

The time required for the transition between modes can be controlled to be about 5 to 10 seconds or longer. Such a transition time length appears to be short enough so that from an inertia point of view neither momentum nor lift should be affected. Considering the effect of the transition on the passengers' comfort, for the chair furthest from the axis of rotation a maximum centrifugal acceleration will be controlled to be less than 0.3g, which is comparable to that felt at the transition phase of take-off (approx. 0.15g). As a result, passenger discomfort will not be expected.

5.5 Material Selection

When flying at supersonic speeds, the outer surface of an aircraft has high temperatures that can weaken the aircraft. For a cruise speed of Mach 1.6, the approximate maximum temperature is below $100°C$, so materials that can withstand high temperatures are desirable. The weight and cost of a material is also a key consideration. A lighter material results in a greater payload and better fuel efficiency.

Aluminum is the most frequently used material for aircraft structures. It exhibits good mechanical and thermal properties and is relatively cheap. The most commonly used aluminum alloy is Duralumin, Al 2024. Some metal alloys including titanium and stainless steel have the required thermal and mechanical properties for a cruise speed of Mach 2.0. However, metal alloys are heavy which negatively affects the performance of the aircraft. In addition, their performance at slightly higher speeds (higher temperatures) is not acceptable.

In the literature, composite materials are commonly chosen for aircraft structures due to their light weight and good thermal and mechanical properties. Composite materials consist

of a matrix (resin) and fibers. Epoxy resin is the most commonly used and has a maximum temperature limit of $180°C$. Due to the need for a factor of safety the actual temperature limit for usage is about $130°C$, above the approximate maximum temperature for the SB-8060-3 outer surface. Typical fiber materials include graphite, aramid, boron, and fiberglass. Graphite is the most popular material for primary structures, and fiberglass is generally used for secondary structures. Composites cost more than metal alloys, so a combination of materials including various composites and metal alloys must be used to satisfy performance and cost concerns for the SBiDir. For example, a graphite-epoxy composite can be used for the highest temperature areas of the aircraft, but it costs about 20 times more than aluminum. As a result, composite materials cannot be used for the entire airplane structure. Metal alloys should be used for areas where the conditions do not require composites in order to balance the cost and weight considerations. To select specific materials for each part of the aircraft, a heat transfer analysis of the surface of the aircraft is needed.

6 Validation of Sonic Boom Simulation

As the first step, it is necessary to validate our sonic boom simulation tools. Simulation of sonic boom using CFD needs to emphasize on the off body phenomenon, which has different mesh requirement from predicting aerodynamic forces of an airplane[69]. The cone Model 1 in the NASA sonic boom wind tunnel testing[70] is used to validate the CFD mesh setup and numerical schemes selection. The half cone angle is 3.24°, the cone length is 2inch. The tested Mach numbers 2.01 is calculated numerically for its near field sonic boom signature. The computed results are compared with the experiment[70] and the inviscid Euler results of Wintzer et al[71].

The cone Model 1[70] is simulated using inviscid Euler solver in the FASIP code with full geometry and a cross section of the mesh is shown in Fig. 14. The numerical schemes used is the the 3rd order MUSCL scheme[44] with Roe's approximate Riemann solver[48]. The mesh is inclined at the Mach angle to resolve the oblique shock waves. The computational domain size is extended one chord upstream, two and a half chords above and below the cone, and four and half chords downstream of the cone. The inlet boundary conditions is to fix all the variables at the free-stream conditions. The upper, lower, and downstream conditions are zero gradient extrapolation. The rear part of the cone with constant radius cylinder is extended to the exit boundary for the simplicity of boundary condition treatment. The baseline mesh is $201 \times 141 \times 61$ in the streamwise, radial and circumferential direction respectively, which results in a total grid points of 1.73 million.

Fig. 15 is the near field pressure signature at $H/L = 2$, where H is the vertical distance from the cone leading edge and L is the cone length. Fig. 15 shows that the present computed pressure signature agrees excellently with the computed results of Wintzer et al [71], which has been validated with experiment. Fig. 16 is the extrapolation to $H/L = 10$ using the NASA *NF Boom* code[68] and excellent agreement with the experimental measurement is achieved. Fig. 17 is the pressure contours of the cone Model 1 at incoming Mach number of 2.01. Fig. 18 is the mesh refinement results and shows that the over pressure signatures are identical with different sizes of meshes. The refined mesh is $331 \times 222 \times 101$, a total of 7.42 million grid points. It indicates that the over pressure signature computed using the baseline mesh is converged.

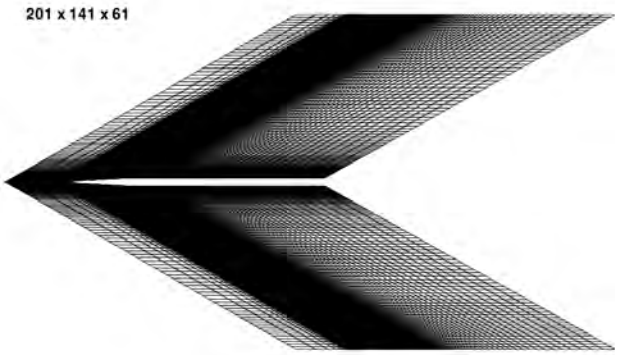

Figure 14: Cross section of the mesh for NASA cone Model 1[70].

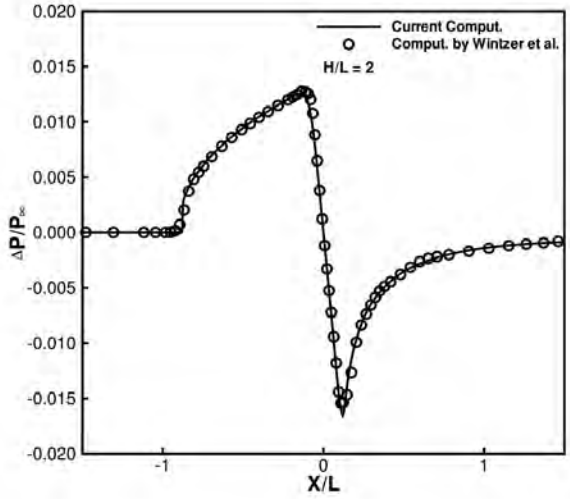

Figure 15: Computed Over-pressure at two body lengths below the cone Model 1 compared with the result from[71].

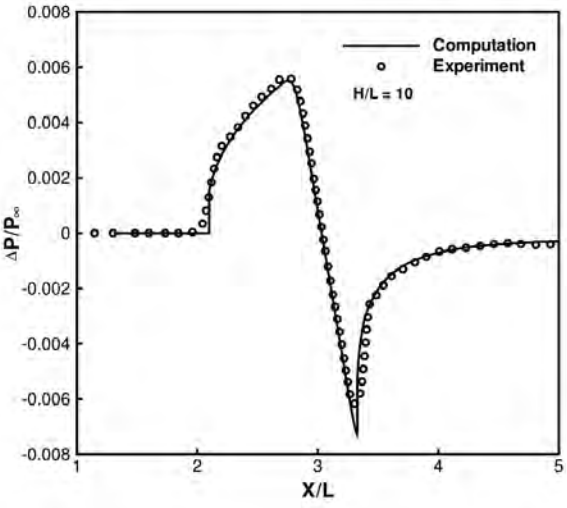

Figure 16: Computed Over-pressure at ten body lengths below the cone Model 1 compared with experiment[70].

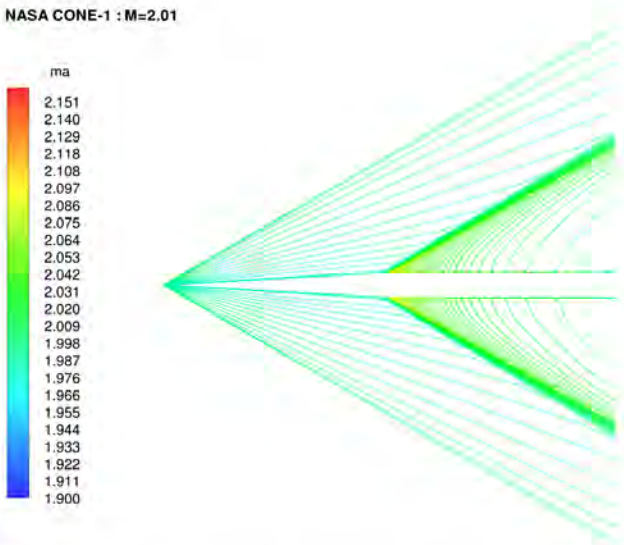

Figure 17: Computed pressure contours of the cone Model 1.

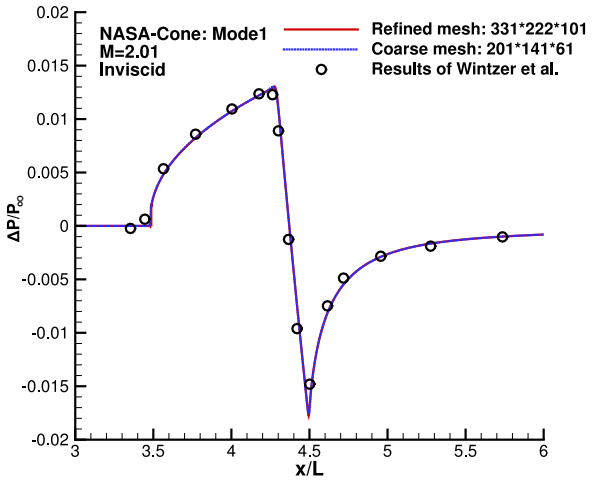

Figure 18: Comparison of the computed over-pressure at two and half body lengths below the cone Model 1 for mesh refinement study.

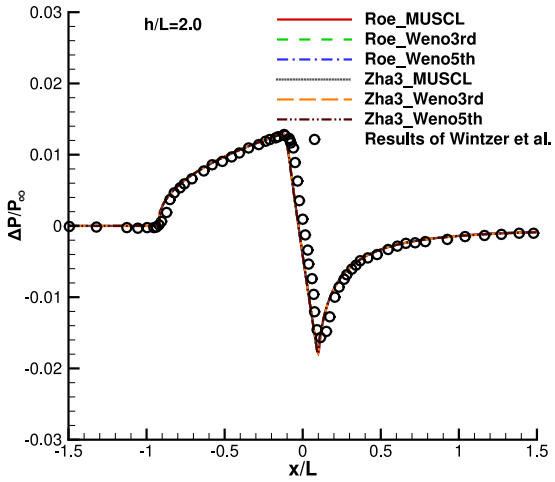

Figure 19: Comparison of the computed over-pressure at two and half body lengths below the cone Model 1 using different schemes.

To further validate that the solution is also independent of the numerical schemes, additional schemes in the FASIP code are tested, including 3rd order MUSCL scheme[44] with the low diffusion E-CUSP scheme of Zha et al(labeled as Zha3 in the plots) [49], 3rd order and 5th order WENO schemes[41, 42] with Roe's approximate Riemann solver [48] and the low diffusion E-CUSP scheme of Zha et al [49]. The near field over-pressure at $H/L = 2$ computed by above different schemes is given in Fig. 19, which shows that all the different schemes achieves virtually identical results.

Above results indicate that the CFD simulation and far field wave propagation tool are suitable for the sonic boom analysis. The same numerical strategy is used to simulate the SbiDir-FW configurations in this research.

7 Proof of Concept by Trade Study

Since SBiDir-FW is a new concept, no prior knowledge on the correlation between the geometry and sonic boom and aerodynamic performance is available. Due to the time limitation, this Phase I study focuses on conducting parametric trade study to develop such a correlation. A trade study is to vary one design parameter by hands and keep all other parameters unchanged to see the effect of that particular parameter. The best design from the trade study within a very limited design space will be used as the proof of the concept. In other words, a systematic automated design optimization with stochastic and gradient based methods to change multiple parameters may further improve the design significantly. However, it is extremely important to conduct the manual trade study first to understand the physics and the relationship between the geometry parameters and sonic boom and aerodynamic performance. The automated design optimization should be only used as a tool under the guidance of the aerodynamic physics, not the ultimate goal. Otherwise, the whole course may be misled. Automated design optimization will be conducted in Phase II research.

7.1 Mission Requirements

To achieve designs that are realistic, a mission is assigned to impose the constraints of pay loads, volume, size, weight, etc. The initial mission goal for Phase I study include:

Cruise Mach number of 1.6,
100 passengers and their luggage as the pay load,
Range of 4000nm,
Fuel efficiency measured by passenger*mile/lb fuel ≥ 3,
Ground sonic boom loudness $\leq$ 75dBPL
Minimum supersonic aerodynamic efficiency L/D ≥ 8
Minimum subsonic aerodynamic efficiency L/D ≥ 18

All the above initial mission requirements are met or exceeded based on the numerical simulations in Phase I. More design optimization will be conducted in Phase II to further improve the design with wind tunnel testing to validate the results.

7.2 Mesh

The mesh is constructed using the H-mesh topology in order to achieve high quality around the sharp LE and TE of the airfoils. The mesh displayed Fig. 20 uses a total of 301 points placed around airfoil, 81 in the spanwise direction, and 161 points in the direction normal to the wing surface. Total mesh size is 3.93 million points, partitioned into 40 blocks for the parallel computation. A refined grid is constructed using 1.5 time more points in each direction with the total grid points of 13.3 million. The baseline mesh and refined mesh results show good agreement.

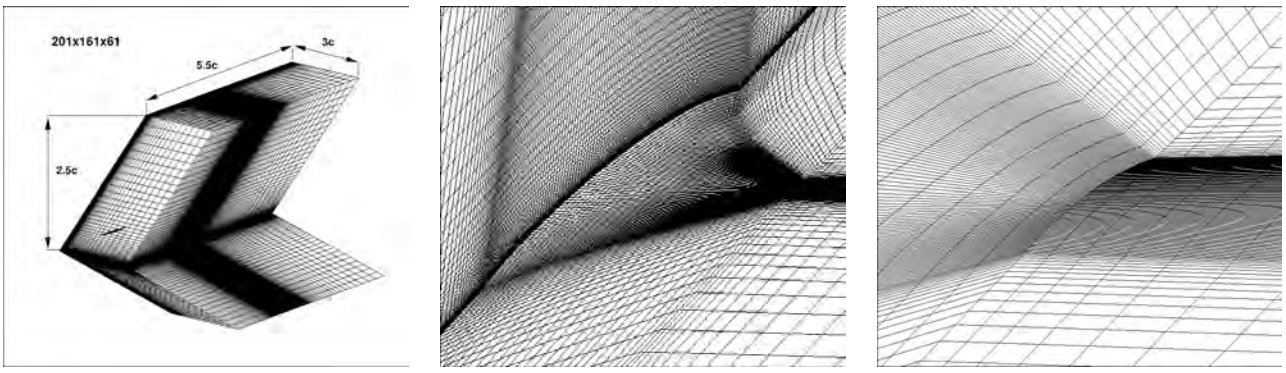

Figure 20: SBiDir mesh topology, outside mesh (left), suction surface (middle) and wing tip (right).

A large amount of trade studies are carried out. The following sections only show some of them to demonstrate the features of SBiDir-FW concept.

7.3 Sweep and Dihedral Angle Study

The sweep angle needs to be determined first to form the planform shape, which decides the aspect ratio at supersonic and subsonic. Aspect ratio is critical to determine the lift, drag, aerodynamic efficiency of L/D. For supersonic flight, a high sweep angle is always desirable since it generates low shock strength, sonic boom, and wave drag. As an example of extreme, a sweep angle of 89° will be basically a 2D airfoil slice with tiny span width and will generate acoustic wave with no sonic boom. However, it is useless since there is no volume to hold passengers and fuel. In general, decreasing the sweep angle to a certain extent within the Mach cone will increase supersonic aspect ratio, planform area, volume, lift, wave drag, ratio of lift to drag, shock wave strength, and sonic boom. To satisfy the mission requirement, a high L/D and sufficient lift coefficient is required, and a lower sweep angle is preferred. However, a lower sweep angle will increase the aspect ratio, make the planform less slender, and increase sonic boom. In simple words, a very slim planform is beneficial to reduce sonic boom, but being too slim will not have enough lift and volume to fly the mission. So there is a balance between the required aerodynamic performance for the mission target and the low sonic boom goal.

The table in Fig. 21 gives two different sweep angle design examples at the early stage of this research, namely D84TW and D82S4. The two designs have constant sweep angle of 84° and 82° respectively with diamond shape planform.

	General characteristics, M=1.6, L=100m												
Design	Area (m^2)	AR sup	AR sub	Passen-gers	TO weight (klb)	Alt (kft)	Ground Boom (dBPL)	L/D, M>1	L/Dp	CL	L/D, M<1	Range (nm)	Pass*mile / lb fuel
	706	0.28	14.16	100	191.5	42	81.6	6.48	19.11	0.0363	12.5	3000	3.58
D82S4													
D84TW	528	0.20	18.94	60	110.7	42	63.8	5.50	18.73	0.0296	N/A	2500	3.11

Figure 21: Performance of Design D84TW and D82S4.

Fig. 22 shows the Mach number contours on the suction and pressure surface, which also displays the slim planform shape. Fig. 23 is the Mach number contours at different span, indicates that there is a shock wave going upward on the suction surface and an expansion wave going downward. The airfoil used to stack the wing is simple circular arc airfoil with linear meanline angle distribution. The thickness varies from 2.2% in the 0% span to 0.5% span in the tip. The surface isentropic Mach number distributions at different span shown in Fig. 24 indicates that the region near tip is highly loaded and near center is lightly loaded. A more even loading distribution will be more desirable.

Fig. 25 is the lift and pressure drag coefficient variation with AoA. The lift is almost linearly increased with increasing AoA. The pressure drag grows slower at low AoA and increases more rapidly at high AoA. The pressure drag is over a order of magnitude smaller than the lift and yields a L/D_p about 19 (Fig.21) at AoA=3°. However, since the surface friction drag primarily depends on Mach number and Reynolds number, the friction drag is more dominant and brings the overall L/D down to about 5.5 as shown in Fig. 22. The volume of D84TW only allows it to carry 60 passenger and the range is 2500nm due to the moderate L/D. The flight altitude is 35kft to gain freestream density to compensate the low lift coefficient.

Such a slim planform gives smooth ground sonic boom signature as shown in Fig. 26, 27, and 28 as the 2 body below over-pressure signature, ground over pressure signature, and ground boom loudness. A smooth *Sine* shape ground boom signature is obtained with boom loudness below 70dbPL.

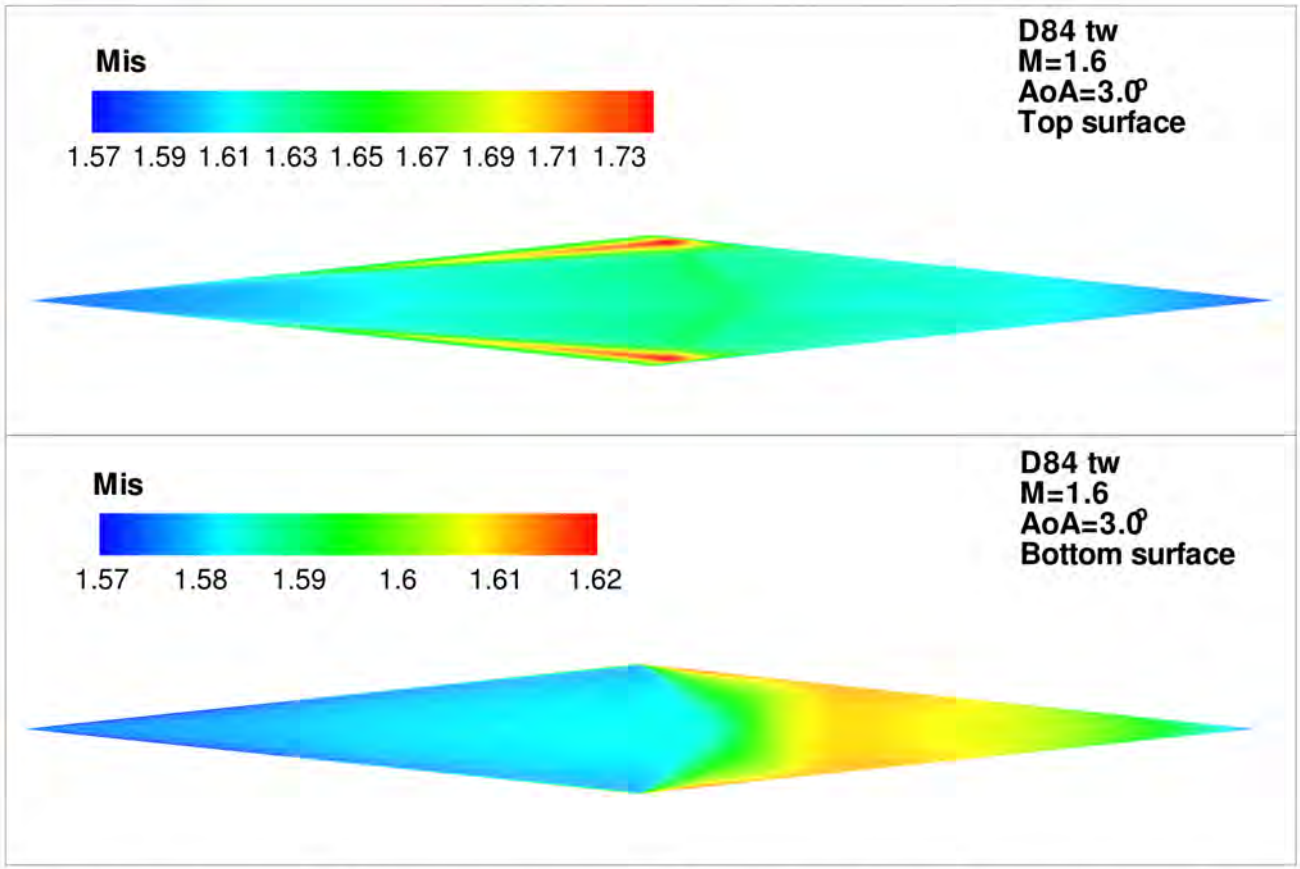

Figure 22: Isentropic Mach number contours of D84TW at AoA=3°, top: suction surface, bottom: pressure surface.

Decreasing the sweep angle to certain extent within the Mach cone will increase aspect ratio, the slope of lift vs AoA, and hence lift coefficient and L/D at the same AoA. Since the D84TW's lift coefficient and L/D are not sufficient to carry 100 passengers for the range of 4000nm, a design with sweep angle of 82°, D82S4, is conducted. Fig. 29 is the D82S4 Mach contours of the suction and pressure surface and shows the planform shape.

As shown by Fig. 21, decreasing the sweep angle by 2° from 84°, the aspect ratio is increased by 40% from 0.2 to 0.28, the planform area increased by 34%. At the same AoA=3°, the lift coefficient is increased by 23%, L/D increased by 18%. The volume increase is sufficient to carry 100 passengers with the range increased to 3000nm. Even though the ground boom signature shape is still *Sine* shape wave. The ground boom loudness is increased to 81dbPL from flight altitude of 42kft. In general, a low sweep angle will give better L/D, but stronger sonic boom.

To further increase L/D without considering much the sonic boom, a variable sweep is more beneficial to have lower boom and low wave drag as shown by design D84-68.11 in Fig. 30, which has a variable sweep distribution from 84° at the very leading edge to 78° at the wing tip. The supersonic aspect ratio is increased to 0.632 with the lift coefficient of 0.086 as shown in Table

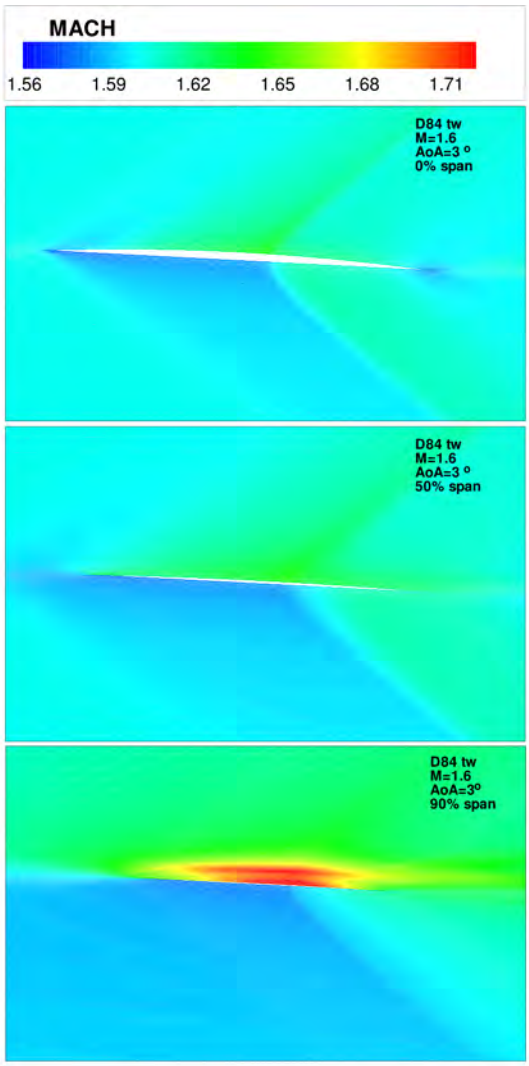

Figure 23: Isentropic Mach number contours of D84TW at different span location, AoA=3°.

1. The L/D is astonishingly high up to 10.45. Due to the increased L/D, volume, and planform area, this airplane can carry 200 passengers for 5000nm at altitude of 56kft with a strong ground sonic boom loudness of 101.64dbPL and a N-wave. To keep the same mission of 100 passengers with the range of 4000nm, the flight altitude is ??? with the ground boom loudness of ???dbPL.

Table 1: Geometry information

Length(m)	Span(m)	Area(m^2)	Volume(m^3)	AR(subsonic)	AR(supersonic)
100	23.7	891	585	11.23	0.632
Cl	Cd	Cl/Cd			
0.08613	0.00824	10.453			
Altitude(ft)	30000	40000	50000	56000	
Noise(PLdB)	111.12	106.38	101.64	99.08	
Cl required					

Due to the time limitation of Phase I research, no optimization of sweep angle is conducted.

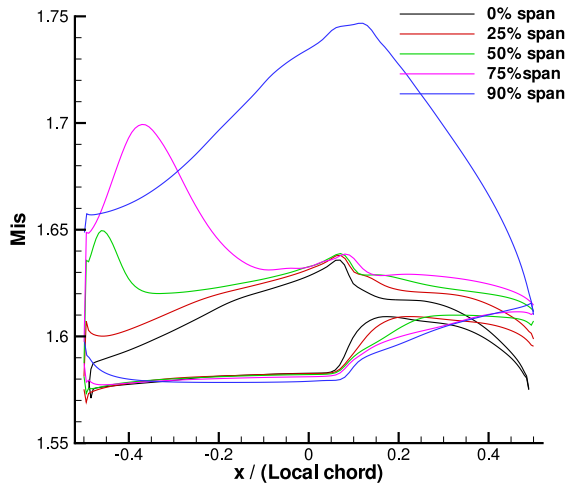

Figure 24: D84TW surface isentropic Mach number distributions at different span location.

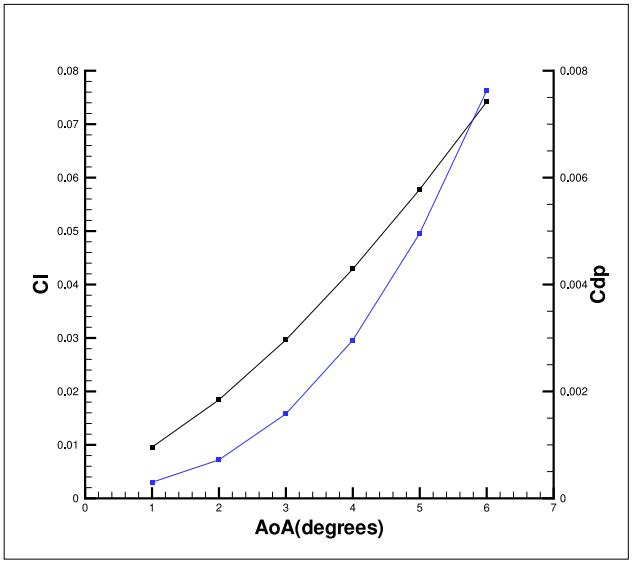

Figure 25: D84TW lift and drag coefficient vs angle of attack.

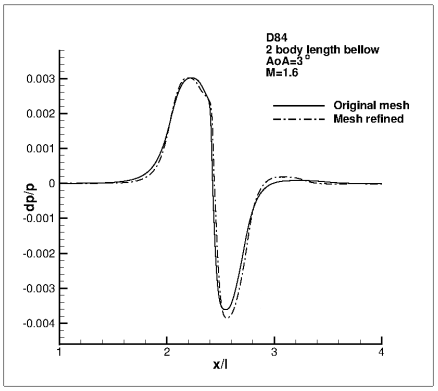

Figure 26: Over pressure 2-body below.

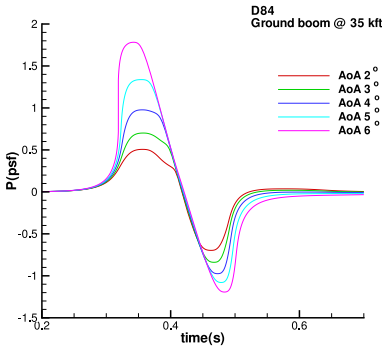

Figure 27: Ground over pressure.

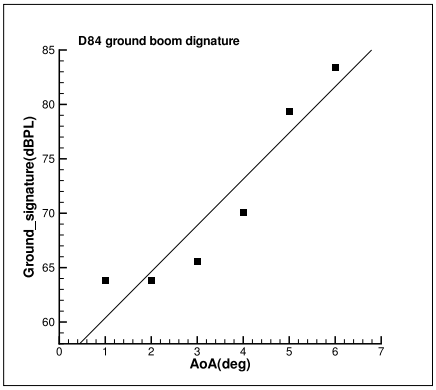

Figure 28: Ground boom loudness, Alt=35kft.

This trade study is to understand the sensitivity of sweep angle to the aerodynamic and sonic boom performance. The general conclusion is that a lower sweep angle will give high L/D and high sonic boom. The L/D of 10.45 and the sonic boom achieved in this study is believed to still have a lot of room to go and is definitely not the limit. More effort to improve this design will be continued. An optimal sweep angle distribution needs to be studied in Phase II systematically.

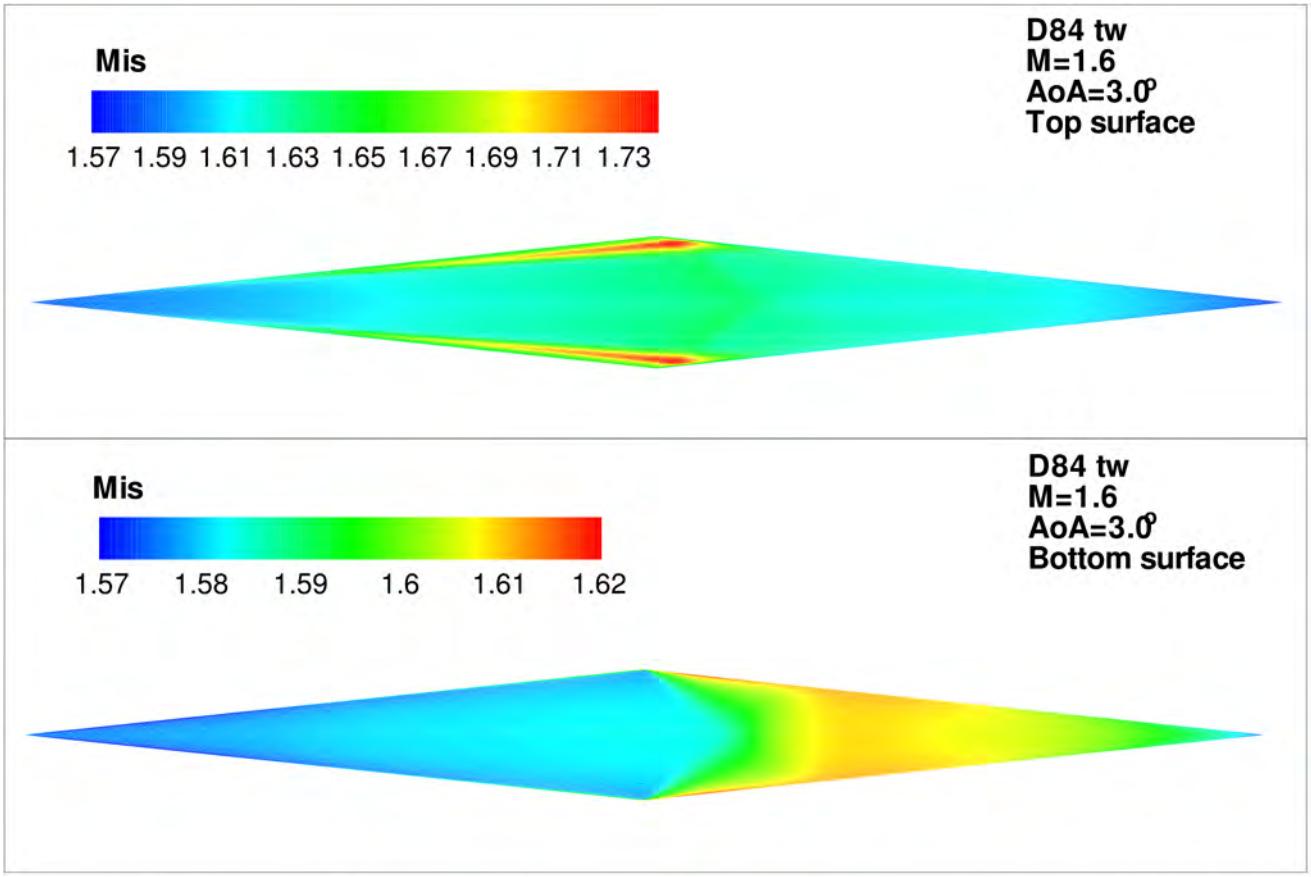

Figure 29: Isentropic Mach number contours of D84TW at AoA=3°, top: suction surface, bottom: pressure surface.

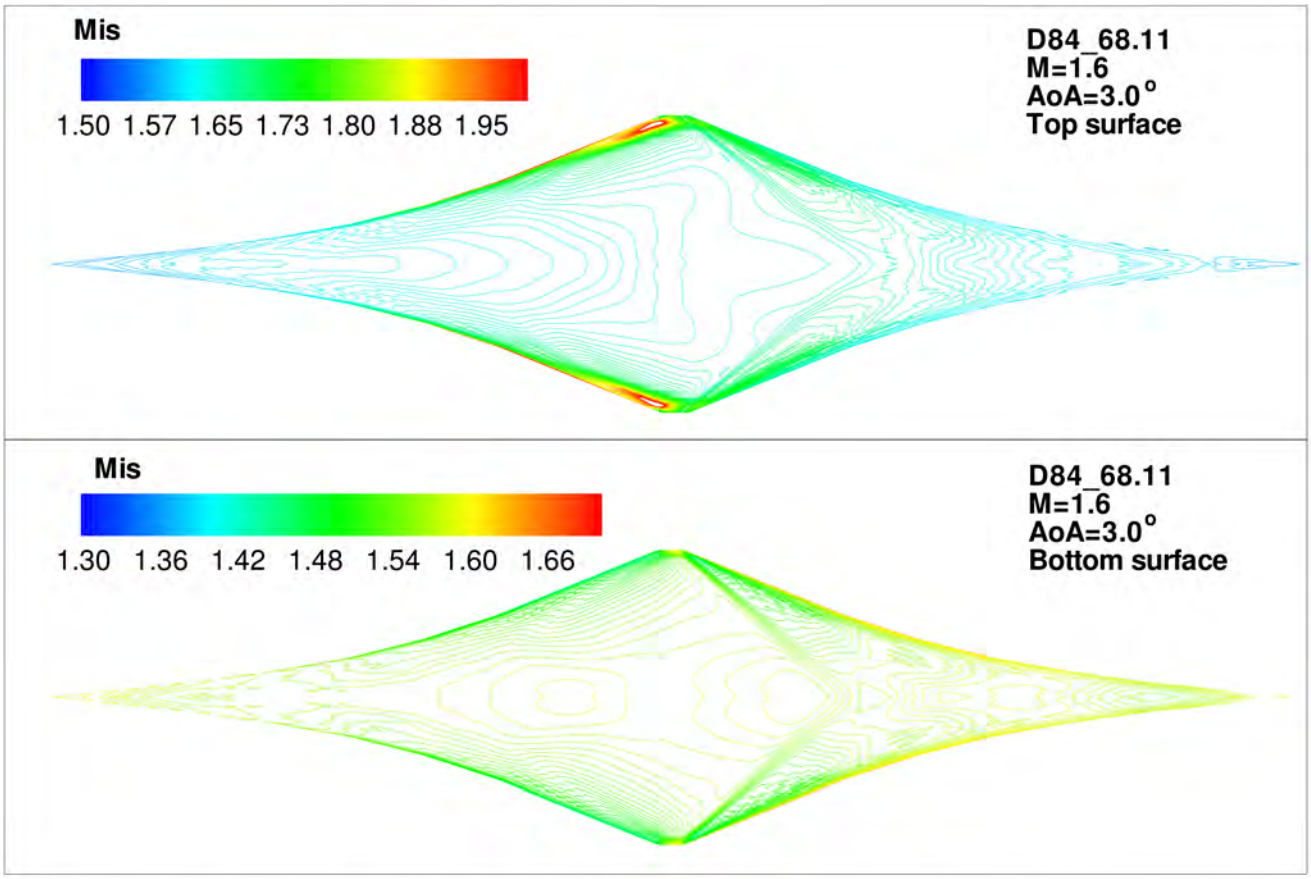

Figure 30: Isentropic Mach number contours of D84-68 at AoA=3°, top: suction surface, bottom: pressure surface.

7.4 Meanline Angle Distribution Study

To further reduce sonic boom with increased L/D, the meanline angle distribution is found to be the most effective way to control shock strength. The meanline angle distribution can be varied for each airfoil section to adjust the flow incidence at leading edge, control the loading distribution along the chord, and hence control the shock strength. The basic strategy is to remove the surface shock waves in order to provide a favorable near field over-pressure signature, which will further reduce the ground sonic boom level. The total meanline angle variation from LE to TE stands for how much the flow is turned by the airfoil, which determines the total lift or loading of the airfoil.

In this study, all other design parameters including sweep angles, dihedral angles, airfoil thickness, leading edge (LE) and trailing edge (TE) thickness are held unchanged. A variable sweep from 84° to 78° is adopted to increase the aspect ratio to 0.355 in order to further increase L/D up to 8.4. Again, many design trails are conducted and only three of them are presented in this section to demonstrate the effect.

As comparison, Fig. 31 presents three different meanline angle distributions at zero span airfoil, which is found to have the most impact on the sonic boom due to its longest chord length in the flying wing planform. The airfoil has the same flow turning from LE to TE. In other words, each airfoil will have about the same loading or lift, but the loading distribution along the chord is different. All meanline angle distributions are symmetric about the 50% chord location to ensure the symmetry requirement of SBiDir-FW concept. The left plot in Fig. 31 is a linear distribution from LE to TE, which represents a circular arc airfoil. For an ideal 2D supersonic flow, a linear meanline angle distribution means the flow on the suction surface will have uniform expansion from LE to TE, and the flow on pressure surface will have uniform compression. For 3D wing with high sweep angle, the flow has some similar feature, but is altered significantly since the flow pressure needs to return to ambient pressure after TE.

The middle plot in Fig. 31 has a nonlinear distribution with half of the total turning imposed on the first 25% of the chord, almost no turning from 25% to 75% chord, and another half turning imposed at the last 25% chord due to the symmetry requirement of the airfoil geometry. Even though the middle plot has nonlinear loading distribution, the turning is reduced monotonically from LE to TE. The right plot in Fig. 31 also has nonlinear distribution similar to the middle plot, but with more enhanced turning effect in the first and last 25% of chord that the meanline angle distribution becomes non-monotonic. Such non-monotonic meanline angle distribution is successfully applied to remove shock waves for a transonic compressor blade with supersonic inlet Mach number by Hu et al[38].

Fig. 32 is the comparison of surface isentropic Mach number distribution at different span, the black line is for the linear meanline angle, red for the monotonic, and blue for the non-monotonic. The typical surface isentropic Mach number distribution on the suction surface and pressure surface appears to be fairly symmetric as shown by the linear distribution case(black line). That is, while the flow on the suction surface expands and accelerates , the flow on the pressure surface is compressed and decelerates. They reach the highest and lowest peak at the same location. Then the flow on suction surface goes through a shock wave and the flow on pressure surface goes through a rapid expansion wave. The flow on suction and pressure surface meets the ambient pressure at the trailing edge.

Changing the meanline angle distribution from the linear to the monotonic (red line) drastically changes the loading distribution, which is more uniform from LE to TE along the chord.

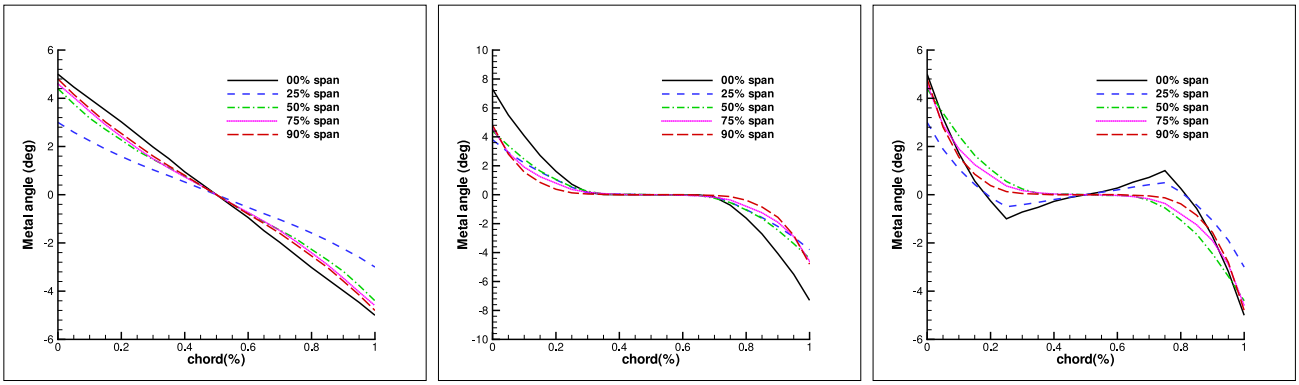

Figure 31: Three different meanline angle distributions, left: linear; middle: monotonic; right: non-monotonic.

The strength of shock wave on suction surface and expansion wave on pressure surface are significantly reduced. The non-monotonic meanline angle distribution(blue line) further reduces the peak Mach number compared with the monotonic one. The non-monotonic distribution has the same LE meanline angle as the linear one, but the flow incidence is less due to the rapid decrease of the meanline angle after the LE. The more important effect is that the high peak Mach number on suction surface is reduced and the low peak Mach number on pressure surface is increased. In other words, the shock wave on suction surface and expansion wave on pressure surface are both reduced. Such effect is maintained in most of the span until near tip, where the linear meanline angle distribution has lower peak Mach number. Applying linear meanline angle distribution near tip is hence expected to further improve the results. Table 2 to 4 summarize the performance of the three designs. Compared with the linear meanline angle distribution, the non-monotonic one reduces the lift by 10%, but gain the L/D by 3% with the value of 8.4 due to reduced wave drag by weaking the shock waves.

Fig. 33 compares the suction and pressure surface Mach number contours of the linear and non-monotonic meanline angle distribution with the exact same planform shape determined by the variable sweep. For the linear one on the left, there is a strong shock wave on the suction surface emanating from the tip. At the same location on the pressure surface, there is a strong expansion wave. The shock wave on the suction surface and the expansion wave on the pressure surface always go hand in hand to balance the pressure. For the non-monotonic one on the right, both the shock wave and expansion wave are basically removed.

Fig. 34 displays the Mach contours at different span showing the wave structures propagating in the near field. The front 60% of the airplane generates the compression wave propagating downward and expansion wave travling upward. Even though the non-monotonic meanline angle design has almost no strong waves on the wing surface, there is still an oblique shock formed on upper surface going upward and an expansion wave propagating downward because the flow has to match the pressure of ambient. Such a wave pattern is determined by the lift requirement. In other words, as long as an object generates lift regardless of the specific configuration, the wave propagating downward will have compression in front, followed by an expansion, and end with an aft compression wave to return the flow pressure to ambient. The hope is not to let the compression in the front and aft coalesce into two shock waves in order to avoid the N-wave, which has sharp pressure rise within a very short time that generates strong noise and annoyance. It is hence beneficial to let the compression occurs in a longer distance in a more graduate way

to have less compression coalesce in far field. The high slenderness of SBiDir-FW provides an advantage to prolong the compression and expansion with smaller slope. The removal of strong shock wave on suction surface and compression wave on pressure surface is to maintain a graduate variation.

The most important benefit of changing the meanline angle distribution from linear to non-linear and non-monotonic is it drastically reduces the ground sonic boom noise. Fig. 35 and 36 show the over pressure signature at 2-body below and the propagation to ground. The nonlinear meanline angle distribution has a much lower compression and expansion peak than the linear one in the near field and the pattern is maintained to far field. However, the linear design's high compression peak coalesce to a strong shock in the far field, whereas the nonlinear one remain as smooth *Sine* shape wave. Table 2 to 4 indicates that the nonlinear meanline angle distributions reduce the ground boom loudness by as much as 24-25dbPL at the flight altitude of 56kft from the linear design of 91dbPL to 67-66dbPL. At the same time, the planform shape is unchanged and the L/D is increased by 3% to 8.4.

The most important and encouraging finding from this meanline angle distribution study is the qualitative trend instead of the quantitative values, which need to be confirmed by wind tunnel experiment and eventually flight testing. This qualitative direction establishes an effective control relationship between the far field ground sonic boom with the aircraft geometry parameters based on a clear aerodynamic physics principle, which is to generate the loading distribution along a slender body with as smooth distribution as possible without strong shock and expansion waves. An optimal design can be eventually achieved with detailed efforts such as design optimization under an effective qualitative guideline.

Table 2: Linear meanline angle distribution

Length(m)	Span(m)	Area(m^2)	Volume(m^3)	AR(subsonic)	AR(supersonic)
100	15.7	690	462	14.492	0.355
Cl	Cd	Cl/Cd			
0.06284	0.00762	8.14			
Altitude(ft)	36000	40000	50000	56000	60000
Noise(PLdB)	99.68	98.45	95.28	91.14	88.38
Cl required	0.027	0.0348	0.064	0.095	0.12

Table 3: Monotonic meanline angle distribution

Length(m)	Span(m)	Area(m^2)	Volume(m^3)	AR(subsonic)	AR(supersonic)
100	15.7	690	544	14.492	0.355
Cl	Cd	Cl/Cd			
0.05810	0.00698	8.324			
Altitude(ft)	36000	40000	50000	56000	60000
Noise(PLdB)	72.40	71.75	68.85	67.28	66.16
Cl required	0.0255	0.0328	0.061	0.088	0.115

Table 4: Non-Monotonic meanline angle distribution

Length(m)	Span(m)	Area(m^2)	Volume(m^3)	AR(subsonic)	AR(supersonic)
100	15.7	690	511	14.492	0.355
Cl	Cd	Cl/Cd			
0.05628	0.00671	8.3875			
Altitude(ft)	36000	40000	50000	56000	60000
Noise(PLdB)	71.12	70.70	67.99	66.41	65.41
Cl required	0.025	0.032	0.060	0.087	0.113

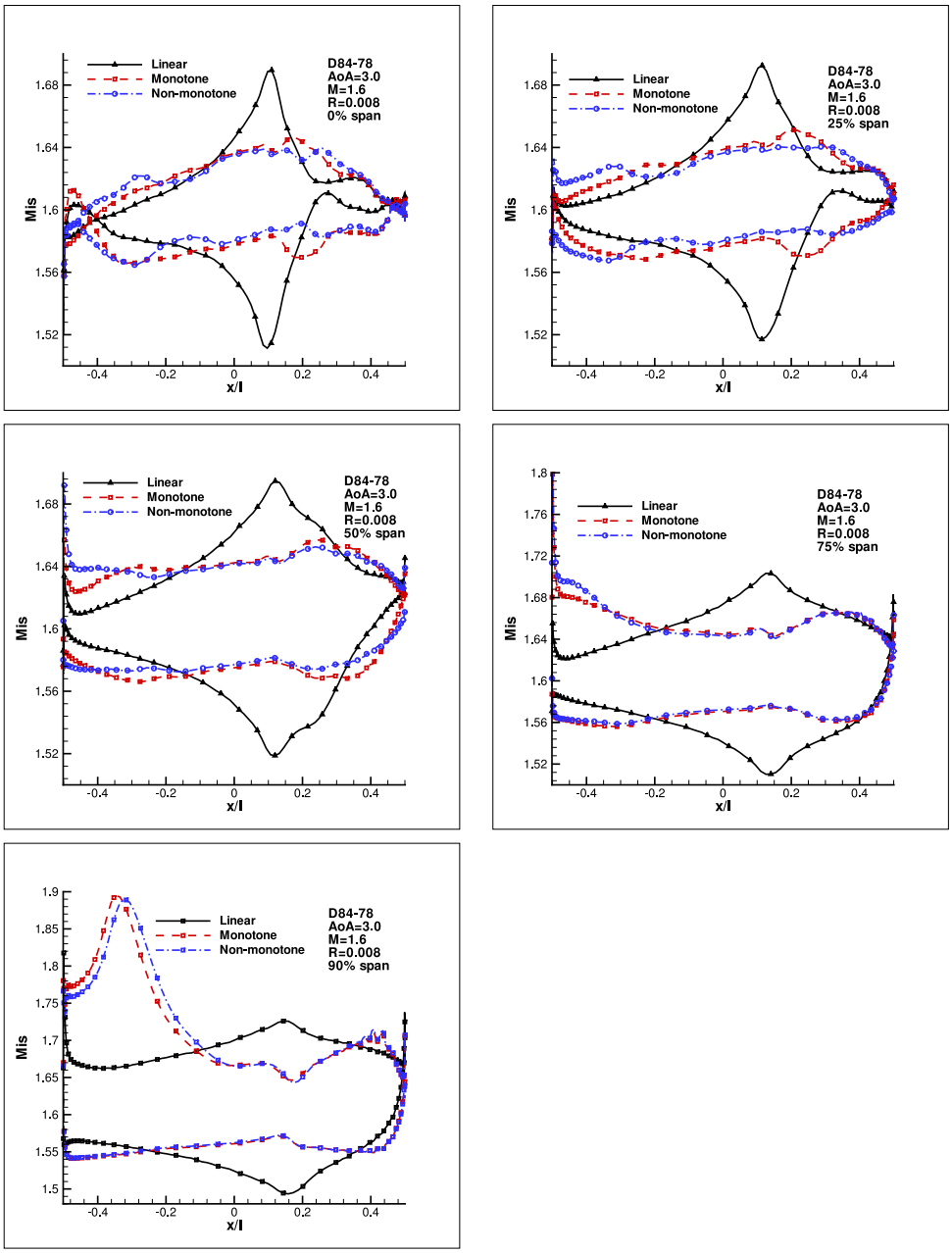

Figure 32: Wall Isentropic Mach numbers at different spans.

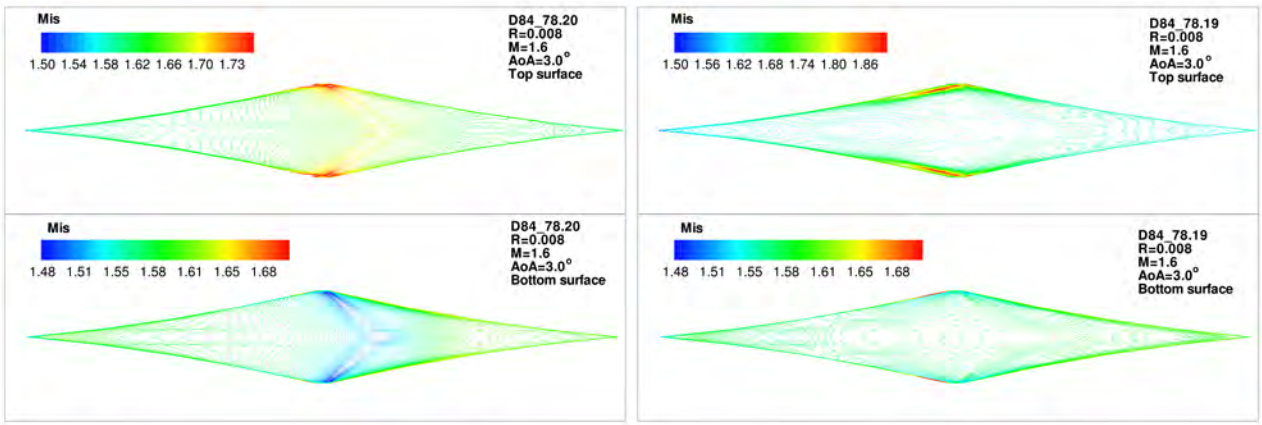

Figure 33: Comparison of surface Mach number contours, Left: linear; Right: Non-monotonic

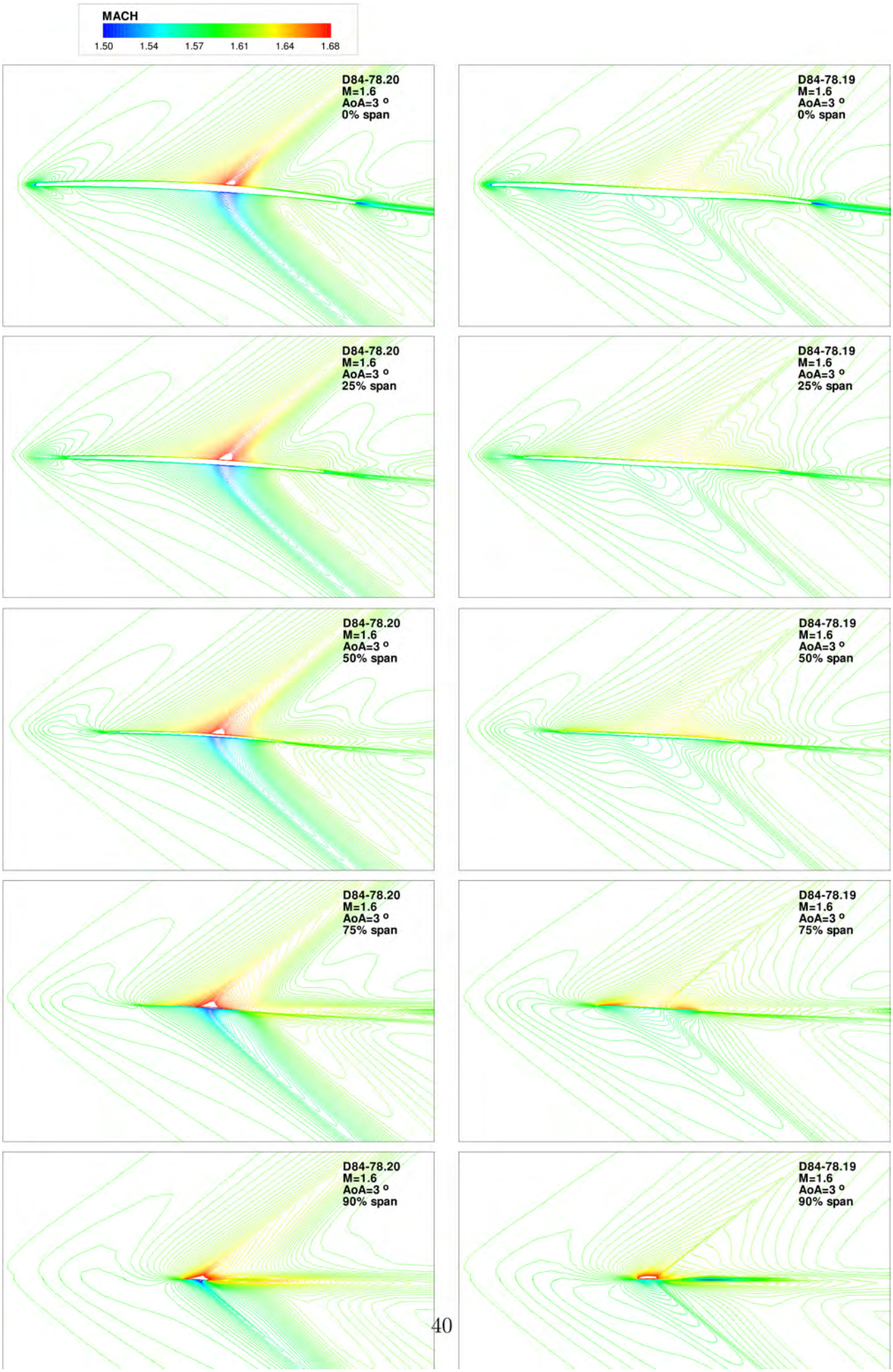
MACH
1.50
1.54
1.57
1.61
1.64
1.68
D84-78.20
M=1.6
AoA=3 º
0% span
D84-78.19
M=1.6
AoA=3 º
0% span
D84-78.20
M=1.6
AoA=3 º
25% span
D84-78.19
M=1.6
AoA=3 º
25% span
D84-78.20
M=1.6
AoA=3 º
50% span
D84-78.19
M=1.6
AoA=3 º
50% span
D84-78.20
M=1.6
AoA=3 º
75% span
D84-78.19
M=1.6
AoA=3 º
75% span
D84-78.20
M=1.6
AoA=3 º
90% span
D84-78.19
M=1.6
AoA=3 º
90% span

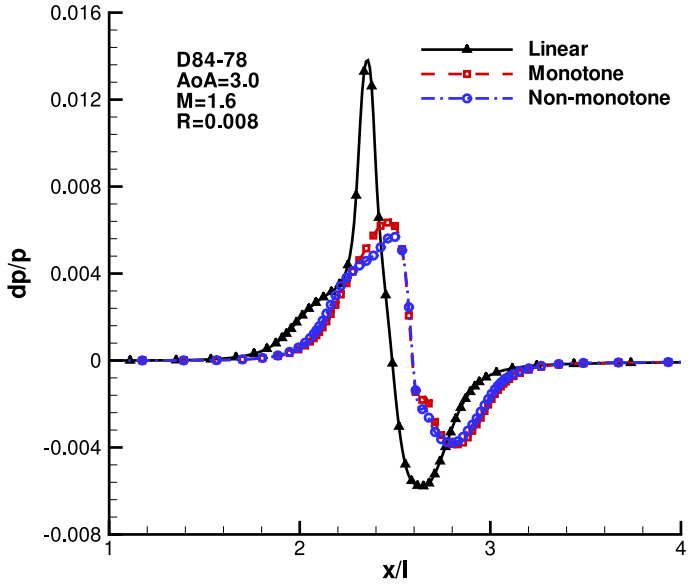

Figure 35: Comparison of overpressure signature 2 body length below the aircraft

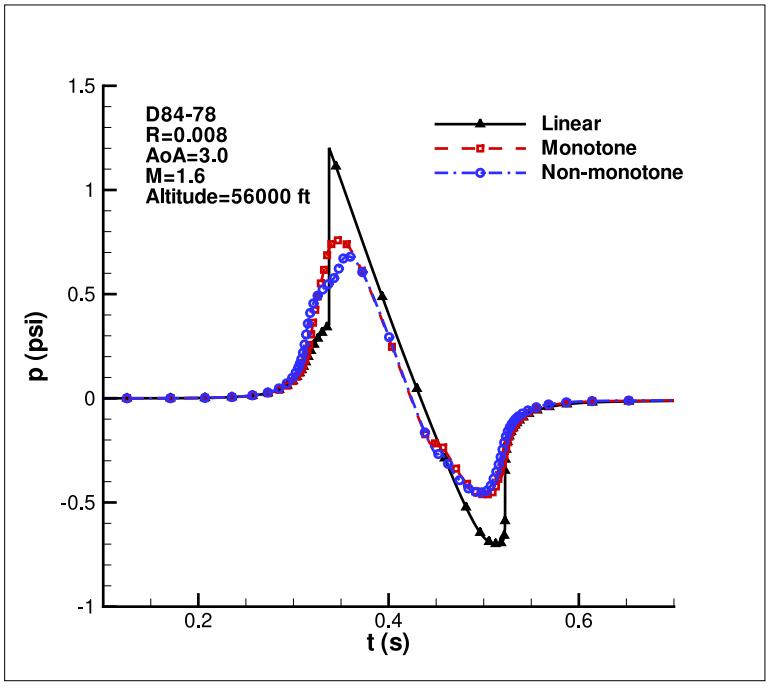

Figure 36: Comparison of ground sonic boom signature

7.5 Angle of Attack Study

The same deign D84-78.19 analyzed in above section 7.4, which has the meanline angle distributions tailored for AoA=3° to remove the surface shock wave, is conducted for trade study with AoA 1°, 2° and 4° to see their aerodynamic and sonic boom performance. Table 5, 6, and 7 summary the results, which can be compared with the results of D84-78.19 in Table 4.

Table 5 indicates that reducing the AoA to 1° decrease the L/D as expected. Fig. 38 displays the surface isentropic Mach number distributions at different span location for each AoA. At AoA=1°, the closed LE shape of the Mach number distribution at 0% span shows that the flow has a negative incidence at that location as expected. The meanline angle producing smooth surface isentropic Mach number distributions at AoA=3° does generate a shock wave on the suction surface at about 60% chord location and a strong expansion wave on the pressure surface at the same location. Such a wave structure produces a stronger ground sonic boom than at AoA=3° even though the lift at AoA=1° is lower. When the AoA is increased to 2° from 1°, the lift and L/D are increased and the sonic boom is reduced since the Mach number distribution is closer to AoA = 3°, but the boom strength is still slightly higher than the AoA=3°. When the AoA is increased to 4°, the increased incidence generates a strong leading edge downward shock that increases the boom strength.

Fig. 39 and 40 are the over-pressure signature 2-body below and its propagation to ground. Again, the near field shape is well preserved. Interestingly, the AoA=1° has the lowest wave peak, but not the least boom loudness due to the small shock wave interrupting the expansion and generates a higher noise level than that at AoA=3°, which has a higher wave peak but a smoother wave.

As aforementioned that lifting body will necessarily generate a wave signature with a compression in front, followed by an expansion, and ended with another compression. In general, the higher the lift, the higher the wave peak. This study gives an important conclusion that a higher lift at higher AoA with higher peak does not necessarily generates a louder sonic boom. If the higher peak wave is smoother with longer pressure rising time, the noise could be weaker as the case of AoA=3° compared to AoA=1°.

Fig. 41 shows the Mach number contours at different span locations for different AoA. At zero span, the overall upward shock on suction surface and downward expansion on pressure surface for the AoA=1° is weaker than the one of AoA=3°. However, on the wall surface, the AoA=1° has a stronger root of the waves than the AoA=3° case, which generates a weaker ground sonic boom loudness. Fig. 42 is the Mach number contours on the suction and pressure surface for the AoA=1° case, which indicates that the overall compression and suction are not as strong as the AoA=3° as reflected by the wave peak of the 2-body below in Fig. 39.

Table 5: AoA=1°

Length(m)	Span(m)	Area(m^2)	Volume(m^3)	AR(subsonic)	AR(supersonic)
100	15.7	690	462	14.492	0.355
Cl	Cd	Cl/Cd			
0.02602	0.00448	5.808			
Altitude(ft)	36000	40000	50000	56000	60000
Noise(PLdB)	76.88	76.64	74.73	73.41	72.44
Cl required	0.0175	0.036	0.0665	0.15	

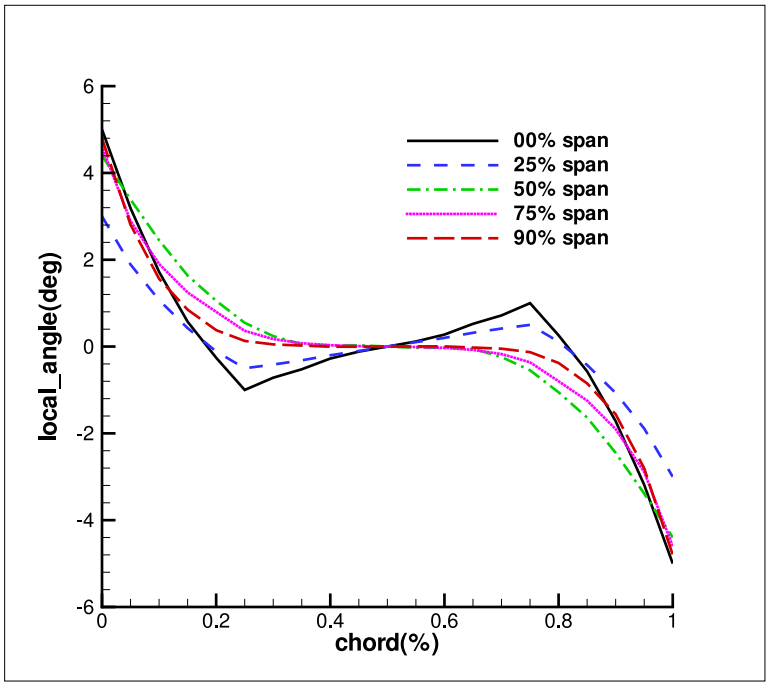

Figure 37: Meanline angle distribution.

Table 6: AoA=2°

Length(m)	Span(m)	Area(m^2)	Volume(m^3)	AR(subsonic)	AR(supersonic)
100	15.7	690	511	14.492	0.355
Cl	Cd	Cl/Cd			
0.03994	0.00529	7.55			
Altitude(ft)	36000	40000	50000	56000	60000
Noise(PLdB)	73.62	72.96	70.24	68.69	67.68
Cl required	0.032	0.040	0.078	0.118	0.15

Table 7: AoA=4°

Length(m)	Span(m)	Area(m^2)	Volume(m^3)	AR(subsonic)	AR(supersonic)
100	15.7	690	511	14.492	0.355
Cl	Cd	Cl/Cd			
0.07493	0.0089	8.419			
Altitude(ft)	36000	40000	50000	56000	60000
Noise(PLdB)	83.65	84.95	84.87	84.79	84.49
Cl required	0.0251	0.0319	0.0592	0.0863	0.1112

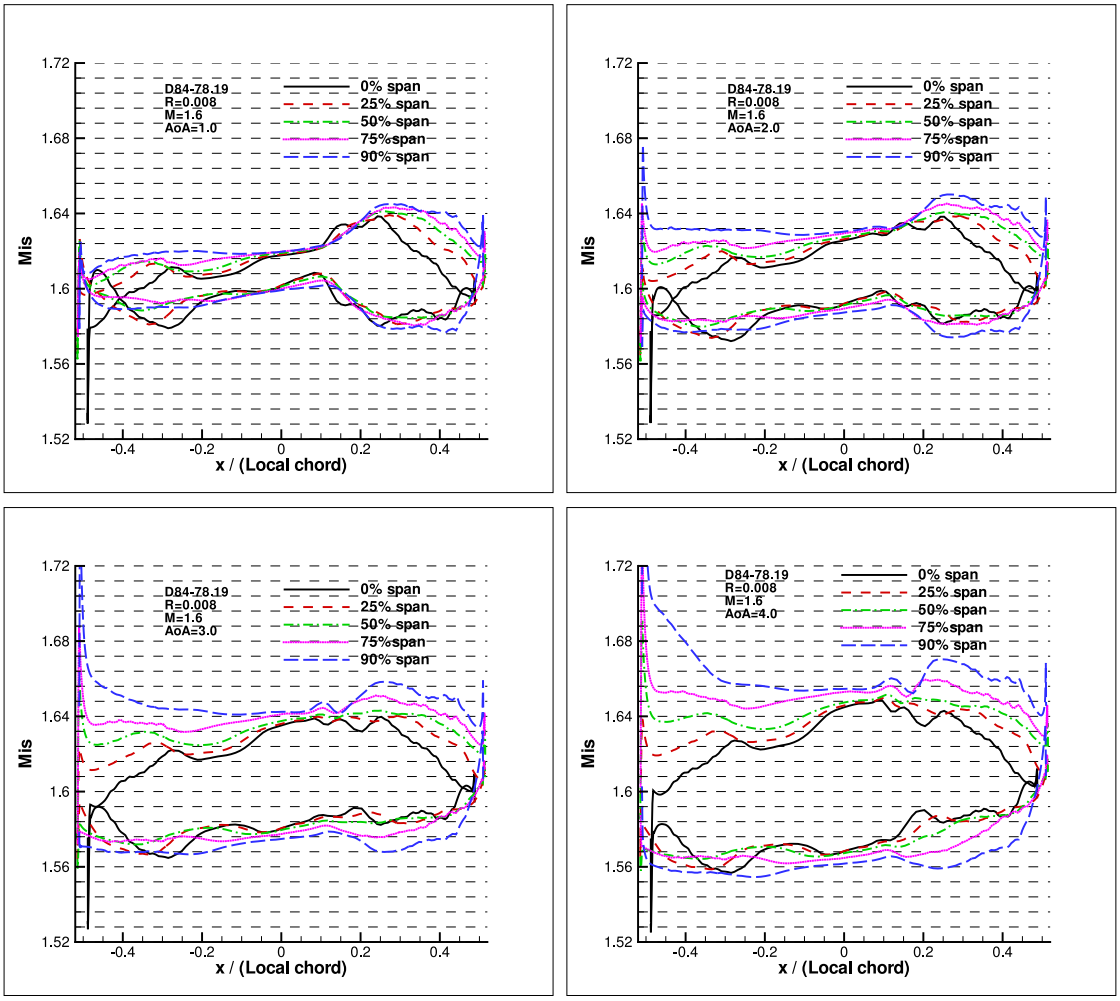

Figure 38: Surface isentropic Mach numbers at different spans for different AoA.

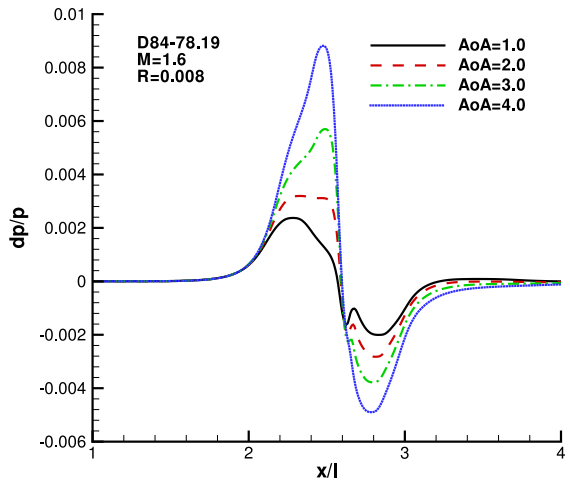

Figure 39: Over-pressure signature 2 body length below at different AoA.

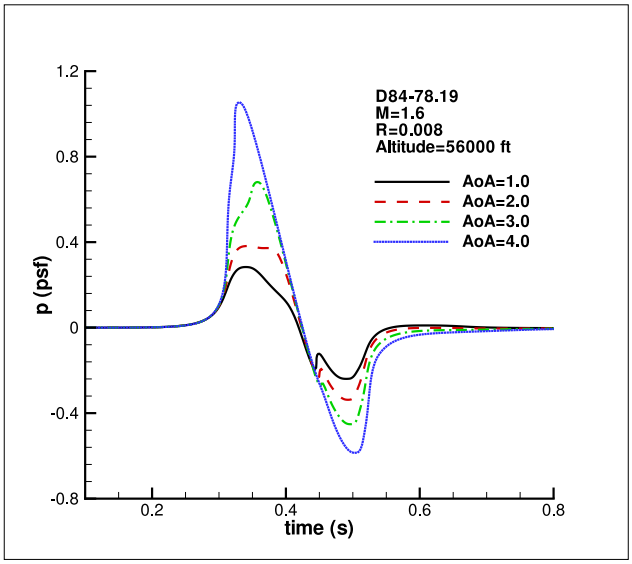

Figure 40: Ground boom signature at different AoA.

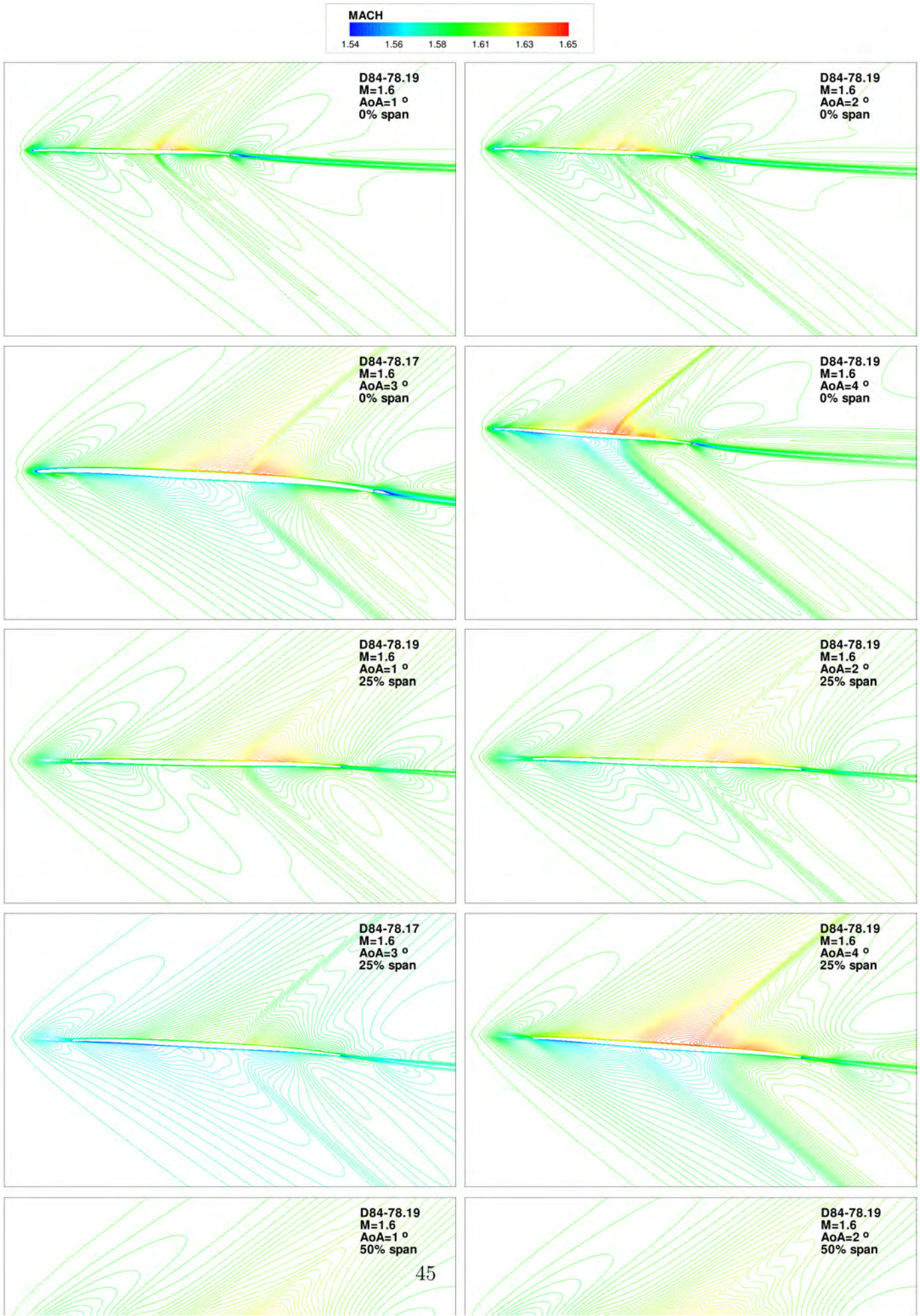
MACH
1.54
1.56
1.58
1.61
1.63
1.65
D84-78.19
M=1.6
AoA=1 º
0% span
D84-78.19
M=1.6
AoA=2 º
0% span
D84-78.17
M=1.6
AoA=3 º
0% span
D84-78.19
M=1.6
AoA=4 º
0% span
D84-78.19
M=1.6
AoA=1 º
25% span
D84-78.19
M=1.6
AoA=2 º
25% span
D84-78.17
M=1.6
AoA=3 º
25% span
D84-78.19
M=1.6
AoA=4 º
25% span
D84-78.19
M=1.6
AoA=1 º
50% span
D84-78.19
M=1.6
AoA=2 º
50% span

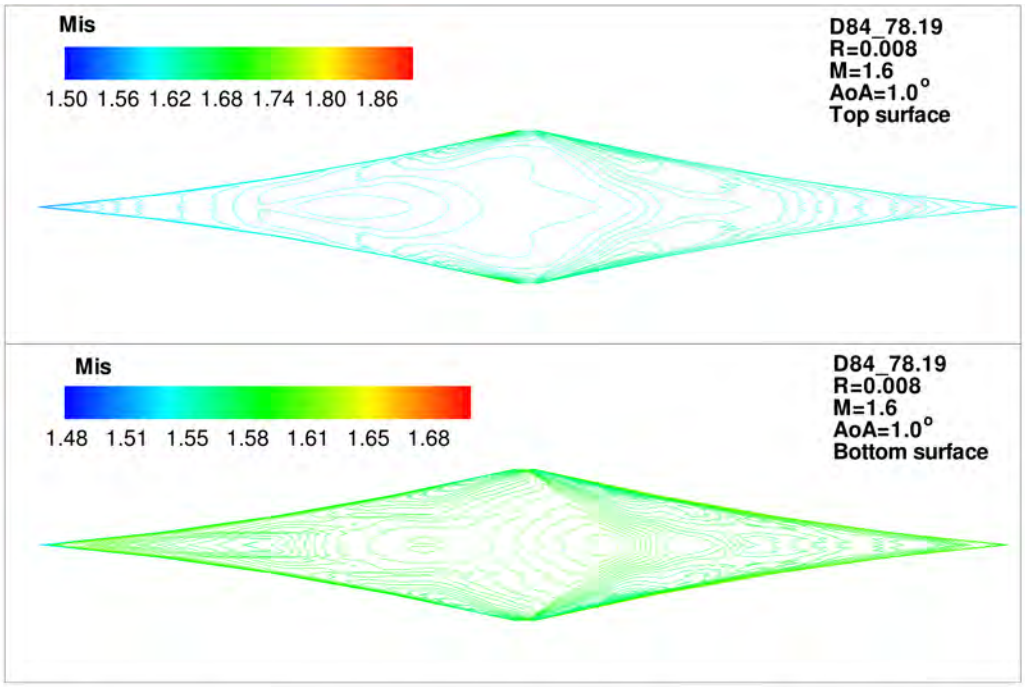

Figure 42: Mach number contours on suctions and pressure surface at AoA=1°

7.6 Leading/Trailing Edge Roundness Study

A sharp leading edge is generally preferred for supersonic airfoil to generate weak attached shock. However, sharp leading edge is difficult to handle variation of AoA. In particular for SBiDir-FW, it needs to fly at subsonic and a round LE is desirable. This trade study is to investigate what influence will a round LE has on sonic boom and aerodynamic performance.

The same design of D84-78.19 studied in section 7.4 and 7.5 is compared with different LE radius from completely sharp ($R_{LE} = 0$) to $d_{LE}/t_{max} = 0.36$ for all the airfoil. For a maximum thickness of 2.2% used in D84-78.19 at zero span, the $d_{LE}/chord$ is about 0.008.

The overall conclusion is that a round LE and TE up to $d_{LE}/t_{max} = 0.36$ has a small benefit for both sonic boom and aerodynamic performance as demonstrated in Table 8 and 9 with the L/D slightly increased and the sonic boom loudness slightly reduced by 1dbPL.

The more important advantages for using round LE and TE are the following:

1) For the same planform area of the design D84-78.19 , the round LE/TE with $d_{LE}/t_{max} = 0.36$ increases the volume significantly by 18%. This is very important to hold more fuel and payload. Increaseing so much volume without hurting the sonic boom and aerodynamic performance is definitely very desirable. The high sweep angle avoids the penalty that a round LE may create in supersonic flow since the Mach number normal to the LE is subsonc.

2)It significantly increases the AoA range that a SBiDir-FW can operate efficiently and effectively.

Fig. 43 compares the surface isentropic Mach number distributions between the configurations using sharp and round LE/TE with the exact same meanline angle distributions and all other geometry parameters. At zero span, the round LE gives near zero incidence whereas the sharp LE has a negative incidence even though the overall Mach number distribution is similar. The peak Mach number generated by the round LE is also slightly lower. The round LE advantage is more shown for the outer span near tip. The sharp LE generates very high incidence and the round LE accommodate the flow much better with positive incidence. The peak Mach number generated by the round LE is significantly lower than that of the sharp LE at 90% span.

Table 8: Sharp LE/TE edge

Length(m)	Span(m)	Area(m^2)	Volume(m^3)	AR(subsonic)	AR(supersonic)
100	15.7	690	462	14.492	0.355
Cl	Cd	Cl/Cd			
0.05772	0.00727	7.94			
Altitude(ft)	30000	40000	50000	56000	
Noise(PLdB)	73.67	71.24	68.95	67.57	
Cl required	0.0175	0.036	0.0665	0.15	

Table 9: Round LE and TE with $d_{LE}/t_{max} = 0.36$

Length(m)	Span(m)	Area(m^2)	Volume(m^3)	AR(subsonic)	AR(supersonic)
100	15.7	690	544	14.492	0.355
Cl	Cd	Cl/Cd			
0.05628	0.00671	8.3875			
Altitude(ft)	30000	40000	50000	56000	
Noise(PLdB)	73.63	71.96	67.99	66.41	
Cl required	0.0175	0.030	0.055	0.80	

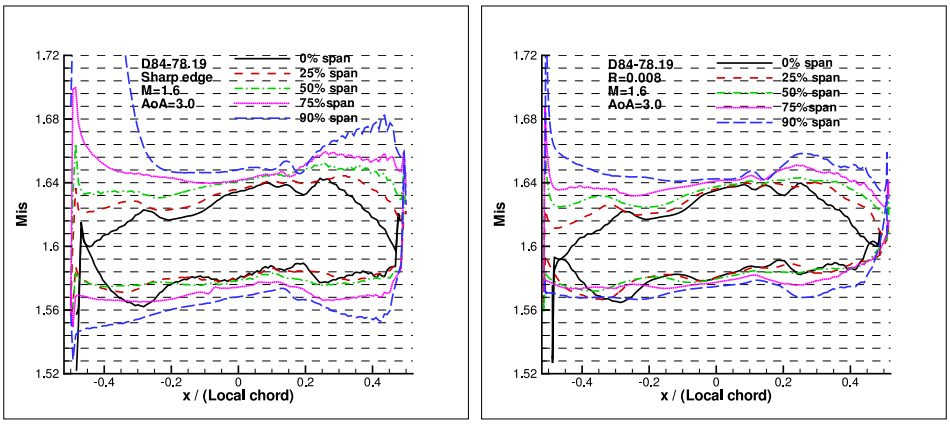

Figure 43: Wall Isentropic Mach numbers at different spans. Left: base design, Right: $d_{LE}/t_{max} = 0.36$

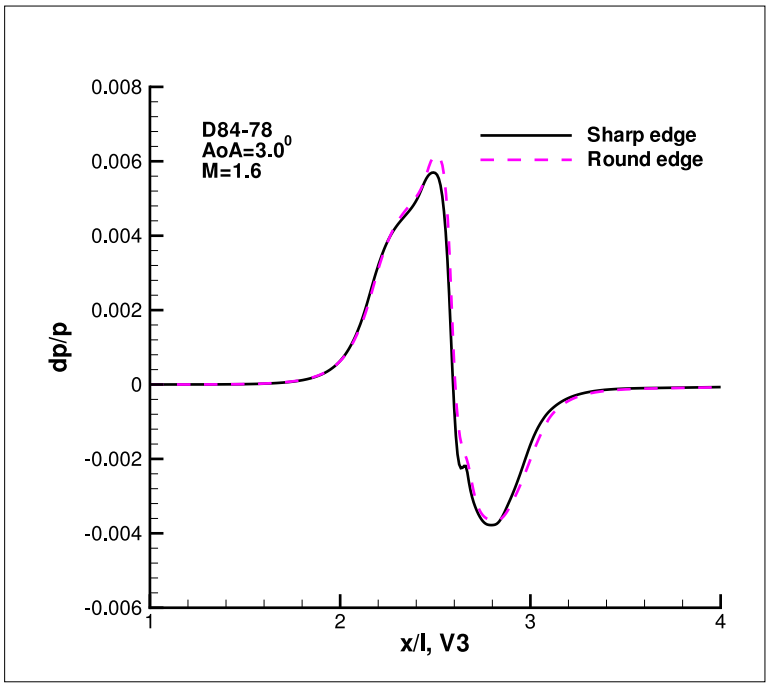

Figure 44: 2 body length below signal

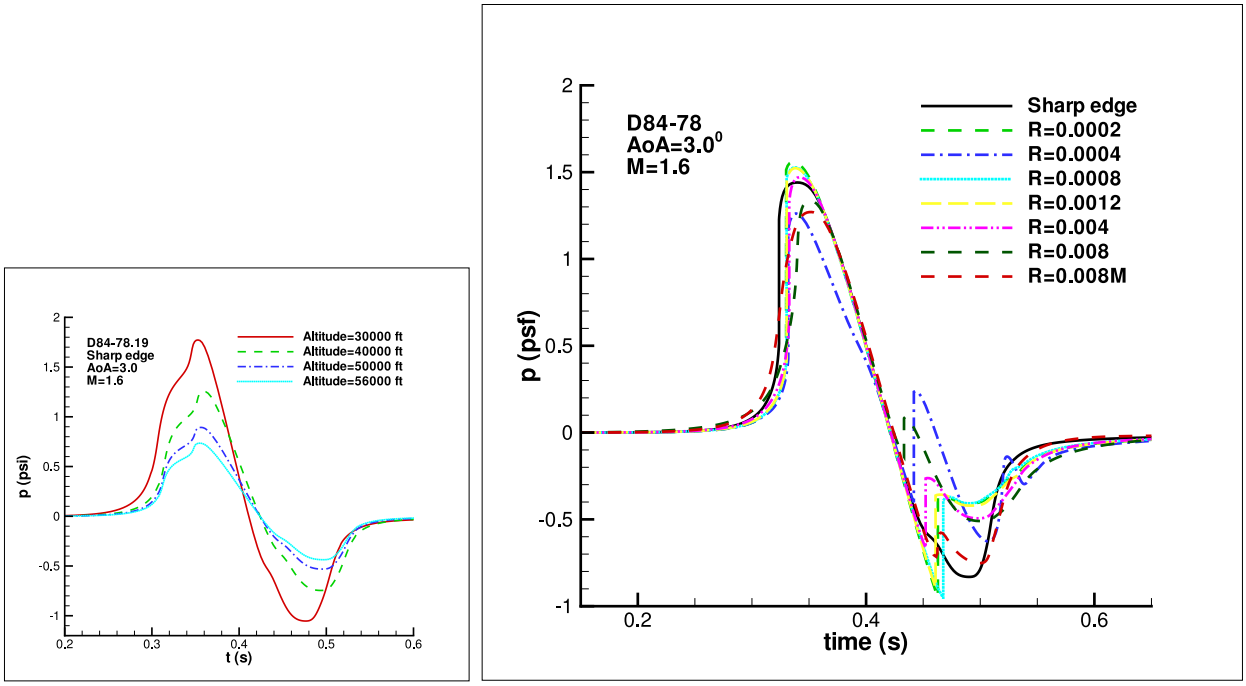

Figure 45: Ground boom(right)

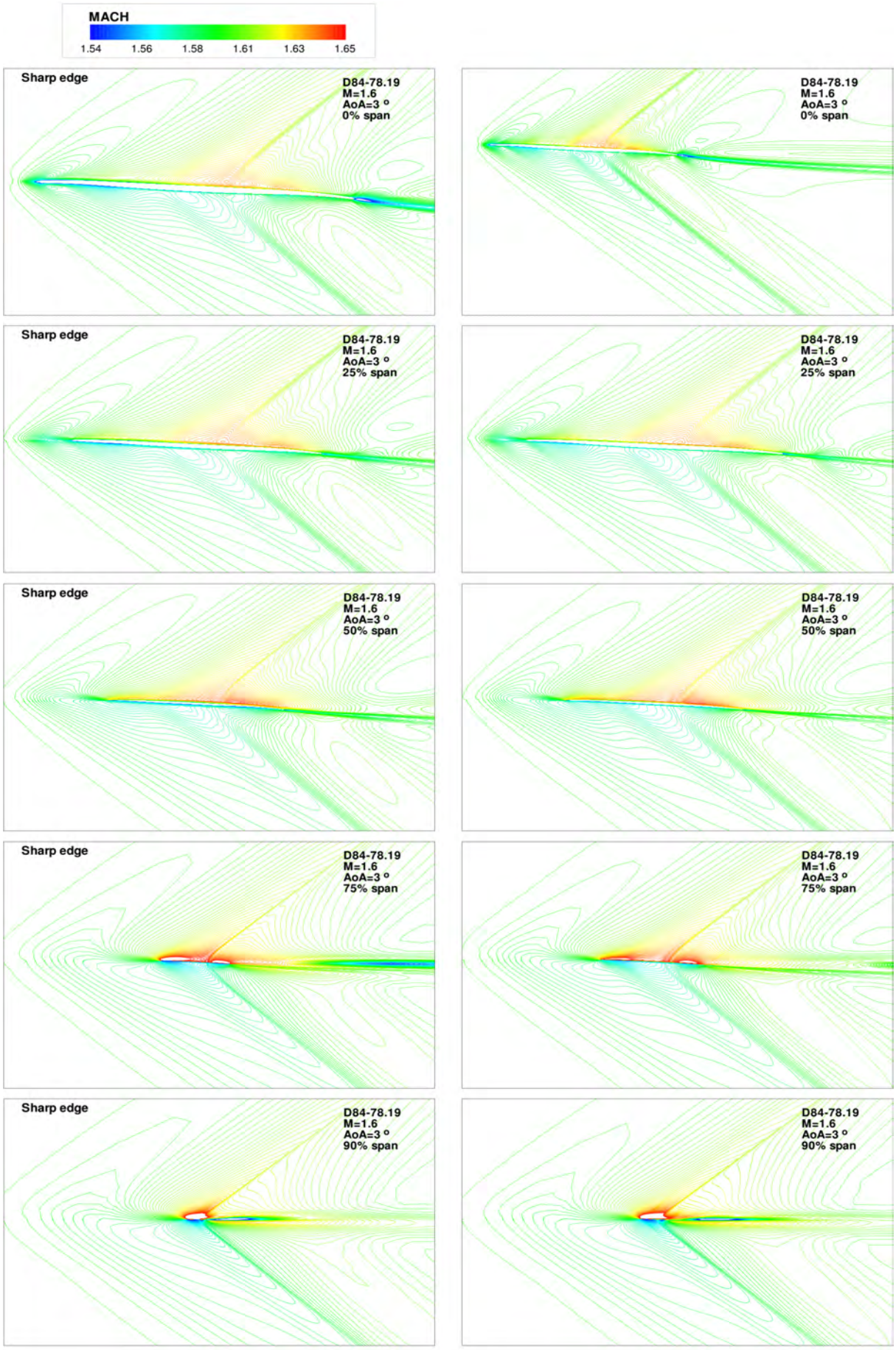

Figure 46: M at different spans

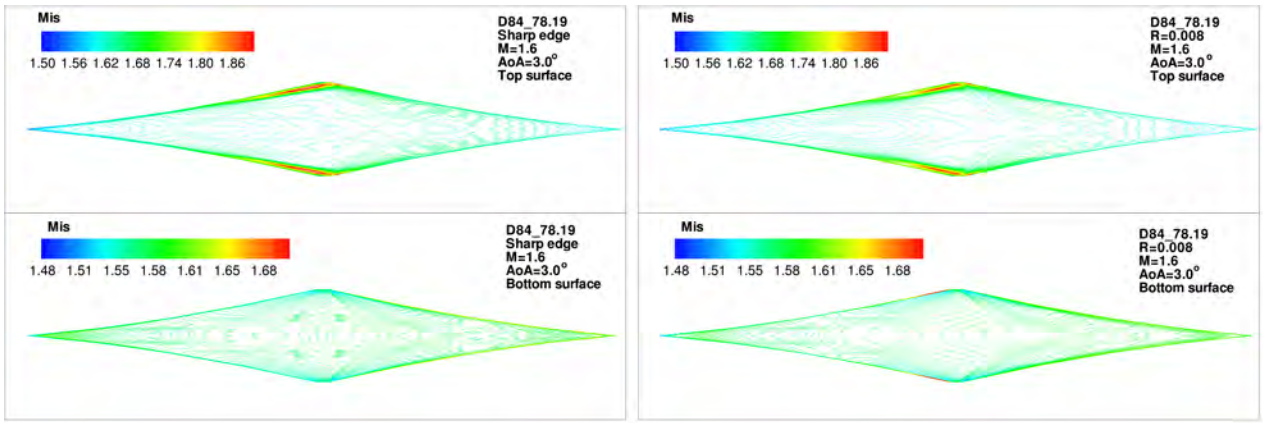

Figure 47: Surface Mis

7.7 Subsonic Performance

To demonstrate the advantage of subsonic performance of SBiDir-FW concept, the RANS simulation using S-A model is conducted for one of the designs. Since all the different design trade studies were conducted in parallel, this design with subsonic analysis is different from other designs presented in the previous section. The design is not optimized for supersonic, but a typical one with sharp LE and TE, which are found not the most favorable geometry for aerodynamic efficiency and sonic boom.

The design is named as D82-78-74-74nmC1S1. The Mach number selected for subsonic analysis is 0.25, representing the takeoff/landing situation. The Reynolds number is 4.3×10^7 based on the subsonic averaged chord length. The sweep angle is distributed from 82° to 74°. The geometry used one of the early option with point sharp LE and TE, which is not expected to sustain high AoA without flow separation. Round LE and TE will be used for future design. Table 10 shows some geometry information. The aspect ratios at supersonic is 0.44 and 10 at subsonic. Fig. 48 is the airfoil meanline angle distributions and airfoil shapes for D82-78-74-74nmC1S1. Fig. 49 is the overview of the D82-78-74-74nmC1S1 3D configuration.

7.7.1 Mesh

Both the supersonic CFD analysis and subsonic analysis are conducted for this design. The supersonic simulation used the same approach as mentioned before. Only the subsonic approach will be described below. The mesh calculation for the Navier-Stakes calculation at M=0.25 is constructed using the H-mesh topology as well. The mesh displayed Fig. 50 uses a total of 120 points around the airfoil, 60 along the span and 80 points in the direction normal to the airfoil. Total mesh size is 2.2 million cells, partitioned into 120 blocks for the parallel computation. The first grid point is placed at $y^+ \approx 1$.

For both supersonic Euler and subsonic RANS calculation, refined grids are constructed using 50% more points in every direction. The baseline mesh and refined mesh results showed excellent agreement for the Euler calculation and reasonably good agreement for the Navier-Stokes calculation.

7.7.2 Aerodynamic Performance

Fig. 51 shows the forces and pitching moment of the passenger at supersonic M=1.6. The mesh refinement performed for the passenger plane is in perfect agreement with the original mesh results. The lift and pitching moment vary almost linearly with the AoA. The D82-78-74-74nmC1S1 design used for the passenger plane reaches $L/D = 9.2$ at AoA=3°. However to reduce sonic boom, the AoA=2.5° and $L/D = 8.92$ is used for cruise. The pitching moment calculation has the pressure forces only since the inviscid Euler is used. The moment calculation is performed around the center of gravity, which coincides with the geometric center of the aircraft. The near zero values of the pitching moment makes the aircraft easy to trim.

Design	Sweep angle (°)	Length(m)	Span(m)	Area(m^2)	AR sub	AR sup
D82-78-74-74nmC1S1	$[82°, 78°, 74°, 74°]$	100	21.1	1002	10.0	0.44

Table 10: Geometric overview of the D82-78-74-74nmC1S1 passenger aircraft.

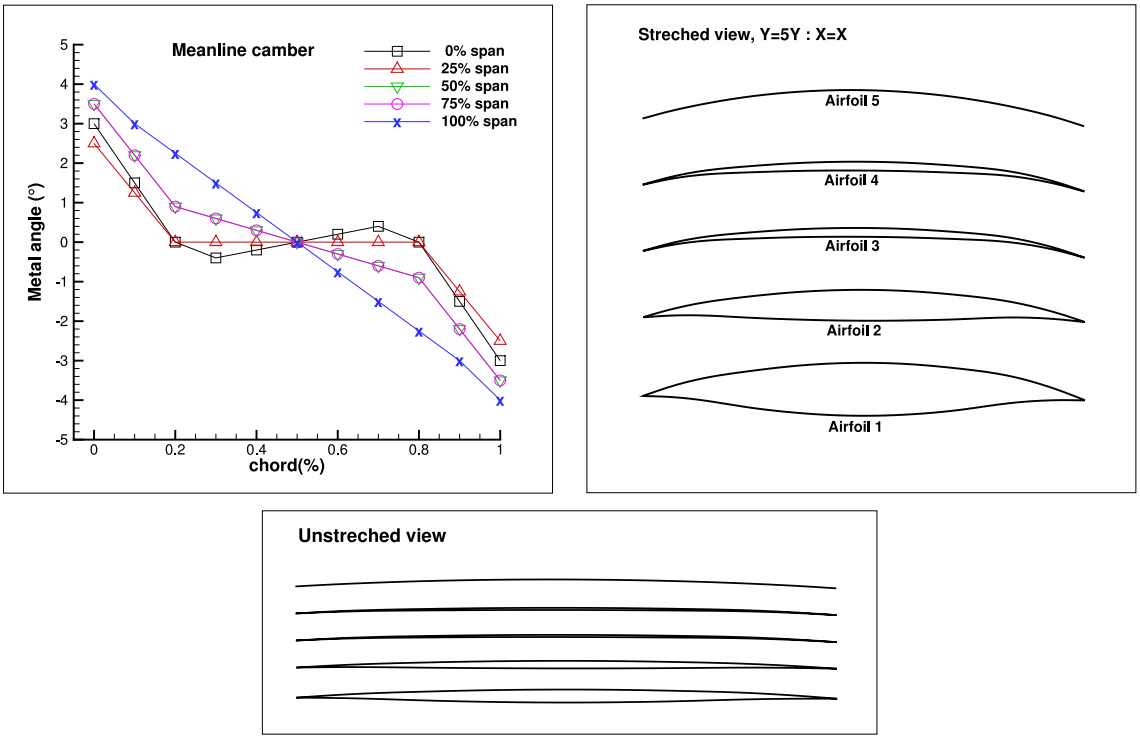

Figure 48: Passenger airfoils camber and profile plots. The top left plot shows the camber distribution of each airfoil. The top right plot shows the airfoil geometry, the view is stretched 5 times in the Y direction. Bottom plot shows the airfoil geometry without stretched view.

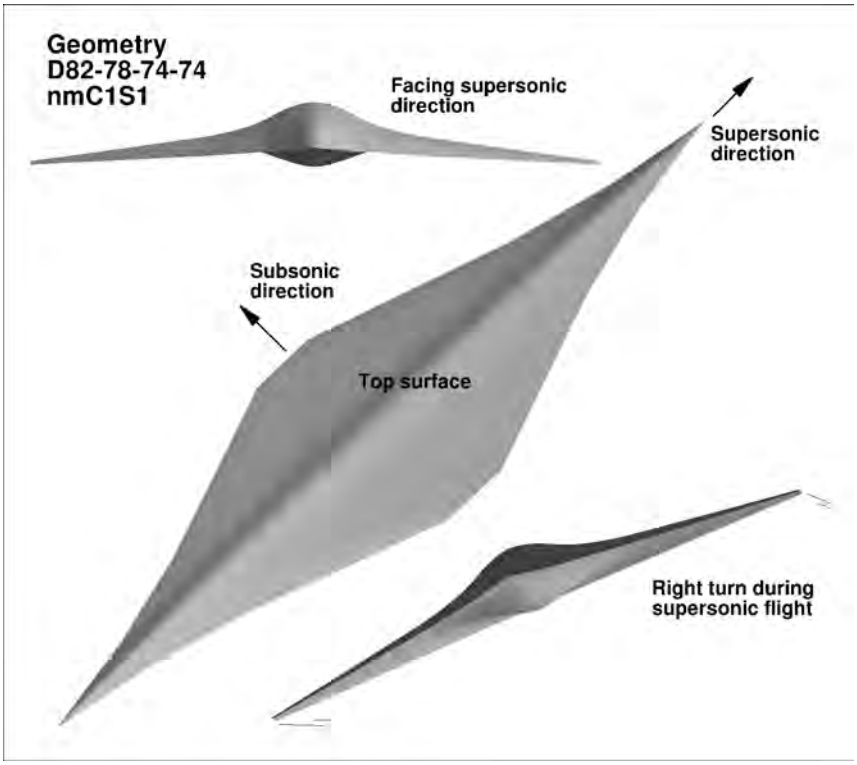

Figure 49: D82-78-74-74nmC1S1 Passenger plane geometry overview.

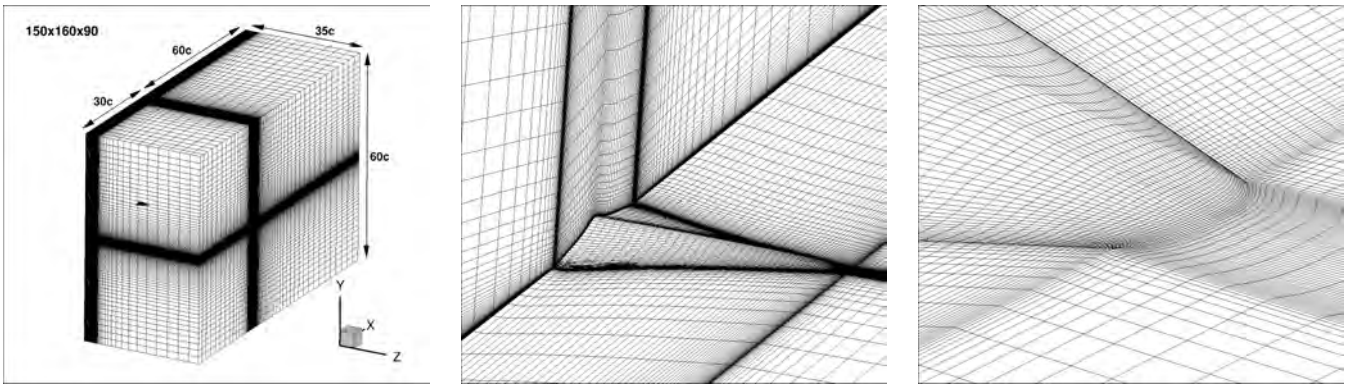

Figure 50: Subsonic mesh topology of the Navier-Stokes calculation at M=0.25. Outer mesh (left), suction surface (middle) and wing tip (right).

Fig. 52 shows the forces and pitching moment at subsonic M=0.25 for D82-78-74-74nmC1S1(labeled as the passenger). The friction drag also benefits from the relatively thick, almost separated boundary layer. The mesh refinement performed is in perfect agreement for the lift and moment and a fair agreement for the drag, which is over-predicted by the original mesh by 10%. The subsonic D82-78-74-74nmC1S1 reaches $L/D = 19.7$ at AoA=2°. The moment is slightly greater than zero at AoA=2°. This allow to control of the aircraft without trim.

7.7.3 Angle of Attack Effect at M=1.6

Fig. 53 shows the aerodynamic performance and sonic boom with AoA varying from 1-3°. The top plot is the isentropic Mach number at different span location, the middle plot is the over-pressure at 2-body length below, and the plot at the bottom is the ground sonic boom signature.

Mach number distribution, top of Fig. 53
The increase of AoA results in an increase the incidence, which leads to a wider opening of the Mach number surface distribution at LE. In addition, the tip up-wash further increase the incidence in that region. The wing tip loading does not seem to affect the boom which depends mostly of the center profile loading. The Mach number variation on the pressure surface is relatively smooth for all AoA.

Over-Pressure, middle and bottom of Fig. 53
The 2-body below over-pressure amplitude increases with AOA increasing. The low 2 BL over-pressure at $AoA = 1°$ combine with the relatively low flight altitude prevent the pressure wave from converging into a N-wave as seen on the ground boom plot. This results in a relatively smooth signature with low perceived loudness. At $AoA = 2.0°$ both the 2 body length pressure signal and the ground pressure signal are smooth with low amplitude. The calculated ground perceived sound level using *NF Boom* is 79.8dBPL. At $AoA = 3°$ more lift is generated with stronger pressure waves. The 2 body length bellow pressure signal is smooth but the amplitude is large. When propagating to the ground, the pressure waves converge into a N-wave that generates high perceived loudness.

Fig. 54 shows the Mach number contours on SBiDir pressure and suction surfaces as well as the planform shape used. No strong waves appears until AoA=3°. Fig. 55 shows spanwise cross-section views of Mach number contours. All AoA experience very similar physics with stronger waves as the AoA increase. The central airfoil experience a relatively fast expansion-compression on the suction surface. The flow experience an isentropic compression on the 1^{st} 60% chord of the pressure surface. Past 60% chord, expansion waves takes place. Eventually the flow field recompress at the TE of the airfoil. At 50% span waves are very smooth. The 90% span is the most loaded part of the wing, however there is little propagation of the waves toward the ground.

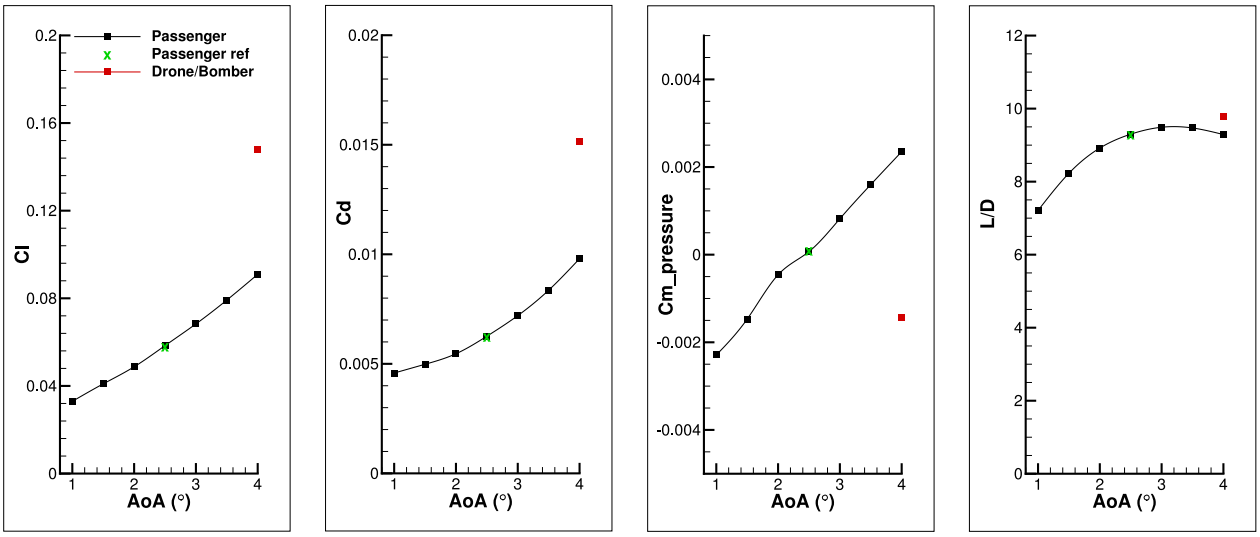

Figure 51: Forces and pitching moment at various AoA and M=1.6 for D82-78-74-74nmC1S1.

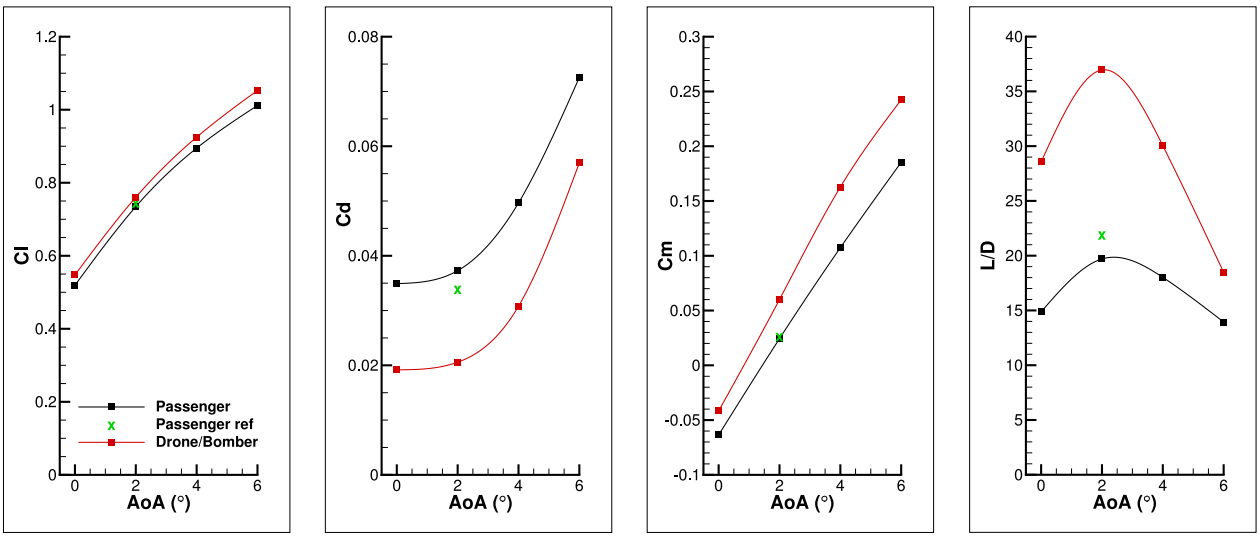

Figure 52: Forces and moment at various AoA and M=0.25 for the D82-78-74-74nmC1S1 passenger plane .

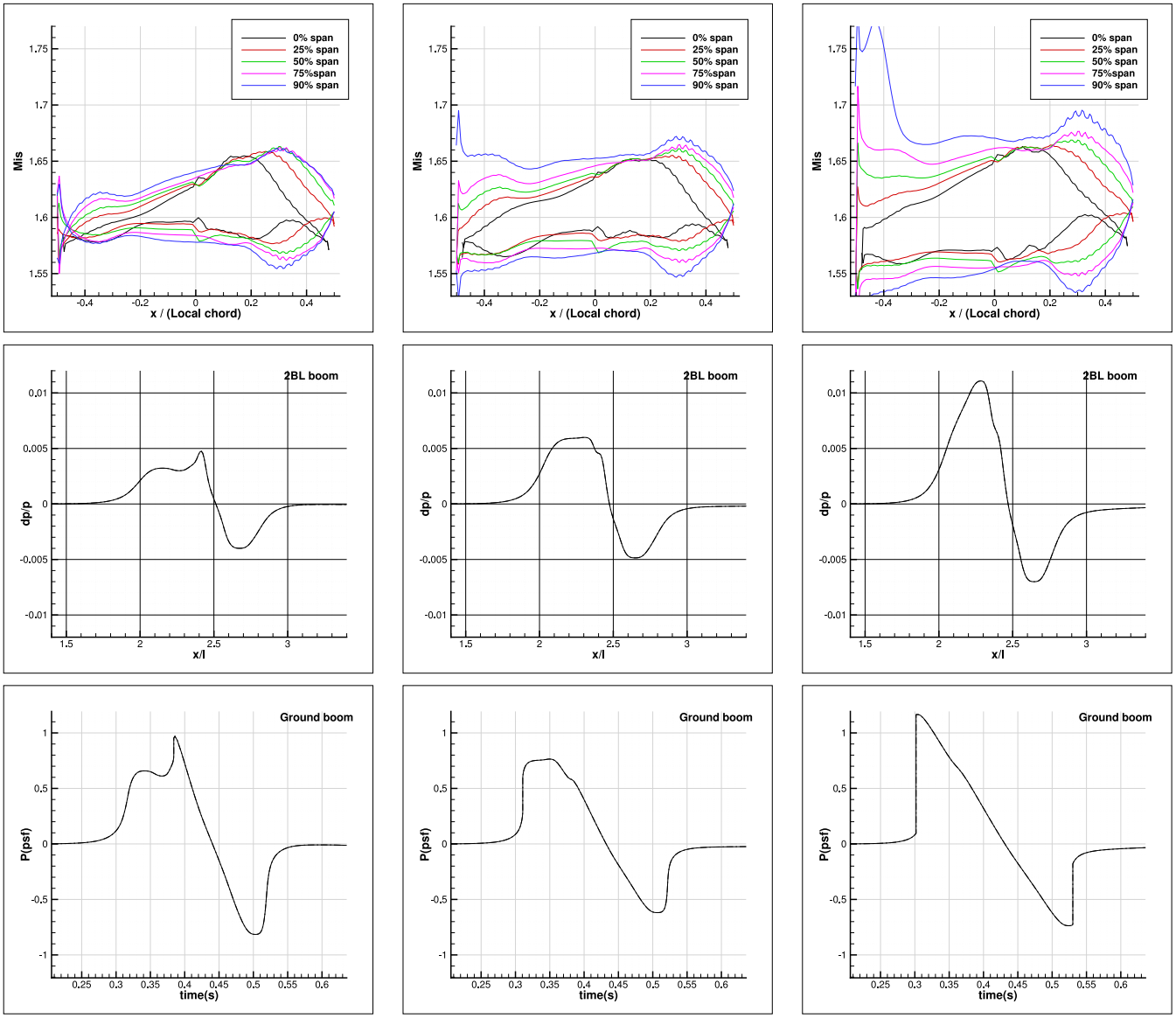

Figure 53: Effect of AoA on the passenger plane at M=1.6. From top to bottom are displayed the Mis at various spanwise locations (top), the 2 BL bellow pressure field (middle) and the ground boom (bot). The AoA varies from left to right with AoA=1° (left), AoA=2° (middle) and AoA=3° (right).

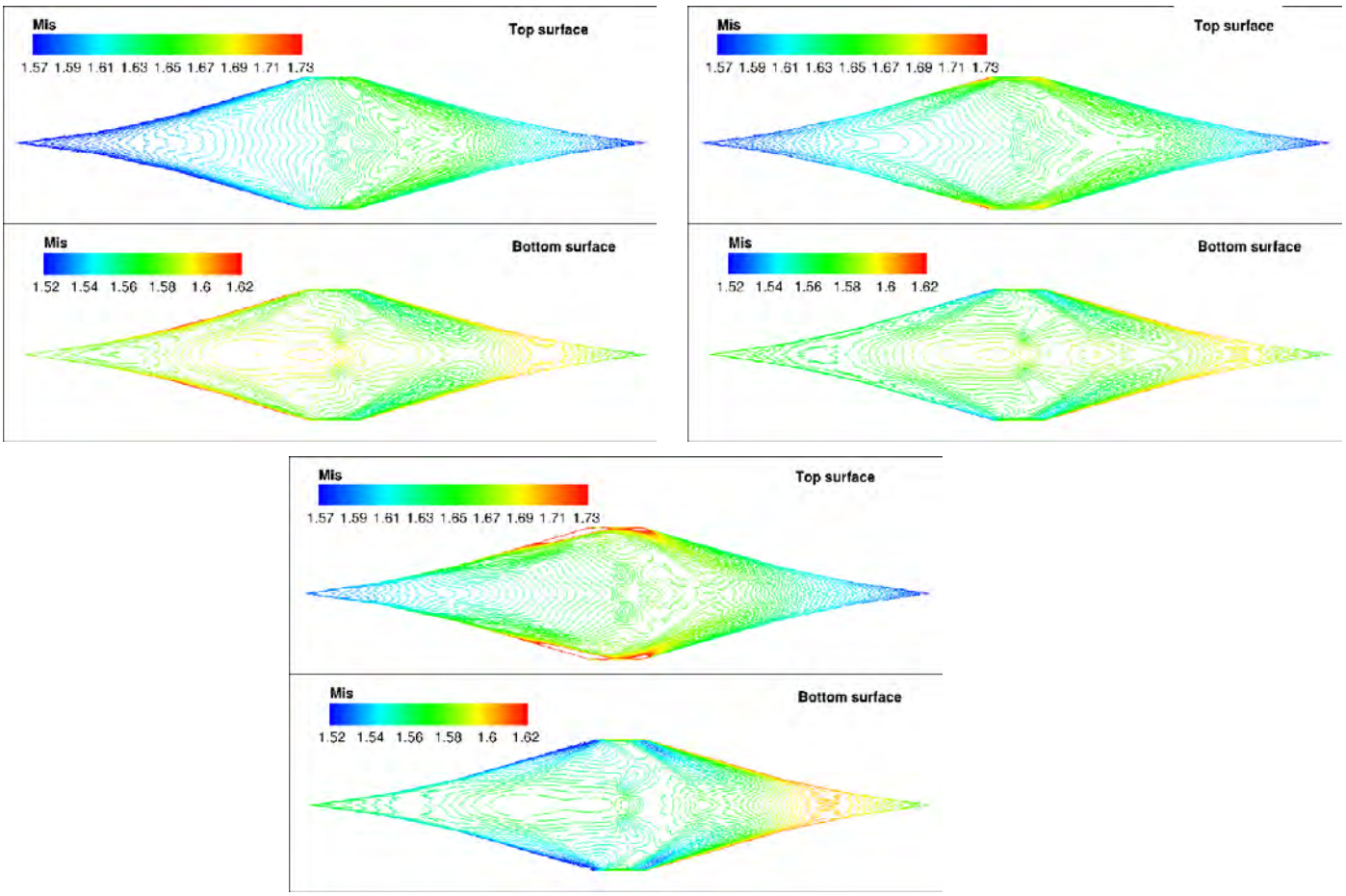

Figure 54: Effect of AoA on the passenger plane at M=1.6. Comparison of Mis on the pressure and suction surface with AoA=1° (top left), AoA=2° (top right) and AoA=3° (bot).

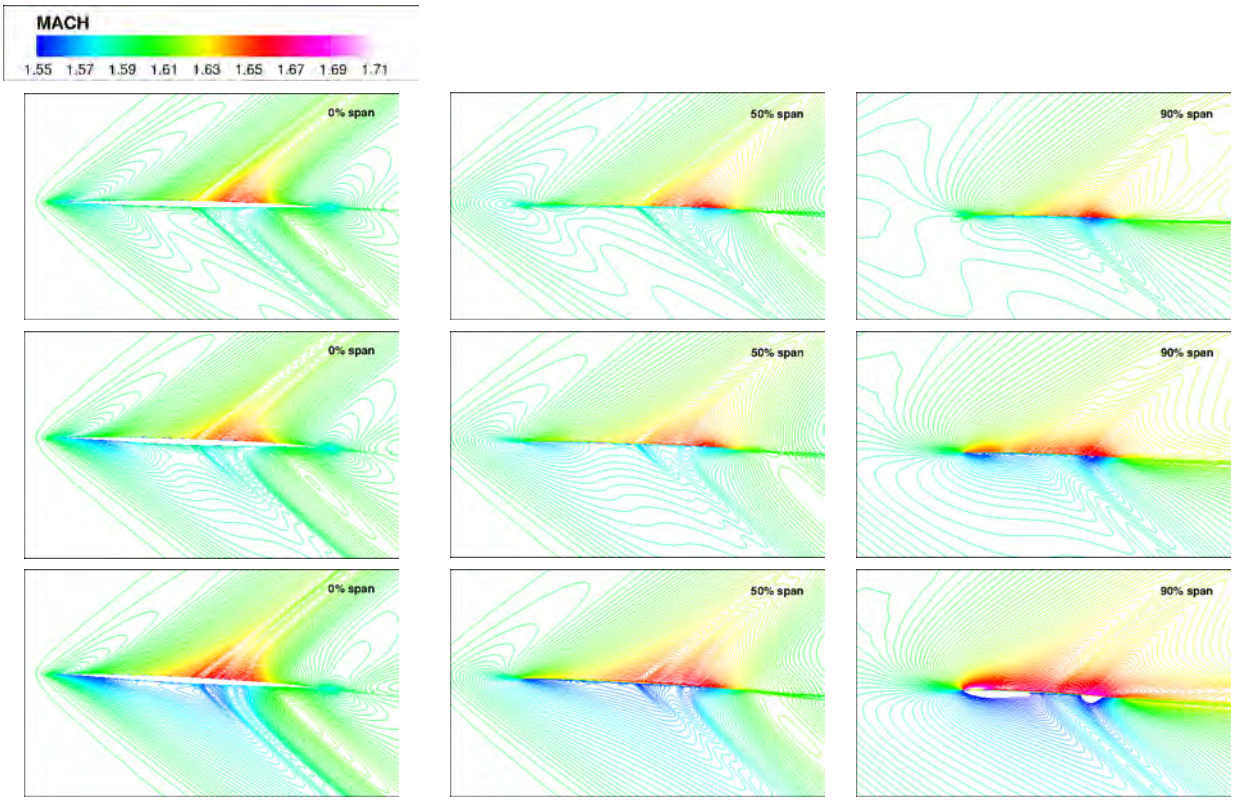

Figure 55: Effect of AoA on passenger plane at M=1.6. Comparison of spanwise cross-section views of Mis line contours for AoA=1° (top), AoA=2° (middle) and AoA=3° (bot).

7.7.4 Performance At M=0.25

The Mach number of 0.25 reflects the conditions at take-off, landing and loitering. Fig. 56,57 show the Mach contours at various spanwise locations at AoA=2° and AoA=6° at M=0.25. At AoA=2°, the 0% and 33% span flow is attached. At 66% and 90% span, the flow has a small separation at the TE. This separation forms a vortex tube that developes in spanwise direction from the tip to the center of the aircraft. As shown in Fig. 52, the L/D=19.7 is achieved at AoA=2°, which is the primary subsonic flight AoA. At AoA=6°, the TE separation is stronger and propagates up to 33% span. The flow also separate at the LE of the aircraft at 0% and 33% span because of the sharp LE, which is not favorable for subsonic flow and will be replaced by the round LE and TE in our design.

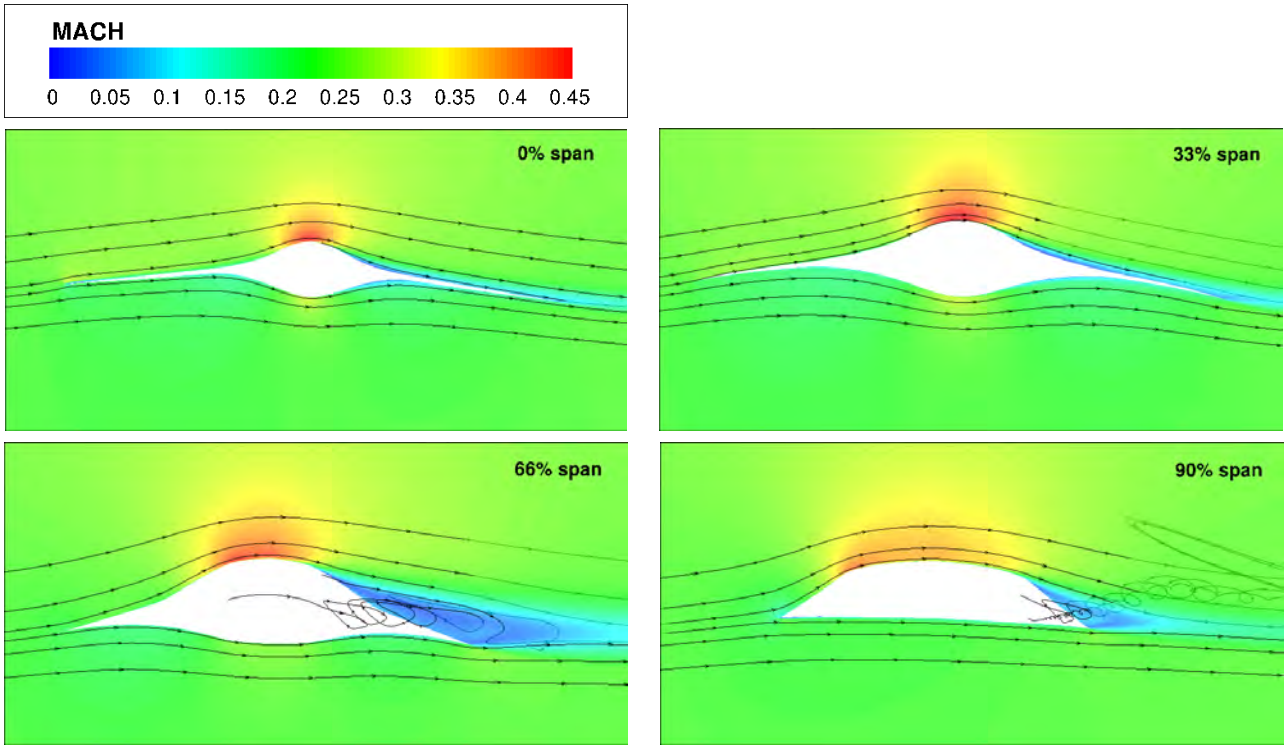

Figure 56: Spanwise Mach contours of the passenger plane at M=0.25 and AoA=2°.

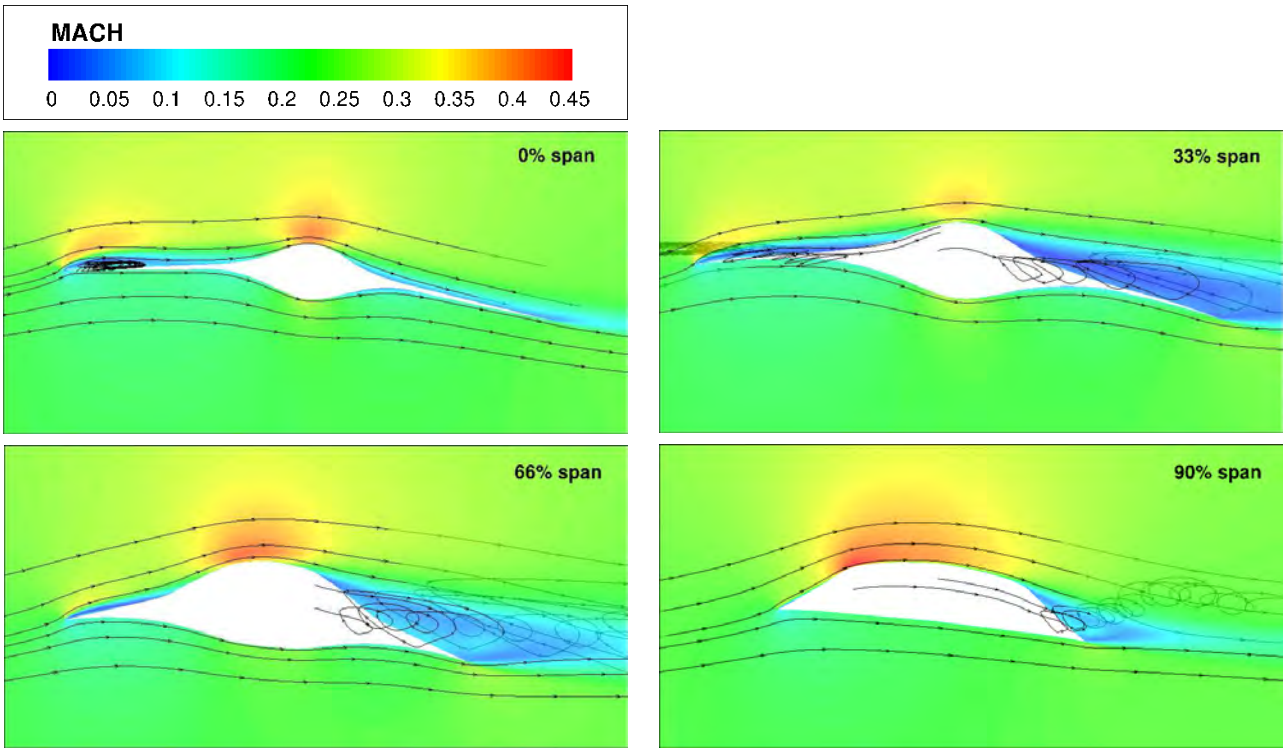

Figure 57: Spanwise Mach contours of the passenger plane at M=0.25 and AoA=6°.

7.8 Internal Seating

To demonstrate that the SBiDir-FW designed has sufficient volume, internal seating and external attachment of engines and landing gears are designed for two configurations with moderate aerodynamic performance. The two designs are named D84TW and D82S4. Both are diamond shape planform with sweep angle of 84° and 82° respectively.

Both the design have the length of 100m and thickness of 2.2% in the 0 span location and the thickness is decreased to 0.5% toward to the tip. D84TW has an excellent ground boom signature of 64dbPL due to its very high sweep angle of 84°. But the lift is also small and the overall L/D is only 5.5, which is not sufficient to fly 4000nm.

Table 11: Minimum interior dimensions for aircraft seating based on flight duration

Minimum	Long Range	Short Range
Seat Width	17in	16 in
Pitch	34	30
Headroom	65 in	60 in
Aisle width	20 in	15 in

Based on design parameters for seating shown in Table 11[3], a volumetric analysis of the plane was needed to determine the available room for passengers. SolidWorks was used to examine all designs' interior volume. Design D84TW is analyzed for minimum long range passenger aircraft requirements, and seated only 72 passengers. Taking a cut out of all the plane's area for which the height was greater than 60 inches as the minimum headroom requirement, an oval-shaped region in the middle of the flying wing was extracted from the original solid model, and a shell was created of this area in order to mimic the possible aircraft cabin. The minimum aircraft wall thickness is 7cm. Screenshots of the cabin area for Diamond 84 Thin Wing can be found in Figure 55. The chairs have minimum width of 16 inches and minimum pitch of 30 inches, and arranged in the cabin shell for maximum passengers. Aisle width was kept at 20 inches, and placed around the outside of the cabin for maximum seating room. Bathroom and cockpit spacing was considered as well for correctness. Diamond 84 Thin Wing's final assembly seats 58 people plus two pilots and also has two bathrooms. Screenshots of this assembly can be seen in Fig. 58 and 59.

The same process was followed in SolidWorks to create the cabin shell for Diamond 82 S4. The cabin area and shell can be seen in Figures 5 and 6 below. This new configuration adequately met the mission requirement of 100 passengers, and contained 3 bathrooms and a cockpit for two pilots. The cockpit and seating arrangement can be seen in Fig. 60 and 61. Since the minimum short range requirements for D82S4 allowed enough space for more passengers than the mission requirements (although only 100 seats were placed), in future designs the next step in optimization will be to increase the seat width, pitch, and headroom, and the aisle width and height until the maximum of each is reached to still allow 100 passengers.

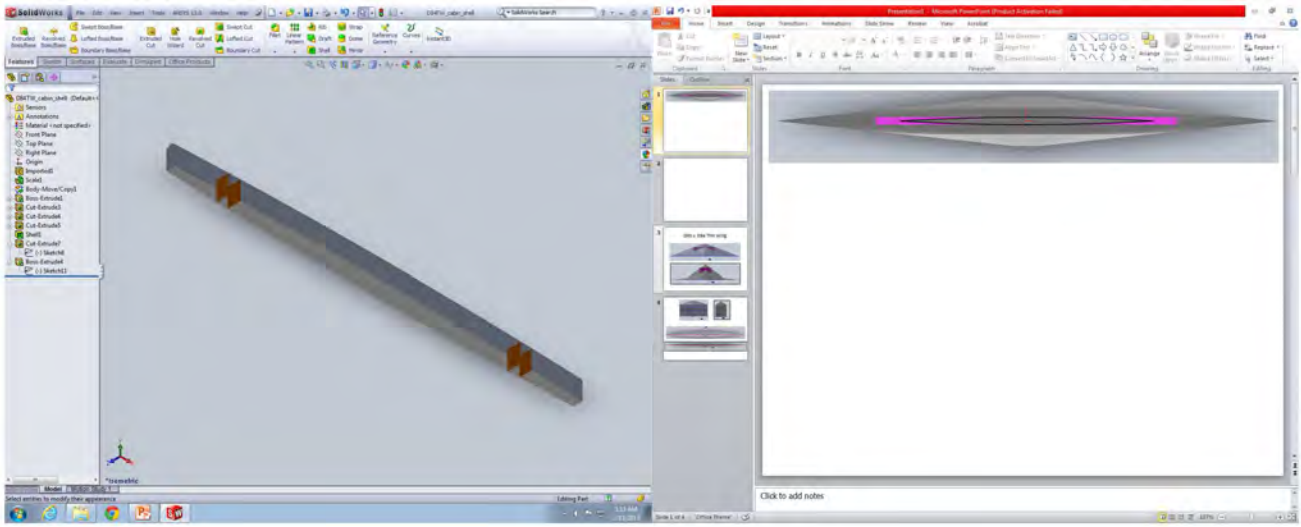

Figure 58: Cabin Shell of D84-TW. The top image shows the cabin area outlined in black in comparison to SBiDir.

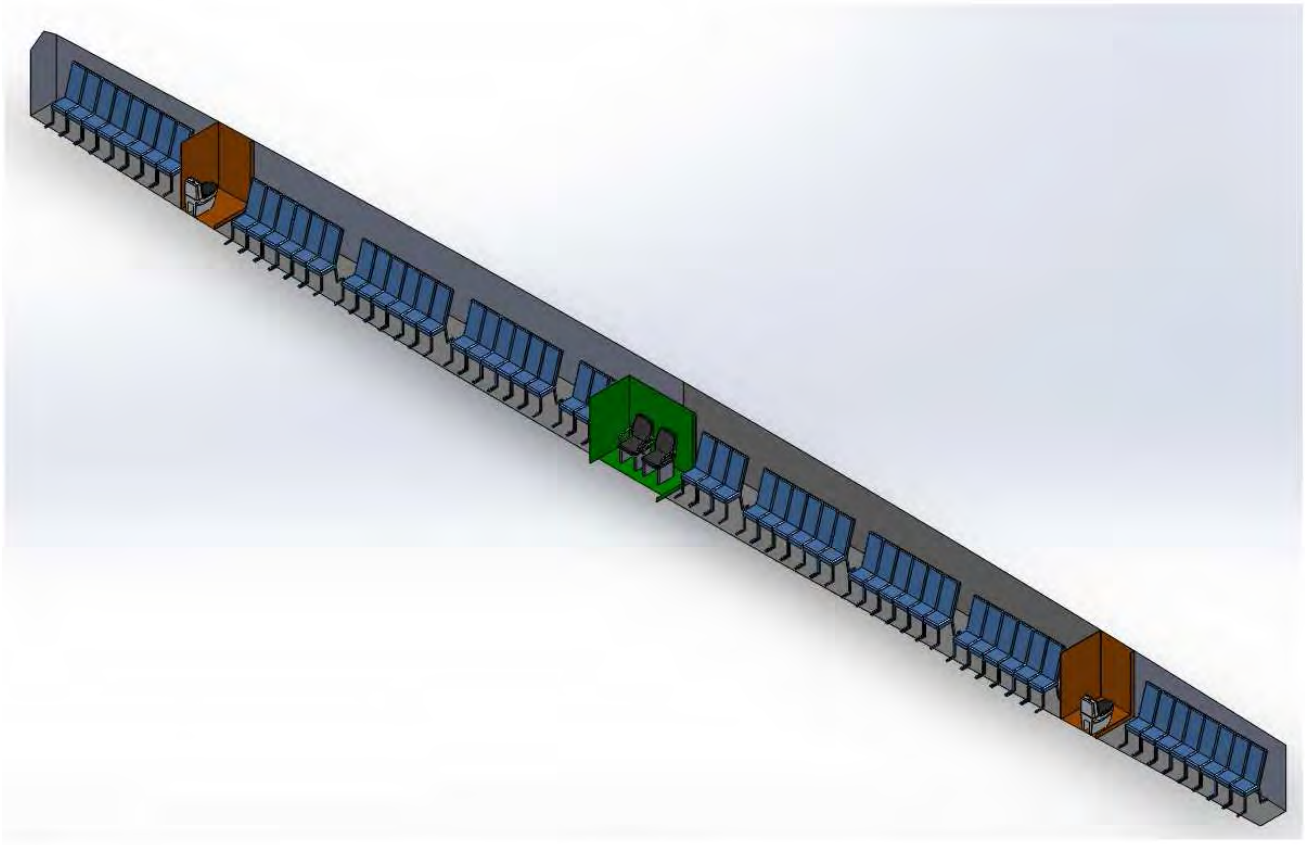

Figure 59: Cabin assembly of D84-TW. Orange rooms indicate lavatories, green room is the cockpit.

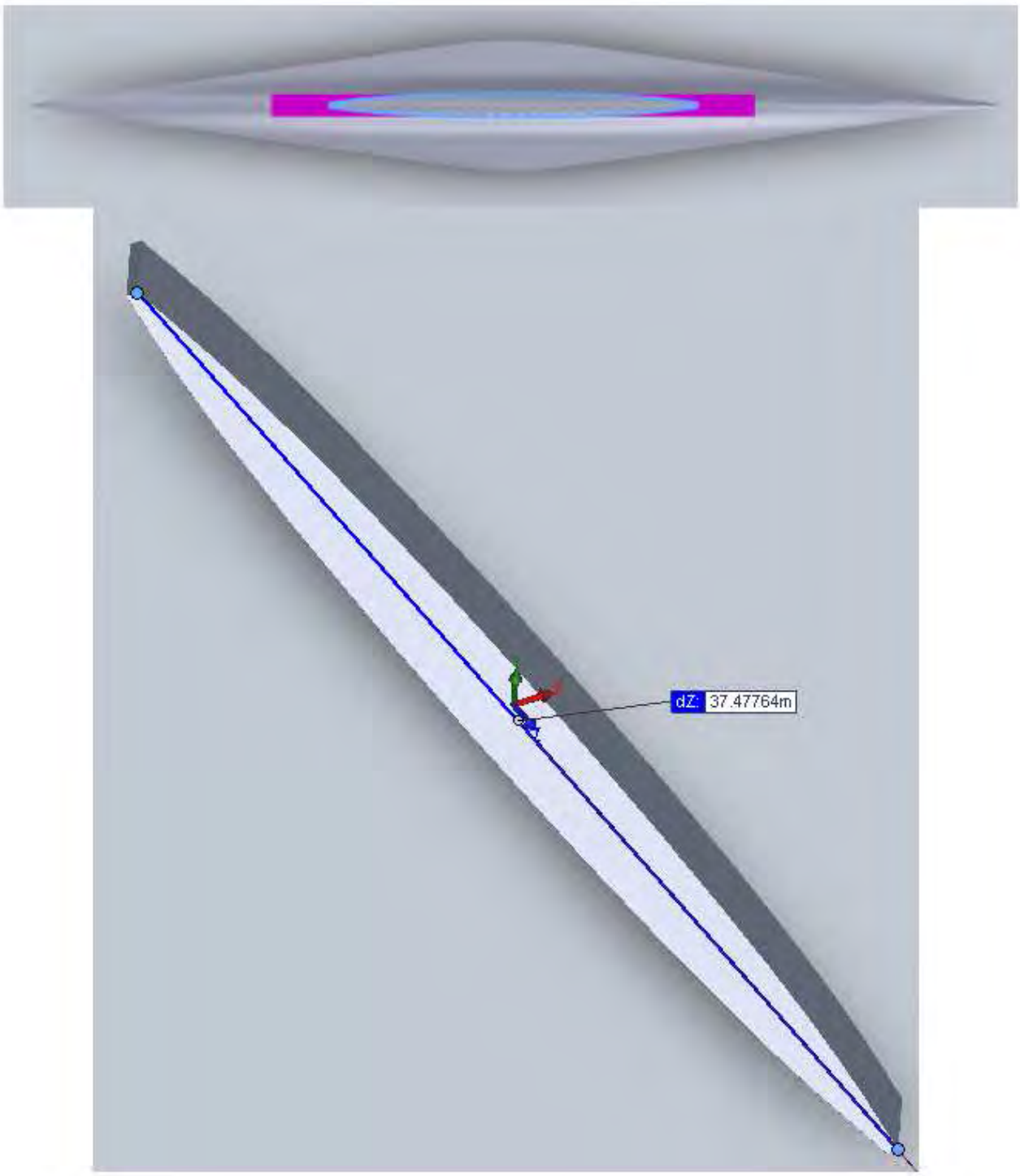

Figure 60: Cabin Shell of D82-S4. The top image shows the cabin area outlined in light blue in comparison to SBiDir

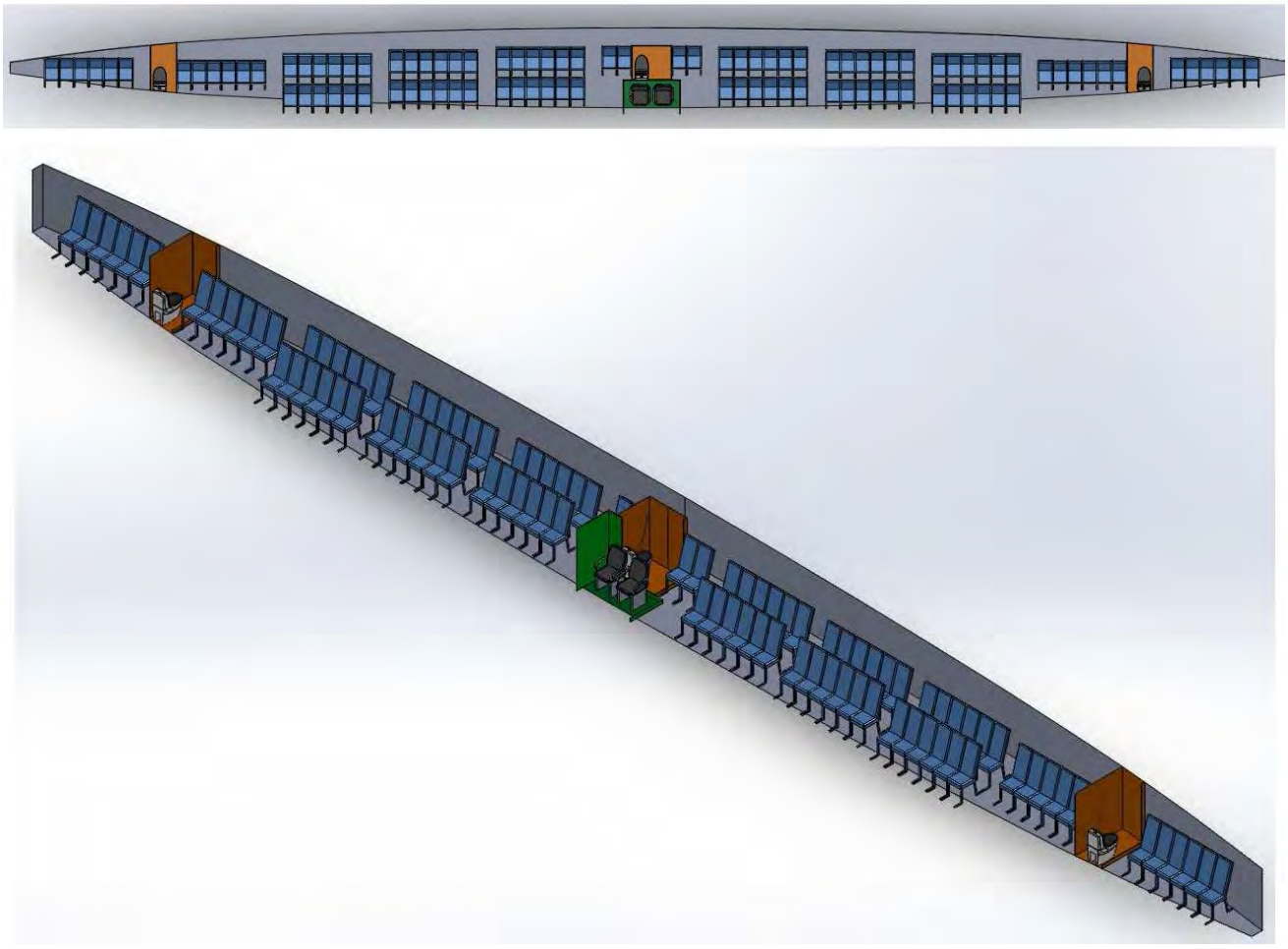

Figure 61: Cabin assembly of D82-S4. Orange rooms indicate lavatories, green room is the cockpit.

7.9 Engine Mounting

A turbo-jet engine with low captured area will be used on SBiDir to meet the requirements of flight conditions and safety. D84-TW requires a maximum thrust of 44 klb from two engines at sea level and D82S4 requires maximum thrust of 64 klb, which includes the case of emergency with power from one engine. Currently, no such an engine exists matching the required thrust. A projected engine is sized based on the NASA N+2 engine studied by Boeing[26]. SBiDir-FW will have its engines mounted above the wing. The wing area at that region is constantly changing and does not provide an easy mounting surface. Additionally, for symmetry the engines will be mounted near the center of the wing body where the passengers are located. The substantial weight of the engine will require very strong mounts. It will be necessary to heavily reinforce the structure in this area for sufficient safety.

Traditionally, engines have been mounted below the wing or have been blended into the body of the aircraft. In the case of SBiDir, under-mounted engines are not favorable due to the presence of wave propagation especially to the ground. Additionally, it also creates a much larger clearance for landing gear, which would add to the overall weight of the aircraft. Blending the engines into the body is also not feasible due to the necessary turning of the aircraft during flight. The rotation also presents troubles in a twin-engine design in symmetry of the thrust outputted from the engines.

Therefore, the engines will be mounted above the wing using a Y strut attachment. The Y strut shape allows the engines to maintain its symmetry even during rotation from subsonic to supersonic and vice-versa. Additionally, the shape also provides for a singular turning axis, which is beneficial in maintaining symmetry during rotation. The mounting strut also provides the necessary height above the structure. The height will prevent the engines from disrupting the passengers within the cabin with engine noise. The engine and its mount will be located just aft of the mid-plane in the supersonic direction. Having the engines there reduces the possibility of a large nose down moment if any instability during flight occurs. Additionally, the location is near the mid-plane in the subsonic direction as well keeping a symmetric application of thrust in both directions possible. Any further beyond the mid-plane will disrupt a steady flow into the engine inlet due to the shockwave. The engines can be seen in Fig. 62 and 63 in the supersonic direction.

For the subsonic direction the strut and engines will be mounted directly on the mid-plane in the subsonic direction. This provides for a symmetric application of the thrust and increased stability during flight. The engine attached to the Y strut can be seen in Fig. 64 for subsonic flight direction.

Figure 62: Engines attached to D82S4 in supersonic direction, top view

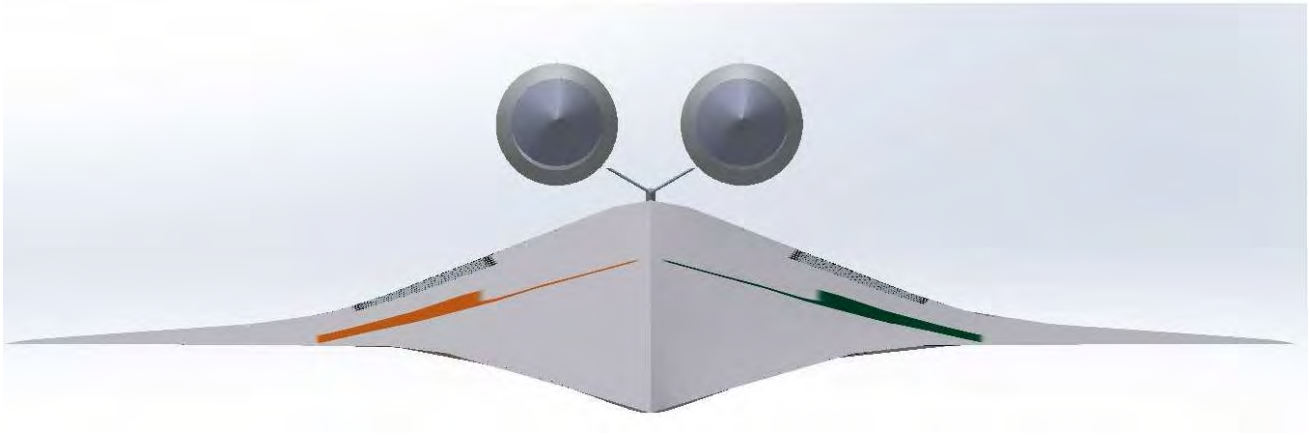

Figure 63: Front view of engines attached to D82S4 in supersonic direction.

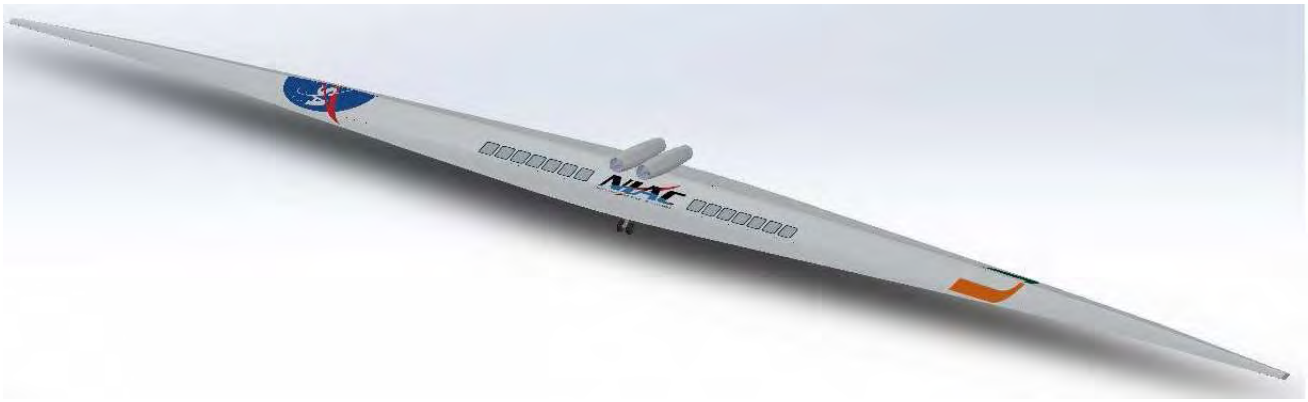

Figure 64: Front view of engines attached to D82S4 in supersonic direction.

7.10 Landing Gear

For landing gear installation, only the small airplane D84TW is considered. The larger airplane such as D82S4 and other designs have even larger room. The landing gear for SBiDir-FW will be a tricycle design. Since takeoff and landing will occur in the subsonic direction, the landing gear will be oriented in the subsonic direction. The tricycle design will consist of one set of nose landing gear with two wheels sharing the same axis and three sets of main landing gear each consisting of two wheels with parallel axis. The nose landing gear and the middle main landing gear is oriented along the mid-plane of the subsonic direction. The two outer main landing gears are located just outside of the passenger area and will be along the same axis as the middle main landing gear. This tricycle design provides a safe design in the event of an uneven landing, which is inherently more likely due to SBiDir's geometry. The extremely long length of SBiDir in the subsonic direction makes landing with all three main landing gears simultaneously difficult. Additionally, small deviation angles from approach can result in disastrous landings as this can cause the wing tips to collide with the ground. Therefore, the two outer main landing gears are located far outward from the center of SBiDir to prevent it from colliding with the ground during gust conditions. This is also necessary due to the need to retract the landing gear. Volume is more readily available to house the landing gear once the passenger cabin ends. The actual placement of the landing gear requires that it folds into place from the rear of the aircraft in order to provide a sufficient stability in landing.

The landing gears are a series of reinforced triangular struts. The volume necessary for the storage of the wheels is located in the central area of SBiDir. Therefore, it is necessary that the wheels be stored in that area, but it is needed further out from this area for a stable landing platform. Therefore, the landing gear is attached to a straight strut reinforced with a second strut to form the triangular structure. This will lock the strut into place during landing and allows for the folding and retraction during flight. This will be accomplished with an actuator within the aircraft. Fig. 65 and 67 show the design of the landing gear.

As can be seen from Fig. 67, the landing gear is just outside of the passenger cabin. For scale, a 5'10" person is inserted in the picture to show the magnitude of the length of SBiDir and the landing gear size. A dimensioned view of the landing gear can be seen in Fig. 67.

The size of the nose and main landing gear wheels were extrapolated using historical data for the aircraft based off the equations given in [3]. Based on the take off weight, the nose landing gear wheels is found to be 0.27-0.3 m in width and 0.75-0.8m in diameter. The main landing gear wheels are found to be 0.3-0.35m in width and 1-1.1m in diameter. However, with new and emerging technologies, it is likely that the size of the landing gear wheels can be decreased but these sizes are sufficient for our needs.

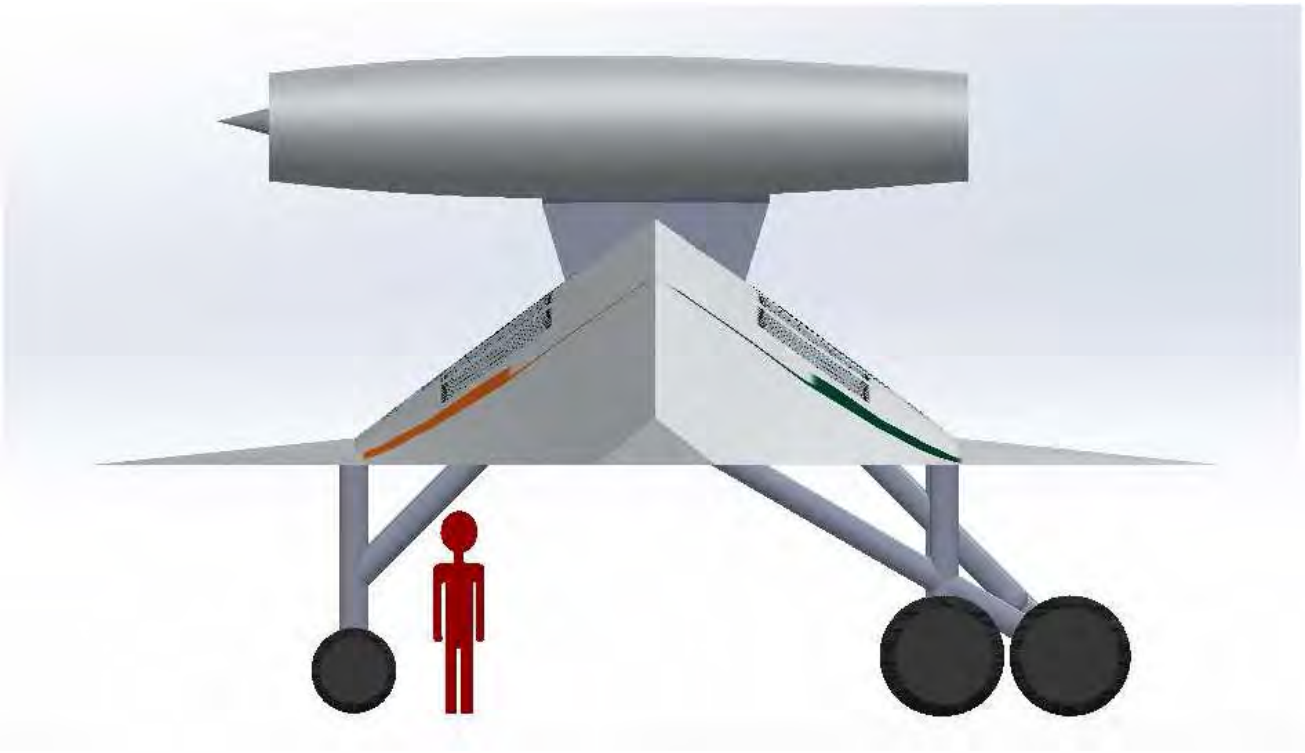

Figure 65: Sideview of D84TW with landing gear compared with an average size person.

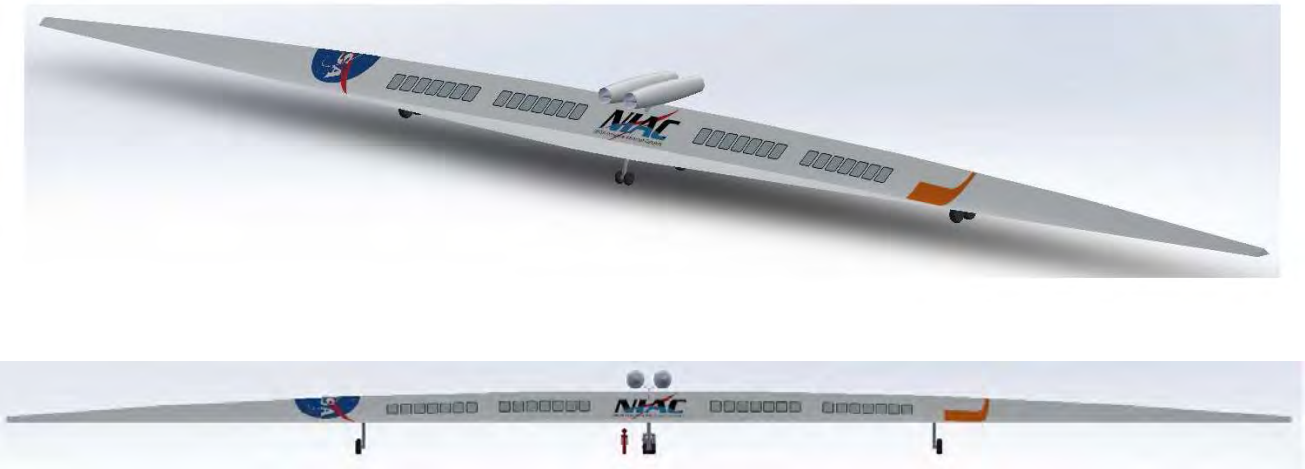

Figure 66: Landing gear on D84TW subsonic direction.

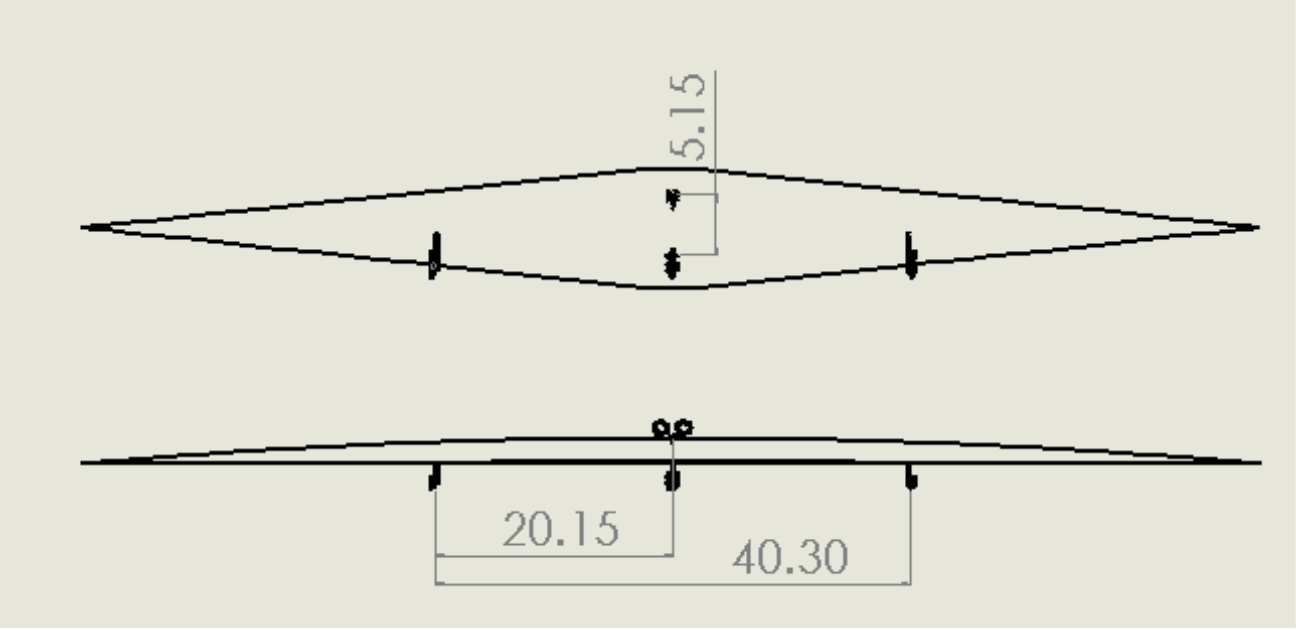

Figure 67: Landing gear dimensions on D84TW subsonic direction (meters).

References

[1] Seebass, R., "Supersonic Aerodynamics: Lift and Drag ." Paper presented at the RTO AVT Course on *Fluid Dynamics Research on Supersonic Aircraft*, RTO EN-4, Rhode-Saint-Gendse, Belgium,, 25-29 May 1998.

[2] Winter, K. G. and Smith, K. G., "Measurements of Skin Friction on a Cambered Delta Wing at Supersonic Speeds." R. & M. No. 3501, AERONAUTICAL RESEARCH COUNC1L, LONDON, HER MAJESTY'S STATIONERY OFFICE, August 1965.

[3] T. C. Corke, *Design of Aircraft*. Prentice Hall, 2003.

[4] Haering, E. A. and Ehernberger, L. J. and Whitmore, S. A. , "Preliminary Airborne Measurements for the SR-71 Sonic Boom Propagation Experiment." NASA TM 104307, Sept. 1995.

[5] Mack, R. J., and Needleman, K.E., "A Methodology for Designing Aircraft to Low Sonic Boom Constraints." NASA TM-4246, February 1991, 1991.

[6] Mack, R. J., and Needleman, K.E., "Aerodynamic Design for Supersonic Speeds." Proceedings of the 1st International Congress in the Aeronautical Sciences (ICAS), Advances in Aeronautical Sciences, Vol 1., Pergamon Press, NY,, 1959.

[7] Hirschberg, M., Hart, D. and Beutner, T., "A Summary Of A Half-Century of Oblique Wing Research." AIAA Paper 2007-150, 2007.

[8] Desktop Aeronautics, Inc., "Oblique Flying Wings: An Introduction and White Paper." http://www.desktopaero.com/obliquewing/library/whitepaper/index.html, 2005.

[9] Campbell, J.P., and Drake, H.M., "Investigation of stability and control characteristics of an airplane model with a skewed wing in the Langley free flight tunnel." NACA TN-1208, May 1947.

[10] Matthews, H. , "Oblique Wing Research Aircraft NASA AD-1." World X-Planes Magazine, No. 2, 2005.

[11] Kroo, I.M., "The Aerodynamic Design of Oblique Wing Aircraft." Proceedings of the AIAA/AHS/ASEE Aircraft Systems Design and Technology Meeting, CP 86-2624, AIAA, Washington D.C., 2005.

[12] Kennelly, R.A., Carmichael, R., Strong, J., and Kroo, I.M., "Transonic Wind Tunnel Test of a 14% Thick Oblique Wing." NASA TM-102230, Aug. 1990.

[13] Kempel, R.W., McNeill, W.E., and Maine, T.A., "Oblique-Wing Research Aircraft Motion Simulation with Decoupling Control Laws." AIAA Paper 88-402, 1988.

[14] R. Jones, " Technical Note - The Flying Wing Supersonic Transport ," *Aeronautical Journal*, vol. 3, March 1991.

[15] R. Seebass, " Sonic-Boom Theory ," *AIAA Journal of Aircraft*, vol. May-June, pp. 177–184, 1969.

[16] A. George and R. Seebass, " Sonic Boom Minimization including Both Front and Rear Shocks ," *AIAA Journal*, vol. 9, 10, pp. 2091–2093, 1971.

[17] R. Seebass and A. George, " Sonic-Boom Minimization ," *Journal of the Royal Aeronautical Society of America*, vol. 51, 2, pp. 686–694, 1972.

[18] Darden, C. M., "Minimization of Sonic-Boom Parameters in Real and Isothermal Atmospheres." NASA TN D-7842, March 1975.

[19] L. B. Jones, " Lower Bounds for Sonic Bangs ," *Journal of the Royal Aeronautical Society*, vol. 65, 606, pp. 433–436, 1961.

[20] Graham, D., "Quiet Supersonic Platform, Shaped Sonic Boom Demonstrator (SSBD) Program." FAA Civil Supersonic Aircraft Workshop, http://www.aee.faa.gov/Noise/aee100_files/SonicWkshp/2-Panel1-Graham-Northrop.pdf, Nov. 2003.

[21] Darden, C. M., "Sonic-Boom Minimization With Nose-Bluntness Relaxation." NASA TP-1348, January 1979.

[22] McLean, F. E., "Some Nonasymptotic Effects on the Sonic Boom of Large Airplanes." NASA TN D-2877, 1965.

[23] Pawlowski, J. W., Graham, D. H., et al., "Origins and Overview of the Shaped Sonic Boom Demonstration Program." AIAA 2005-0005, Jan. 2005.

[24] Howe, D., Simmons, F., and Freund, D., "Development of the Gulfstream Quiet SpikeTM for Sonic Boom Minimization." AIAA Paper 2008-124, 2008, 7-10, Jan. 2008.

[25] NASA, "NASA Research Announcement ROA-2008 Appendix A.4 Supersonics, Amendment 7, 1. Project Overview." 2008.

[26] Welge, H. R. and Nelson, C. and Bonet, J., "Supersonic Vehicle Systems for the 2020 to 2035 Timeframe." AIAA 2010-4930, 28th AIAA Applied Aerodynamics Conference, Chicago, Illinois, 28 June - 1 July 2010.

[27] Magee, T. E. and Shaw, S. G. and Fugal, S. R., "Experimental Validations of a Low-Boom Aircraft Design." AIAA 2013-0646, 51st AIAA Aerospace Sciences Meeting including the New Horizons Forum and Aerospace Exposition, Grapevine, TX, 07-10 Jan. 2013.

[28] Morgenstern, J. M.and Buonanno, M. and Nordstrud, N., "N+2 Low Boom Wind Tunnel Model Design and Validation." AIAA 2012-3217, 30th AIAA Applied Aerodynamics Conference, New Orleans, Louisiana, 25 - 28 June 2012.

[29] A. Jameson, "Optimum Aerodynamic Design Using CFD and Control Theory." AIAA 95-1729-CP, 1995.

[30] A. Jameson, "Aerodynamic Design via Control Theory," *Journal of Scientific Computing*, vol. 3, pp. 233–260, 1988.

[31] Alonso, J. J. and Kroo, I. M. and Jameson, A., "Advanced Algorithms for Design and Optimization of Quiet Supersonic Platforms." AIAA Paper 2002-0144, 2002.

[32] Choi, S. and Alonso, J. J. and Kroo, I. M. and Wintzer, M. , " Multi-Fidelity Design Optimization of Low Boom Supersonic Business Jets." AIAA 2004-4371, Aug. 30-Sept. 1, 2004.

[33] Rallabhandi, S. and Nielsen, E. J. and Diskin, B, "Sonic Boom Mitigation Through Aircraft Design and Adjoint Methodology." AIAA 2012-3220, 30th AIAA Applied Aerodynamics Conference, New Orleans, Louisiana, June 2012.

[34] Zha, G.-C. and Cattafesta, L. and Alvi, F. S. , "Silent and Efficient Supersonic Bi-Directional Flying Wing." Final Report for NASA NIAC Phase I Grant NNX12AR05G8, 9 July, 2013.

[35] Zha, G.-C., " Supersonic Flying Wing with Low Sonic Boom, Low Wave Drag, and High Subsonic Performance (SFW-L^{2}HSP)." Technology Transfer Office UMI-163, University of Miami,FL, Dec. 2008.

[36] Zha, G.-C., " Supersonic Bi-Directional Flying Wing." Provisional patent application No. 61172929, Submitted to USPTO, 27 Apr. 2009.

[37] Zha, G.-C., " Toward Zero Sonic-Boom and High Efficiency Supersonic UAS: A Novel Concept of Supersonic Bi-Directional Flying Wing." US Air Force Academic Outreach UAS Symposium, Grand Forks, ND, Aug. 4-6, 2009.

[38] Z.-J. Hu, M. Zha, G.-C.and Montgomery, T. Roecken, and J. Orosa, "Transonic Compressor Rotor Design Using Non-monotonic Meanline Angle Distribution." ASME Paper GT2007-27994, 2007.

[39] Zha, G.-C., Im, H. and Espinal, D., " Supersonic Bi-Directional Flying Wing, Part I: A novel concept for supersonic flight with high efficiency and low sonic boom ." AIAA Paper 2010-1013, 48th AIAA Aerospace Sciences Meeting, Orlando, FL, Jan. 4-6, 2010.

[40] Berger, C. and Carmona, K. and Im, H.-S. and Espinal, D.and Zha, G.-C., " Supersonic Bi-Directional Flying Wing Configuration with Low Sonic Boom and High Aerodynamic Efficiency." AIAA Paper 2011-3663, 29th AIAA Applied Aerodynamics Conference, Honolulu, Hawaii, 27-30 June 2011.

[41] Shen, Y.-Q. and Zha, G.-C. and Wang, B.-Y., " Improvement of Stability and Accuracy of Implicit WENO Scheme," *AIAA Journal*, vol. 47, No. 2, pp. 331–344, 2009.

[42] Shen, Y.-Q. and Zha, G.-C. , " Improvement of the WENO Scheme Smoothness Estimator," *International Journal for Numerical Methods in Fluids*, vol. DOI:10.1002/fld.2186, 2009.

[43] Shen, Y.-Q. and Zha, G.-C., " A Seventh-Order WENO Scheme and Its Applications." Submitted to SIAM Journal on Scientific Computing, Oct. 2010.

[44] B. Van Leer, "Towards the Ultimate Conservative Difference Scheme, III," *Journal of Computational Physics*, vol. 23, pp. 263–75, 1977.

[45] Y.-Q. Shen and G.-Z. Zha , "Generalized finite compact difference scheme for shock/complex flowfield interaction," *Journal of Computational Physics*, vol. doi:10.1016/j.jcp.2011.01.039, 2011.

[46] Shen, Y.-Q. and Zha, G.-C. and Chen, X.-Y., " High Order Conservative Differencing for Viscous Terms and the Application to Vortex-Induced Vibration Flows," *Journal of Computational Physics*, vol. 228(2), pp. 8283–8300, 2009.

[47] Y.-Q. Shen and G.-C. Zha, "Large Eddy Simulation Using a New Set of Sixth Order Schemes for Compressible Viscous Terms ," *Journal of Computational Physics*, vol. 229, pp. 8296–8312, 2010.

[48] P. Roe, "Approximate Riemann Solvers, Parameter Vectors, and Difference Schemes," *Journal of Computational Physics*, vol. 43, pp. 357–372, 1981.

[49] G.-C. Zha, Y. Shen, and B. Wang, "An improved low diffusion E-CUSP upwind scheme ," *Journal of Computer & Fluids*, vol. 48, pp. 214–220, 2011.

[50] Im, H-S., Chen, X-Y and Zha, G-C., " Detached Eddy Simulation of Rotating Stall Inception for a Full Annulus Transonic Rotor ," *AIAA Journal of Propulsion and Power*, vol. 28, No. 4, pp. 782–798, 2012.

[51] Im, H-S., Chen, X-Y., and Zha, G-C., "Prediction of a Supersonic Wing Flutter Boundary Using a High Fidelity Detached Eddy Simulation." AIAA Paper 2012-0039, 50th AIAA Aerospace Sciences Meeting, Tennessee,TN, submitted to AIAA Journal, 9-12 January 2012.

[52] Wang, B. Y and Zha, G.-C., "Detached-Eddy Simulation of Transonic Limit Cycle Oscillations Using High Order Schemes," *Journal of Computer & Fluids*, vol. 52, pp. 58–68, 2011.

[53] Wang, B. Y and Zha, G.-C., "Detached-Eddy Simulation of a Co-Flow Jet Airfoil at High Angle of Attack," *AIAA Journal of Aircraft*, vol. 48, 5, pp. 1495–1502, 2011.

[54] Im, H. and Zha, G., "Delayed Detached Eddy Simulation of the Aerodynamic Stall Flows Over the NACA0012 Airfoil." AIAA Paper 2011-1297, 49th AIAA Aerospace Sciences Meeting including, Orlando, Florida, 4 - 7 Jan 2011.

[55] Im, H-S. Chen, X.-Y. and Zha, G-C., "Simulation of 3D Multistage Axial Compressor Using a Fully Conservative Sliding Boundary Condition." ASME-IMECE 2011-62049, Proceedings of the ASME 2011 International Mechanical Engineering Congress & Exposition IMECE2011, Denver, Colorado, USA, Nov. 11-17, 2011.

[56] Im, H-S., Chen, X-Y and Zha, G-C., " Detached Eddy Simulation of Transonic Rotor Flutter Using a Fully Coupled Fluid-Structural Interaction ." ASME Paper GT2011-45437, ASME TURBO EXPO 2011, June 6-10, Vancouver, Canada, June 6-10, 2011.

[57] Im, H-S. and Zha, G-C., "Investigation of Co-Flow Jet Airfoil Mixing Mechanism Using Large Eddy Simulation." AIAA Paper 2011-3098, submitted to ASME J. of Fluid Engineering, (41st AIAA Fluid Dynamics Conference and Exhibit, 27-30 June 2011, Honolulu, Hawaii),, 2011.

[58] Wang, B. Y and Zha, G.-C., "High Fidelity Simulation of Nonlinear Fluid-Structural Interaction with Transonic Airfoil Limit Cycle Oscillations," *Journal of Fluids and Structures*, vol. doi:10.1016/j.jfluidstructs.2010.02.003, 2010.

[59] Wang, B.-Y. and Haddoukessouni, B. and Levy, J. and Zha, G.-C., "Numerical Investigations of Injection Slot Size Effect on the Performance of Co-Flow Jet Airfoil ," *AIAA Journal of Aircraft*, vol. 45, pp. 2084–2091, 2008.

[60] X.-Y. Chen, G.-C. Zha, and M.-T. Yang, "Numerical Simulation of 3-D Wing Flutter with Fully Coupled Fluid-Structural Interaction," *Journal of Computers & Fluids*, vol. 36, No. 5, pp. 856–867, 2007.

[61] X.-Y. Chen and G.-C. Zha, "Fully Coupled Fluid-Structural Interactions Using an Efficient High Resolution Upwind Scheme," *Journal of Fluids and Structures*, vol. 20, pp. 1105–1125, 2005.

[62] Z.-J. Hu and G.-C. Zha, "Calculations of 3D Compressible Using an Efficient Low Diffusion Upwind Scheme," *International Journal for Numerical Methods in Fluids*, vol. 47, pp. 253–269, 2004.

[63] Im, H-S. and Zha, G-C., "Effects of Rotor Tip Clearance on Tip Clearance Flow Potentially Leading to NSV in an Axial Compressor." ASME Paper GT2012-68148, IGTI Turbo Expo 2012, Copenhagen, Denmark, June 11-15, 2012.

[64] Im, H-S. and Zha, G-C., "Simulation of Non-synchronous Blade Vibration of an Axial Compressor Using a Fully Coupled Fluid-Structural Interaction." ASME Paper GT2012-68150, IGTI Turbo Expo 2012, Copenhagen, Denmark, June 11-15, 2012.

[65] Chen, X-Y., Im, H-S., and Zha, G-C., "Fully Coupled Fluid-Structural Interaction of a Transonic Rotor at Near-Stall Conditions Using Detached Eddy Simulation." AIAA Paper 2011-0228, 49th AIAA Aerospace Sciences Meeting including the New Horizons Forum and Aerospace Exposition 4 - 7 January 2011, Orlando, Florida, submitted to AIAA Journal, 2011.

[66] B.-Y. Wang and G.-C. Zha, "A General Sub-Domain Boundary Mapping Procedure For Structured Grid CFD Parallel Computation," *AIAA Journal of Aerospace Computing, Information, and Communication*, vol. 5, No.11, pp. 2084–2091, 2008.

[67] Park, M. A., "Low Boom Configuration Analysis with FUN3D Adjoint Simulation Framework." AIAA 2011-3337, 29th AIAA Applied Aerodynamics Conference, Honolulu, Hawaii, June 2011.

[68] Durston, D. A. , " Sonic Boom Extrapolation and Sound Level Prediction." Unpublished Document, NASA Ames Research Center, Sept. 2009.

[69] Casper, J. H. and Cliff, S. E. and Thomas, S. D. and Park, M. A. and McMullen, M.S. and Melton, J. E. and Durston, D. A., " Assessment of Near-Field Sonic Boom Simulation Tools." AIAA Paper 2008-6592, 26th AIAA Applied Aerodynamics Conference, Honolulu, Hawaii, 18-21 Aug. 2008.

[70] Carlson, H. W. and Mack, R.J. and Morris, O. A. , " A Wind Tunnel Investigation of the Effect of Body Shape on Sonic Boom Pressure Distribution." NASA TN-D-3106, Nov. 1965.

[71] Wintzer, M. and Nemec, M. and Aftosmis, M. J., " Adjoint-Based Adaptive Mesh Refinement for Sonic Boom Prediction." AIAA 2008-6593, 26th AIAA Applied Aerodynamics Conference, Honolulu, Hawaii, 18-21 Aug. 2008.